3-31-2016

Flow Boiling Heat Transfer Over Open Microchannels With Tapered Manifold

Ankit Kalani
axk2161@rit.edu

R·I·T

Flow Boiling Heat Transfer Over Open Microchannels With Tapered Manifold

by

Ankit Kalani

A dissertation submitted in partial fulfilment of the requirements for the degree of Doctor of Philosophy in Microsystems Engineering

Microsystems Engineering Program
Kate Gleason College of Engineering

Rochester Institute of Technology
Rochester, New York
31st March 2016

Flow Boiling Heat Transfer Over Open Microchannels With Tapered Manifold

by

Ankit Kalani

Committee Approval:

We, the undersigned committee members, certify that we have advised the candidate on the work described in this dissertation. We further certify that we have reviewed the dissertation manuscript and approve it in partial fulfillment of the requirements of the degree of Doctor of Philosophy in Microsystems Engineering.

Dr. Satish G. Kandlikar — Date
James E. Gleason Professor, Mechanical Engineering (Advisor)

Dr. Robert Stevens — Date
Associate Professor, Mechanical Engineering

Dr. Steven Day — Date
Department Head, Biomedical Engineering

Dr. Jiandi Wan — Date
Associate Professor, Microsystems Engineering

Certified By:

Dr. Bruce Smith — Date
Director of Microsystems Engineering

Dr. Harvey J. Palmer — Date
Dean, Kate Gleason College of Engineering

Abstract

Kate Gleason College of Engineering
Rochester Institute of Technology

Degree: Doctor of Philosophy
Program: Microsystems Engineering
Author: Ankit Kalani
Advisor: Satish G. Kandlikar

Dissertation Title: Flow Boiling Heat Transfer Over Open Microchannels With Tapered Manifold

Boiling can provide several orders of magnitude higher performance than a traditional air cooled system in electronics cooling application. It can dissipate large quantities of heat while maintaining a low surface temperature to fluid difference. Flow boiling with microchannels has shown a great potential with its high surface area to volume ratio and latent heat removal. However, flow instabilities and early critical heat flux (CHF) have prevented its successful implementation. A novel flow boiling design based on a mechanistic approach is taken to overcome the above mentioned disadvantages while presenting a very low pressure drop. The design uses open microchannels with tapered manifold (OMM) to provide stable and efficient operation.

The tapered manifold above the microchannels provides an increasing cross-sectional area in the flow direction. The extra flow cross-sectional area allows bubbles to emerge from the microchannels and expand in the manifold along the flow direction. Using a 6% taper and a moderately high inlet liquid flow Reynolds number of 1095, a CHF of 1.07 kW/cm^2 with a heat transfer coefficient of 295 $kW/m^{2\circ}C$ and a pressure drop of 30 kPa was recorded. Baseline test with uniform manifold were conducted and compared with tapered geometry. The experimental data was substantiated with pressure drop modeling for the new geometry. High speed visualization was also conducted to understand the underlying mechanism in the tapered configuration.

Acknowledgement

There are many people that have contributed to my successful completion of my degree. I want to recognize a few of them here. Dr. Kandlikar, you have given me this wonderful opportunity and I am so deeply grateful that you took a chance on me. Mere words cannot express my awe of you, thank you so much for always supporting me.

Mom, Dad and Didi, all of this would not be possible or worth anything without your support. You have given me so much encouragement, strength and belief throughout this journey. I cannot imagine the sacrifices that you all have had to make for me to reach here, I hope this achievement in some small way brings you satisfaction. We did it!

My lab members past and present, thank you for being patient with me and always supporting me. Bob, Andrew and Alyssa thank you for your tremendous support in the fabrication of the test setup. Pruthvik, Arvind and Isaac for being wonderful lab mates and sounding board. I have been fortunate to be involved with three amazing volunteer organizations, Recover Rochester, Flower City Pickers and Habitat for Humanity. Thank you so much for allowing me to be a part and serve the Rochester community. In their own way, they all have had a profound impact on my life and through them I have met some incredible individuals.

Thank you to my committee members, the fantastic ME department staff and Mircrosystems department for providing support during my studies. This work was supported by the National Science Foundation under Award No. CBET-1236062

Lastly, I would like to thank God, I am privileged and blessed to have such wonderful people in my life. It is all your will.

Dedication

To Mom, Dad and Sister

Thank you for dreaming

Table of Contents

List of Figures

List of Tables

Nomenclature

Term	Description	Units/Value
A	Projected area	m^2
A_c	Cross-sectional area	m^2
A_{ca}	Channel area	m^2
A_p	Total plenum cross-sectional area	m^2
Bo	Boiling number	-
CHF	Critical heat flux	W/cm^2
Co	Convection number	-
C_p	Specific heat	kJ/kgK
D	Diameter	m
dA/dz	Change of c/s area w.r.t channel length	-
DAQ	Data acquisition system	-
D_h	Hydraulic diameter	μm
dp/dz	Pressure drop	kPa
dT/dx	Temperature gradient	°C/mm
dx	Distance between two thermocouples	mm
dx/dz	Change of quality w.r.t channel length	-
f	Fanning frictional factor	-
f_{app}	Apparent fanning frictional factor	-

Term	Description	Units/Value
F_{Fl}	Fluid-surface dependent parameter	-
f_{TP}	Tow-phase frictional factor	-
G	Mass flux	kg/m^2s
h, HTC	Heat transfer coefficient	$W/m^2°C$
h_{fg}	Latent heat of vaporization	kJ/kg
h_{Lo}	Heat transfer coefficient – single phase	$W/m^2°C$
$h_{TP, CBD}$	Heat transfer coefficient – Convection boiling dominant	$W/m^2°C$
$h_{TP, NBD}$	Heat transfer coefficient – Nucleate boiling dominant	$W/m^2°C$
k_L	Liquid thermal conductivity	W/m-°C
k_{Cu}	Thermal conductivity of copper	W/m-°C
K_{ent}	Entrance loss	-
K_{exit}	Exit loss	-
L	Total channel length	10 mm
L_{sp}	Single phase length	m
L_{tp}	Two-phase length	m
$\dot{m}$	Mass flow rate	kg/s
Nu_{LO}	Nusselt number – liquid only	-
OMM	Open Microchannel with Manifold	-
P_{in}	Inlet pressure	kPa

Term	Description	Units/Value
P_{out}	Outlet pressure	kPa
P_w	Wetted perimeter	m
Q	Total heat transferred	W
q”	Heat flux	W/cm^2
Re	Reynolds number	-
Re_{LO}	Reynolds number – Liquid only	-
S	Manifold height	mm
T_1	Top thermocouple	°C
T_2	Middle thermocouple	°C
T_3	Lowest thermocouple	°C
T_s	Surface temperature	°C
u_m	Average velocity	m/s
U_p	Uncertainty in the parameter *p*	-
v_f	Specific volume of liquid	m^3/kg
v_g	Specific volume of gas	m^3/kg
W	Channel width	m
x	Exit vapor quality	0-1
x_1	Distance between top thermocouple and heater surface	mm
α_c	Channel aspect ratio	-

Term	Description	Units/Value
ΔP	Pressure drop	kPa
ΔT	Temperature difference	°C
Po	Poiseuille number	-
ΔT_{sat}	Wall superheat	°C
$\Delta T_{sub,\ ONB}$	Degree of subcooling at the onset of nucleate boiling	°C
ρ	Density	kg/m^3
ρ_L	Liquid density	kg/m^3
ρ_v	Vapor density	kg/m^3
$\dot{V}$	Volumetric flow rate	m^3/s (mL/min)
μ_l	Liquid viscosity	Pa-s
μ_v	Vapor viscosity	Pa-s

Chapter 1: Introduction and Background

1.1 Motivation

The general trend in electronic devices has been a move toward reduced product size while simultaneously providing greater processing speed, both of which have contributed to dramatic increases in device power consumption. Heat is an unavoidable byproduct of operating electronics, but if not managed properly, system performance and reliability will be adversely affected. Therefore, proper thermal management is essential to prolong the life and reliability of such devices. To illustrate the increasing demand for solutions to this problem, the BCC Research group [1] has estimated that the global market for thermal management in various industries including electronics, medical, aerospace and defense will grow from $10.1 billion in 2013 to $14.7 billion by 2019.

The projected growth of the thermal management systems market is largely a result of several challenges to electronic device cooling which have not yet been surmounted. These include:

1. Product miniaturization and reduced form factor
2. Reduction in product cost
3. Reliability and performance constraints
4. Incorporating new advancements in technology and materials
5. Harsh environmental conditions

Conventional cooling techniques (which includes cooling fans, heat sinks and heat pipes among other techniques) have been unable to overcome the aforementioned challenges, especially at heat fluxes approaching 1000 W/cm^2 [2]. This only serves to intensify the necessity of advanced cooling techniques in order to satisfy current and future

needs. A brief summary of various thermal management methods related to cooling of high heat flux electronic devices is presented below.

1.1.1 Single-phase flow

For decades, air has been the preferred fluid for cooling electronics on account of its availability, low cost (cooling fans), ease of mass production and high reliability for a wide range of applications. Despite its long history of use however, air cooling has proved itself to be unable of coping with newer, increased chip power densities. As such, liquid cooling systems are beginning to rise in popularity. In general, cooling liquids have significantly superior thermal properties compared to air and are expected to meet the thermal management demands of most high heat flux systems. For example, the use of cold plates—a method involving indirect liquid cooling—is already widely used in industry, and comprehensive research is being conducted to improve cold plate thermal performance [3,4]. Direct single-phase liquid cooling has been demonstrated to provide excellent cooling performance in recent years. The fluid medium has to be nontoxic, stable, nonflammable and of high dielectric strength.

Passive enhancements have shown improved heat dissipation rates in comparison to their plain surface counterparts. Microchannels, in particular, have demonstrated superior capabilities for high heat flux dissipation. The pioneering work of Tuckerman and Pease [5] has shown potential for electronics cooling with microchannels, although high pressure drops have been a limitation. Colgan et al. [6] developed a single-phase liquid microchannel cooler with offset strip fins capable of dissipating power densities greater than 300 W/cm^2. The disadvantages of the pumped single phase cooling are discussed below:

- Surface temperature: The surface temperature increases along the stream-wise direction due to heat dissipation. This causes uneven cooling along the length of the chip, which corresponds to increased surface temperature towards the downstream section.
- Bulk liquid temperature: Increases in bulk liquid temperature requires increase in flow rates in order to maintain uniform temperatures for both the bulk liquid as well as the surface. This necessitates a higher pumping power in addition to an increased coolant inventory size.
- Pressure drop: Higher flow rates correlate to increase in pressure drop. In order to account for this greater pressure drop within the system, a higher capacity pump must be selected, which contributes to increased cost and energy consumption. Moreover, higher pressure drops along the fluid flow length can cause unwanted fluid property and saturation temperature variation, leading in turn to unstable flow.

The above-mentioned disadvantages can be addressed by using two-phase pumped liquid systems.

1.1.2 Two-phase flow

Phase change or two-phase (liquid-vapor) flow can provide greater cooling than single-phase due to the significantly higher latent heat compared to sensible heat removal capabilities. The latent heat provides 2–3 orders of magnitude higher heat dissipation. Similar to direct immersion cooling, the fluid selected has to have sound electrical and thermal properties. Boiling is an important mode of heat transfer in a broad range of applications, such as power generation, petrochemical processing, pharmaceuticals and high heat flux removal systems. Boiling can be classified into pool and flow boiling.

Pool boiling

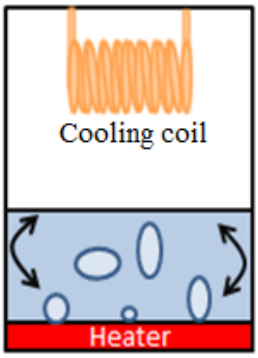

Figure 1: Schematic of a pool boiling system

Pool boiling can be defined as the boiling of stagnant fluid over a heated surface, as seen in Fig. 1. It can dissipate large amounts of heat due to the latent heat effects while maintaining a relatively low surface temperature difference compared to single phase flow. Unlike pumped single-phase flow, pool boiling is completely passive in that it does not require any moving parts for heat dissipation (such as pumps). Rather, the fluid motion is maintained by the expansion and departure of bubbles from the heated surface.

Flow boiling

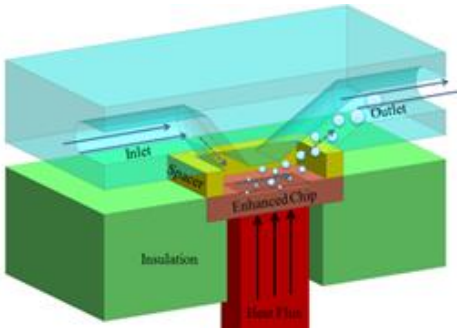

Figure 2: Schematic of a flow boiling system

Flow boiling is another technique widely studied by researchers as a means to exploit the large latent heat required for the phase change from liquid to vapor. It can be defined as boiling of a flowing fluid over a heated surface. The fluid flow can be achieved through natural convection (thermosyphon) or forced by an external pump. The advantages of flow boiling include high heat transfer performance, a uniform temperature environment, low coolant inventory and an only small increase in surface temperature (as compared to single phase).

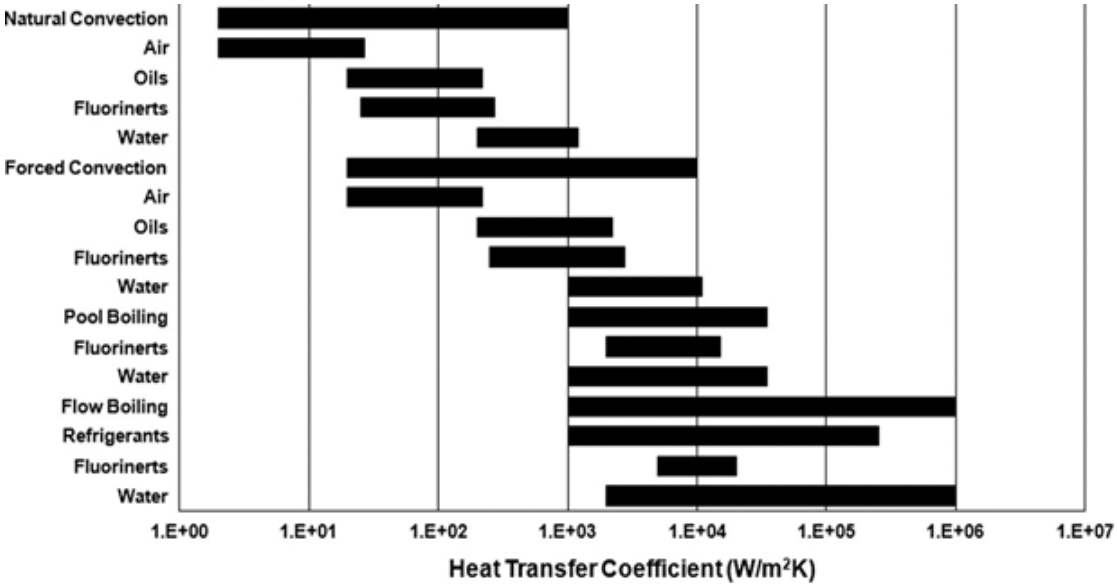

Figure 3: Heat transfer coefficient values of various cooling techniques with different fluid media [7]

Figure 3 summarizes the thermal performance of various cooling methods [7]. The above figure shows that two-phase techniques (pool and flow boiling) show greater thermal performance than natural and forced air convection. Flow boiling, in particular, shows the highest performance with water among all of the methods. Water is chosen as the fluid

medium due to its well-established properties, widespread availability, non-toxic nature and high thermal properties. Proper precautions must be taken so as to avoid contact with the electrical circuit.

1.2 Research Background

1.2.1 Surface enhancement techniques for two-phase cooling

Boiling occurs at a solid-liquid interface. Due to this, various surface enhancement techniques have been used by researchers in the past three decades to obtain improved heat transfer performance. These enhancements not only increase the overall surface area but also affect the underlying mechanism, which in turn provide higher heat transfer capabilities. Some of the most commonly used enhancements are listed below:

i. Microchannel – Parallel channels [8], fins [9], circular pin-fin [10], hybrid combination of channels with pin structure [11] etc.

ii. Microporous – Mesh structure [12], screen laminate [13] and other porous structure obtained through techniques like sintering [14] and electrodeposition.

iii. Nanostructure – Nanowires (NW) [15], carbon nanotubes (CNT) [16], superhydrophobic and superhydrophilic surfaces [17], and MEMS technique used to create reentrant cavities and channels.

For the current work, microchannels are selected as the enhanced surface. Microchannels were chosen due to the following advantages; high surface area to volume ratio, compact, easy to machine and simple in construction. They have been widely used in industry for cooling of electronics, lasers, avionics, and hybrid vehicle power electronics and, more recently, heat exchangers for high-Mach turbine engines and hydrogen fuel cell systems [18]. The channel classification for microchannels [19] is between 200 μm > D_h > 10 μm, where D_h is the smallest channel hydraulic diameter. Microchannels usually

comprise of numerous parallel channels with a cover plate on the top surface, while open microchannels do not have the cover plate. Microchannels can be of a nonrectangular cross-section such as triangular, trapezoidal and diamond–shaped. In the current work, microchannels are considered to be a rectangular cross-section unless specified otherwise. Microchannels can be made using various techniques which include CNC machining, micro-sawing, etching through MEMS and laser micro-machining. A CNC machine was used to obtain the microchannel surface with required geometrical parameters for this work.

1.2.2 Boiling curve

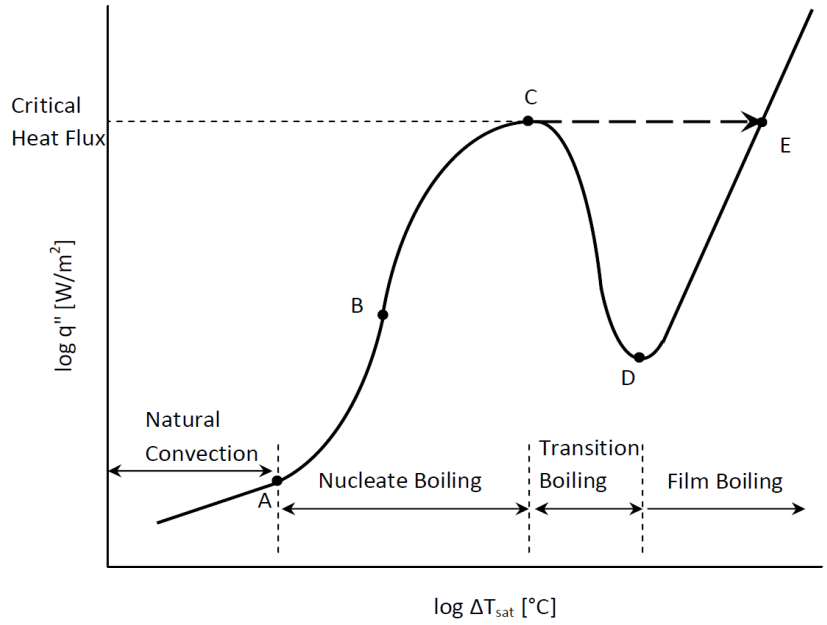

Figure 4: Boiling curve [20]

The boiling curve is represented with heat flux at the y-axis and wall superheat at the x-axis as seen in Fig. 4. Heat flux is the rate of heat transfer per unit area; generally the projected area of the heat transfer surface is used for the calculations, while wall superheat is the temperature difference between the surface temperature and the saturation

temperature of the liquid used. The plot shows various mechanisms involved in pool boiling. Nukiyama [21] was the first to identify these regimes in pool boiling and since then these regions have been used to characterize pool boiling performance.

Critical Heat Flux (CHF) or burnout refers to the upper limit of nucleate boiling. Further increase of heat flux beyond the CHF can cause dramatic increase in surface temperature, which can result in severe damage or meltdown of the surface. During CHF, the rate of bubble nucleation exceeds the rate of bubble detachment from the surface. Bubbles merge to form a continuous vapor blanket over the heater surface thus preventing liquid contact with the surface. The reduction in heat flow from the surface and increase in surface temperature causes reduction in the heat transfer coefficient. The heat transfer coefficient is the measure of efficiency of boiling heat transfer and can be defined as the ratio of heat flux to wall superheat ($q''/\Delta T_{sat}$). In the current work the focus is on flow boiling, hence the above regimes are not discussed in detail, however excellent discussion for the pool boiling curve is available in various heat transfer textbooks [22,23].

For flow boiling, different flow regimes are used to understand the underlying mechanism (discussed in the next section), yet the pool boiling curve is discussed as the same axes are used to characterize the flow boiling performance.

1.2.3 Flow pattern

Flow patterns are used to identify different regimes present in a flow boiling system. They can also be used for characterizing the flow boiling performance. Depending on the adiabatic or diabatic nature and orientation (vertical or horizontal) of the system, varying flow patterns can be obtained. Flow regimes also depend on heat flux, flow rate, geometry

and pressure in the system. Excellent reviews on flow pattern covering various parameters are available in literature. In the current study, diabatic and horizontal orientation are further investigated.

Identifying flow pattern and studying individual flow regime can help in gaining insight into the underlying bubble growth and departure cycle, which in turn assists in understanding heat transfer mechanism. Furthermore, flow pattern identification can assist in the theoretical modeling of a pressure drop or heat transfer model.

An example of various flow regimes observed in flow boiling with microchannels [24] for 400 μm × 400 μm channels as seen in Fig. 5, is discussed below.

1. Bubbly Flow – Isolated bubbles that are smaller than the cross-section of the microchannel appear and flow in the direction of the fluid. The shape and size of these may vary depending on the flow rate and heat flux.
2. Slug Flow – An increase in heat flux causes the bubble to become larger and occupy the entire channel. Small bubbles can be seen in between the elongated bubbles.
3. Churn Flow – It is characterized by rapidly nucleating bubbles and chunks of vapor flowing downstream.
4. Wispy-Annular Flow – The vapor core separates from the wall and a thick unstable liquid film occupies the channel wall.
5. Annular Flow – Further increase in heat flux causes a decrease in the thickness of the liquid film at the channel wall. The interface between liquid and vapor can become wavy.

6. Inverted Annular Flow/CHF – At the highest heat flux, a thick vapor blanket forms at the walls and cuts access of the flowing liquid to the wall. This regime is to be avoided since it is accompanied by a sudden increase in wall temperature and significant decrease in the heat transfer capability.

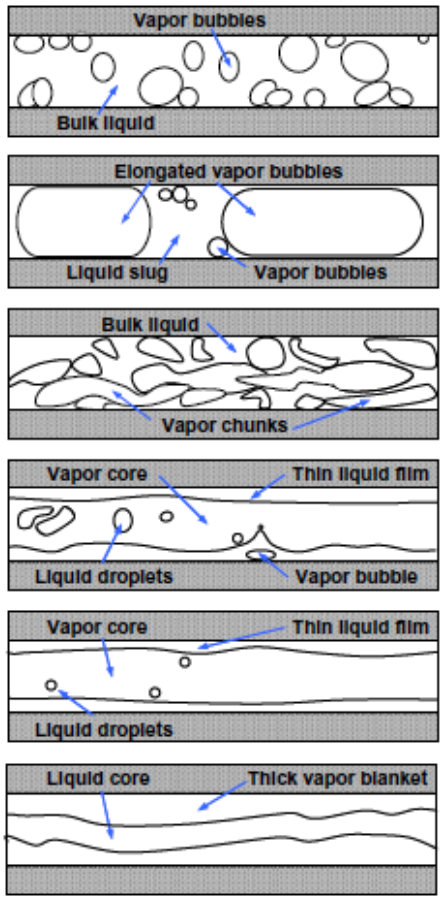

Figure 5: Schematic of a flow boiling regimes in microchannels [24]

The above mentioned regimes may vary depending on the dimension of the channel, flow rate and heat flux. Flow regime maps are also widely used in literature to identify various flow patterns. Taitel and Dukler [25] mapped the flow regime into four patterns (Stratified, Intermittent, Bubble and Annular) with superficial gas and superficial liquid

coordinates. This mapping methodology is one of the popular techniques seen in literature. However, this methodology was obtained for an adiabatic system, avoiding the thermal interactions present in the diabatic conditions. Flow regime maps defined by the flow rate and heat flux have been used for boiling condition.

1.2.4 Flow instability

Flow instabilities have been widely established as one of the main disadvantages of the flow boiling process. They can severely affect the thermal performance of the flow boiling system and significantly hinder the practical realization of flow boiling. The below discussion focuses on the most commonly observed instabilities in literature [26].

Rapid bubble growth

Explosive or rapid growth of a nucleating bubble in microchannels is seen as one of the key flow instabilities. The bubble grows in both upstream and downstream directions causing flow reversal. In some cases, the bubble growing upstream enters into the inlet header, causing severe pressure and temperature fluctuations and preventing the flow of the incoming liquid into the channels. This behavior can be explained by two interrelated mechanism, bubble nucleation and pressure waves during bubble growth [26]. A detailed review of the nucleation characteristics during flow boiling has been provided by Kandlikar [27]. Hsu's model [28] provides the condition required to predict a bubble to grow in a surface cavity. The bubble growth rate after nucleation depends on local liquid conditions and wall superheat surrounding the bubble. The local liquid subcooling ($\Delta T_{Sub,ONB}$) can be obtained through the following equation:

$$\Delta T_{Sub,ONB} = \frac{q''}{h} - \Delta T_{sat,ONB} \quad (1)$$

where ΔT_{sat} is the wall superheat, q" is the heat flux and h is the heat transfer coefficient. For the high heat transfer coefficient as seen in microchannels [29], from the above equation a low subcooling is obtained. In certain cases, the subcooling could be negative (superheated liquid). Hence when the bubble nucleates from the cavity overcoming the surface tension forces, the bubble experiences superheated liquid environment. This causes explosive bubble growth as seen by various researchers [30,31].

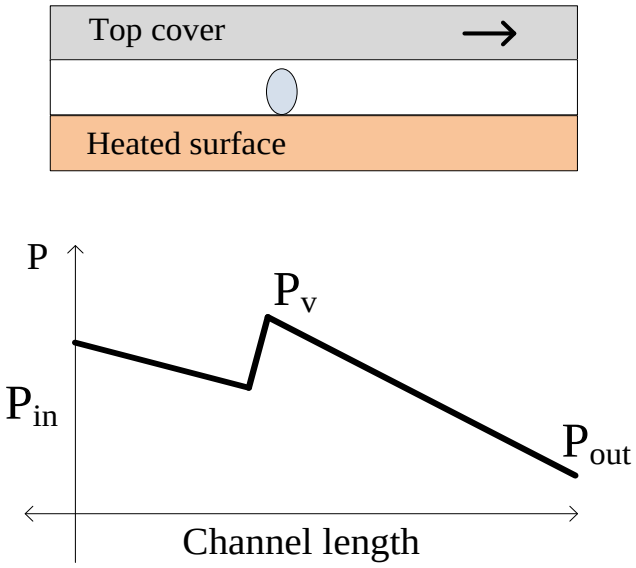

Figure 6: Schematic representation of pressure variation due to bubble nucleation.

Bubble nucleation causes a local pressure increment in the flow system as seen from Fig. 6. The max pressure that can be obtained by the bubble (P_v) depends on the saturation pressure which corresponds to the wall temperature at the nucleation site. Depending on the local condition near nucleation, the bubble could overcome the inertia of the incoming

liquid flow and cause a flow reversal. This flow reversal causes temperature and pressure drop oscillations which have also been observed by various researchers in literature [32,33].

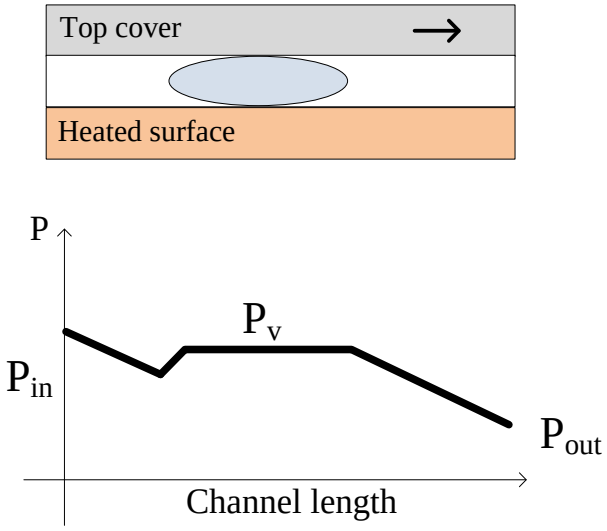

Figure 7: Schematic representation of pressure variation due to bubble nucleation

Figure 7 shows the pressure variation along the length of the channel for an expanding bubble. As the bubble expands, the pressure inside the bubble decreases and enters a relaxation period. The pressure value eventually drops below the inlet pressure, therein reversing the bubble's upward movement and forcing it to flow in the direction of the fluid flow (downstream).

Upstream compressible volume instability

Presence of compressible volume in the upstream leads to oscillating flow and eventually CHF [34]. The compressible volume is due to the presence of non-condensable gases in the fluid. These gases are often trapped in piping paths or occur from a flexible

hose, entrained bubble or a large volume of liquid in a flexible container. If sufficient non-condensable gases are present in the liquid volume upstream of the channel, changes in inlet pressure will compress the gas and affect the supply of liquid to the channels. This will in turn modify channel inlet conditions [26]. Further combining with rapid bubble growth instability, they can lead to long period of pressure and temperature oscillations. Degassing the liquid medium and providing a leak proof system can assist in overcoming this instability.

Critical heat flux condition

The CHF condition marks the transition of a flow boiling system from an efficient heat transfer mode to an ineffective one. It is the upper limit of the nucleate boiling regime. During CHF, the heated channel wall is covered by a vapor blanket and the flowing fluid is not in contact with the surface. Since liquids have superior thermal properties compared to vapor, there is a sharp rise in surface temperature and a reduction in the heat transfer coefficient. In general, when a heated surface is devoid of liquid supply and is blanketed by vapor, the CHF condition is said to be reached and causes dramatic reduction in the heat transfer coefficient. The CHF conditions depend on the following parameters: mass flux, channel length, channel diameter (or hydraulic diameter), system pressure, type of fluid and inlet subcooling. CHF can lead to system meltdown due to the high temperatures. Therefore, a great interest is present in the prediction of CHF and obtaining a corresponding correlation.

1.3 Structure of Dissertation

The dissertation is structured as follows:

Chapter 1: Introduction and Background - provides an introduction to thermal management, various cooling techniques, microchannels and relevant flow boiling theory.

Chapter 2: Literature Review - focuses on the work done by various authors in flow boiling. It provides details on the different techniques used to enhance flow boiling in microchannels. Summary of the literature is provided at the end, followed by the research objective for the current work.

Chapter 3: Experimental Setup – The new geometry is introduced and the details of the fabricated test loop are discussed. Furthermore, details of the test section in terms of materials, sensors and data analysis is presented. Uncertainty analysis is also explained.

Chapter 4: Experimental Results with Uniform and Tapered Manifold – This chapter discusses the heat transfer and pressure drop performance of the new geometry. High speed visualization, flow patterns and flow pattern maps are also discussed. Underlying mechanism for high heat transfer with OMM geometry is explained.

Chapter 5: Flow Visualization – High speed visualization, flow patterns and flow pattern maps are also discussed. Underlying mechanism for high heat transfer with OMM geometry is explained.

Chapter 6: Pressure Drop Modeling – Homogeneous flow model is used for pressure drop prediction and compared with experimental data. Effect of taper and individual pressure drop components are evaluated.

Chapter 7: CHF and Heat Transfer Modeling – Presents CHF results for six flow rates. Discussion on the extension of CHF due to high flow rate. Heat transfer coefficient correlation from literature is also compared with experimental data.

Chapter 8: Key Contributions and Future Recommendations – Presents some of the key takeways from this study and suggestions for future work

Chapters 9 and 10: References and Appendix respectively

Chapter 2: Literature Review

2.1 Previous Work

Microchannel two-phase cooling is accomplished with the help of a heat sink that consists of a high conductivity material containing parallel, small diameter channels. The simplicity and ease of fabrication of the design are the key reasons behind its unprecedented popularity in the industry. Most microchannel geometries of interest possess diameters in the range of 0.1–0.6 mm. These microchannel devices are therefore very compact and lightweight, and provide high heat transfer coefficients by capitalizing upon the coolant's latent heat content rather than the sensible heat alone (seen in single phase liquid cooling). This greatly reduces the flow rate required to dissipate the same amount of heat compared to single-phase cooling, which also helps reduce coolant inventory for the entire cooling system. Flow boiling with microchannels also provides better temperature uniformity by maintaining surface temperatures close to the coolant's saturation temperature. However, two-phase microchannel cooling is not without shortcomings, and their implementation is hindered by the relatively limited understanding of two-phase flow in microchannels.

The literature review section focuses on the flow boiling studies conducted using microchannels as their heated surface and water (primarily) as the fluid medium. A number of issues, such as flow instabilities [26], early CHF [33] and low heat transfer coefficient [35] have prevented it from reaching its full potential. This section focuses on the above mentioned issues and the various techniques used by researchers to overcome them. Results are presented in the form of heat flux, mass flux, pressure drop and wall superheat values.

Previous work based on pressure drop models, high speed visualization and critical heat flux are discussed in later sections with the experimental results.

Flow instability has been widely recognized as one of the major disadvantages in the flow boiling system. The instability arises through rapid expansion of the growing bubble in the channel. Unlike in a pool boiling system where a bubble can nucleate, grow and depart, the growth of a bubble in a flow system is hindered by the channel. Once the bubble grows to the size of the hydraulic diameter of the channel, it expands in both the upstream and downstream direction as seen in Fig. 8 [36].

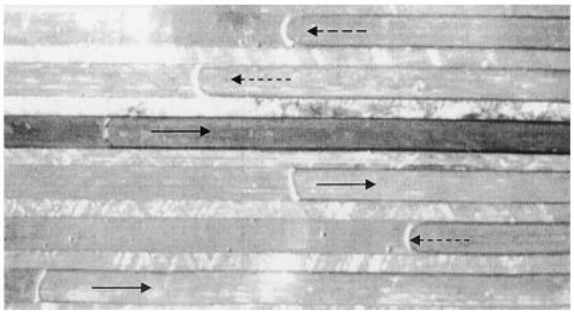

Figure 8: Flow reversal in parallel microchannel [36]

This causes flow reversals, increase in pressure drop due to increased fluctuations and in some cases, introduction of vapor in the inlet manifold region. Due to this backflow, the channels are no longer in contact with the incoming liquid, which in turn can lead to rise in surface temperature and in some cases early critical heat flux. The added increase in pressure causes increase in pumping power, which in turn leads to more consumption of energy. A large pressure drop will cause variation in saturation temperature and fluid properties across the channels. Instabilities are generally classified through flow visualization and pressure and temperature fluctuations.

Early studies from Steinke and Kandlikar [33] using 214 μm wide, 200 μm deep and 57.15 mm long microchannels showed low CHF and HTC values for flow boiling with microchannels. The authors observed high HTC at low exit qualities and the HTC reduced dramatically from 110 kW/m^2°C to about 45 kW/m^2°C at x =0.4.

Inlet restrictors or throttling flow (using a throttle valve) are the most commonly used techniques to overcome flow instability. Qu and Mudawar [37] found two types of dynamic instabilities, Ledinegg and parallel channel instability (Fig. 9), in their work. Large fluctuations of pressure and temperature were observed for the pressure drop oscillation instability (Fig.9a). In some cases, the float of the rotameter also fluctuated, showing the inability of the pump to deliver constant flow rate due to this instability. At higher heat fluxes, due to the large oscillation, the vapor entered the inlet plenum area causing early CHF to occur. The authors used a throttling mechanism at the inlet to suppress the large oscillations. Reduction in pressure and temperature oscillations were observed due to throttling of the inlet control valve. A mild oscillation was still encountered (Fig. 9b); this random fluctuation was termed as the parallel channel instability. The parallel channel instability was due to the density wave oscillation and the feedback effect between the channels. The authors used a microchannel heat sink containing 21 parallel microchannels, 231 μm × 713 μm, and obtained a maximum heat flux of 130 W/cm^2.

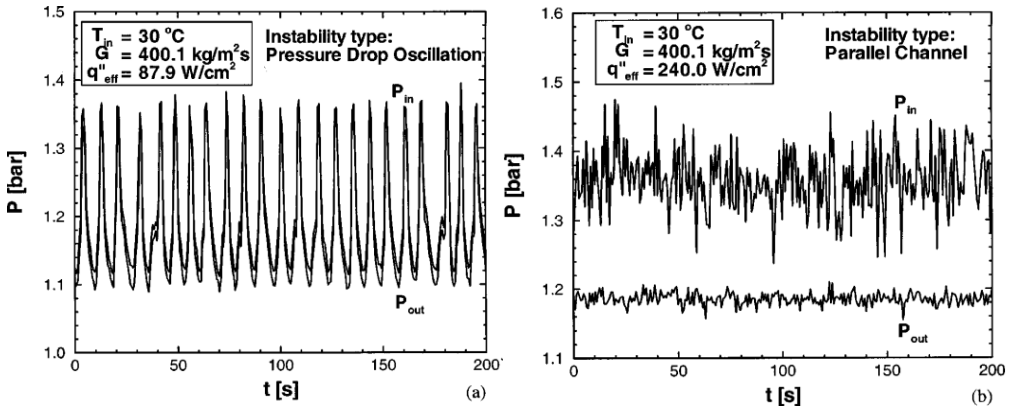

(a) (b)

Figure 9: Temporal records of the two instabilities (a) Pressure drop oscillation (b) Parallel channel instability [37]

Liu and Garimella [38] experimentally investigated flow boiling in microchannels with inlet water temperatures of 79.7 °C to 95.4 °C with the outlet at atmospheric pressure, and mass fluxes of 221-1283 kg/m^{2}s. They obtained a maximum CHF of 129 W/cm^2 with a maximum HTC of 30,000 W/m^2°C and a maximum exit quality of 0.2. They also obtained low pressure in their study, primarily due to the large channel dimension used in their experiments.

The presence of large vapor in the microchannel cross-sectional area reduces the liquid film thickness near the heated channel walls and leads to eventual dryout. Removing vapor from the channel as it is formed keeps the channels filled with liquid, thereby extending the CHF. With nucleation sites activated and the right conditions provided by the liquid flow in the channel, the HTC is also enhanced. Using this principle, Kandlikar et al. [39] used artificial nucleation sites and pressure drop elements (inlet restrictors) in their flow stabilization study. The artificial nucleation sites were introduced to promote early nucleation in the microchannel. They obtained extremely low pressure fluctuations (0.3

kPa) and stable flow with the combination of the above two techniques. However, the study was conducted only at low heat fluxes (max q" = 298 kW/m^2).

Wang et al. [40] used different configurations of inlet/outlet restrictors with trapezoidal shaped microchannels for their instability study. Figure 10 shows one of the configurations used in their study. The authors also pointed out the configuration between the inlet and outlet regions with the microchannels played an important role in affecting the boiling instability. They recommended a configuration which has only inlet restrictors and no outlet restrictors.

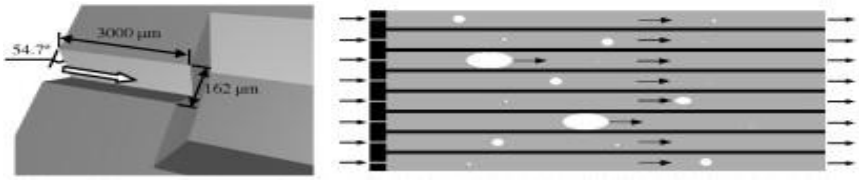

Figure 10: Configuration with inlet restrictors and no outlet restrictors [28]

Kuo and Peles [41] used reentrant cavities in microchannels to enhance heat transfer performance. The overall dimension of the geometry was 1.8 mm × 10 mm, while the microchannels were 200 μm wide, with 200 μm fin width and 253 μm deep. Five microchannels were placed on a silicon substrate. The reentrant cavity size was selected which conformed to the active nucleation cavity range as given by Hsu's model [28]. A maximum critical heat flux (CHF) of ~200 W/cm^2 at a mass flux of 520 kg/m^{2}s using microchannels was achieved with reentrant cavities. Kosar et al. [42] used a similar test setup with the addition of inlet restrictors to obtain a CHF of 614 W/cm^2 at a mass flux of 389 kg/m^{2}s. The wall superheat was as high as 80 °C with a heat transfer coefficient of

around ~75 kW/m^2°C. The overall pressure drop in the system varied from 50 – 200 kPa. The high wall superheats obtained in this work may not be suitable in an electronics cooling application.

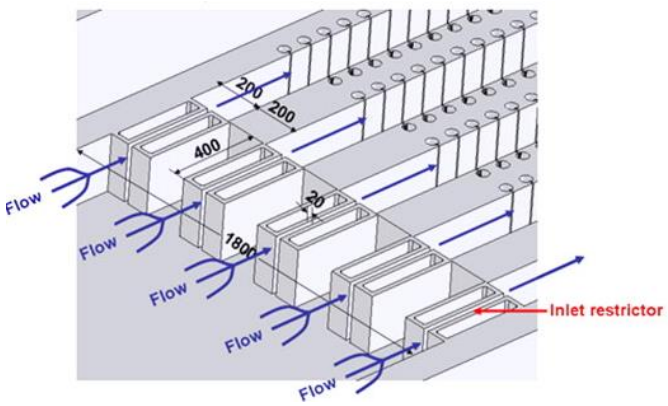

Figure 11: Schematic of a microchannel geometry with reentrant cavities and inlet restrictors [41]

Zhang et al. [43] extensively studied the Ledinegg instability in microchannels. They concluded that the presence of inlet restrictors, increase in the system pressure and the channel diameter, and reduction in the number of channels and the channel length lead to a more stable flow in the microchannels. Inlet restrictors have been used by various investigators in stabilizing the fluid flow. Although efficient, they introduce a significant pressure drop in the flow system. This would lead to an increase in the pumping power requirement for the cooling system.

Fins in microchannels have been used to provide a greater heat transfer surface area while enhancing boiling performance through additional nucleation sites. However, they offer a larger flow resistance which in turn, increases the pressure drop in the system. They have been successfully used in compact heat exchanger passages. Krishnamurthy and Peles [11] used 100 μm diameter circular pin fins in tall microchannels on a 1.8 mm × 10 mm

footprint area. Inlet flow restrictors were also used to stabilize the flow. The authors obtained a maximum heat flux of ~100 W/cm^2 over a range of flow rate and observed that the HTC increased with both heat flux and mass flux. The highest value of HTC obtained was about 60 kW/m^2°C in the saturated boiling region.

Qu and Siu-Ho [44] used an array of 200 µm square, staggered, micro-pin-fins with channel heights of 670 µm for their flow boiling study. The maximum heat flux obtained was ~250 W/cm^2 while the HTC varied from 50 to about 180 kW/m^2°C for mass fluxes in the range of 183 to 420 kg/m^{2}s. They reported a maximum pressure drop of about 70 kPa at the highest heat flux in another publication [45].

Hydrofoil shaped pin fins in flow boiling were extensively studied by Peles's group. Kosar et al. [46] used R-123 as their working fluid over circular and hydrofoil shaped pin fins of 100 µm chord length in their flow boiling study. The depth of the fins was 243 µm with a footprint of 1.8 mm × 10 mm on a silicon substrate (similar to their earlier works). They obtained high heat fluxes for R-123 fluid in the range of ~280 W/cm^2. However, they observed unstable flow and the pressure drop ranged from 8 to about 68 kPa.

Recently, Law et al. [47] used oblique fins in forty microchannels with 0.3 mm wide on a footprint area of 25 mm × 25 mm. FC-72 was used as the working fluid with an inlet temperature of 29.5 °C. For mass fluxes from 175 kg/m^{2}s to 350 kg/m^{2}s, they obtained heat fluxes in the range of 6 W/cm^2 to 120 W/cm^2. They were able to obtain low pressure fluctuations and stable flow with these fins. The authors also concluded that the nucleate boiling was the dominant heat transfer mechanism.

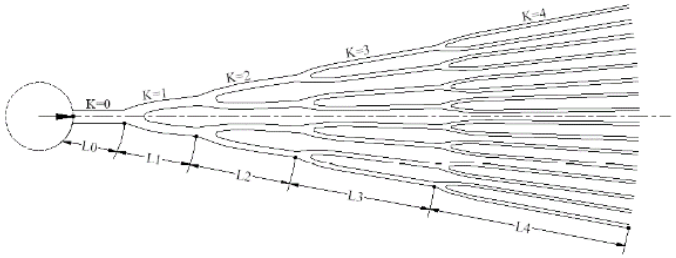

Figure 12: Schematic of the fractal-line microchannel [48]

Fractal microchannel [48] has also been studied as a method to mitigate flow instabilities as seen in Fig. 12. This structure is also a form of inlet restrictors. Low pressure drop was obtained in their study while the heat transfer performance was not discussed.

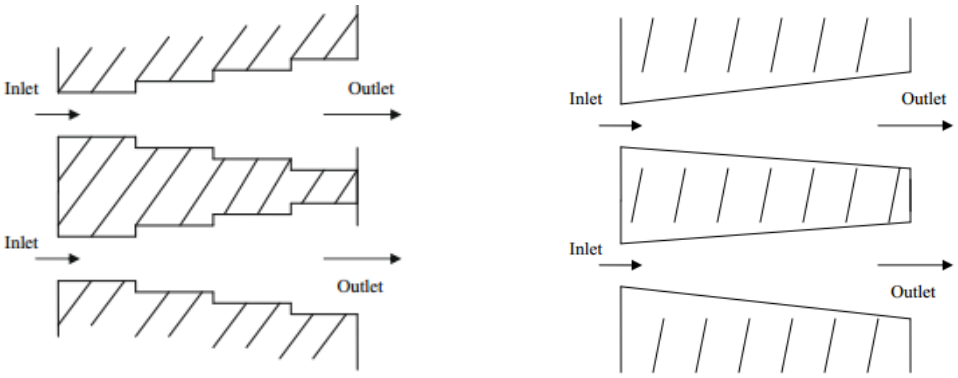

(a) (b)

Figure 13: Schematic of recommended microchannel design (a) Diverging microchannels and (b) stepped microchannels [36]

Mukherjee and Kandlikar [36] numerically simulated a nucleating bubble in a channel and studied the effect of inlet restrictors. They concluded that the reverse flow in microchannels occurs due to the pressure built up in the channels from rapid bubble growth. Higher flow resistance was observed in the downstream direction as compared to the upstream direction. The authors recommended that to obtain a unidirectional flow, the

microchannels should be designed with increasing cross-sectional area in the flow direction. Figure 13 below shows some of the recommended concept designs.

Lu and Pan [49] experimentally investigated the concept introduced by Mukherjee and Kandlikar [36]. The authors used diverging channels (see Fig. 14) with a diverging angle of 0.5°, an inlet width of 100 µm and an outlet width of 560 µm. Three types of geometries were investigated – Type 1: diverging channels, Type 2: diverging channels with artificial nucleation sites (ANS) at a downstream section of the channels and Type 3: diverging channels with artificial nucleation sites (ANS) equally spaced along the channel length. Type 3 geometries recorded the maximum heat transfer performance of 480 W/m^2 at a wall superheat of ~16 °C. The same configuration also recorded the highest pressure of ~40 kPa.

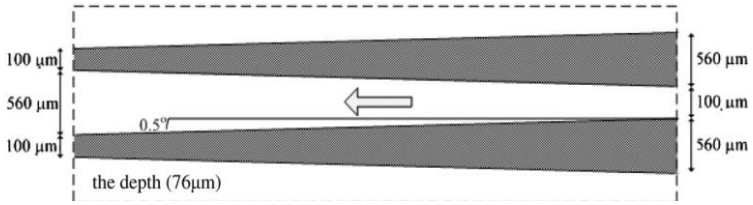

Figure 14: Schematic showing diverging parallel microchannels [49]

Microgaps have also been used in flow boiling [50,51] for improved cooling capability. Alam et al. [51] used ten different microgap sizes ranging from 80 µm to 1000 µm in their flow boiling study. The authors showed that microgaps below 100 µm were ineffective and encountered early CHF. The increase in gap size improved the heat transfer performance, however, a microgap over 500 µm recorded a high wall superheat. Reduction in pressure drop was also observed with increase in gap sizes.

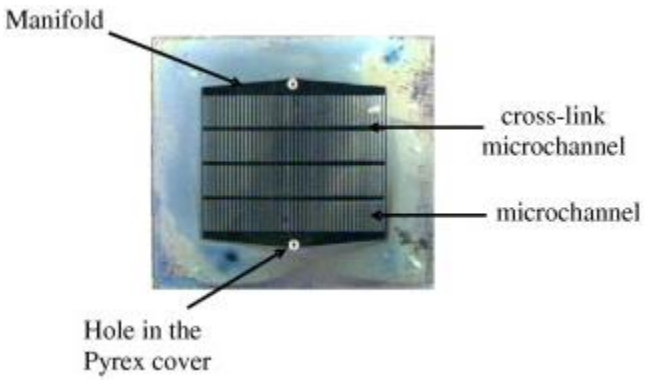

Figure 15: Schematic of the cross-linked microchannels [52]

Cross-linked microchannels have been used by various researchers [53,54] to obtain higher heat transfer performance. Megahed [52] used cross-linked microchannels, as seen in Fig. 15, at low mass fluxes in their work. The author obtained high heat transfer performance compared to straight channels with their geometry. However, the two-phase pressure drop obtained was also higher compared to straight channels due to the cross-link effects.

The concept of increasing flow cross-sectional area by Mukherjee and Kandlikar was experimentally investigated by Balasubramanian et al. [55] through the stepped fin microchannel geometry (Fig. 16). The cross-sectional area was increased by reducing the height of the microchannel in a stepwise fashion in the flow direction. The polycarbonate cover plate was flat and it sat above the left-hand side of the channels. The authors used subcooled de-ionized water at 90 °C and the liquid flow direction was from left to right. The copper microchannel geometry consists of two steps and forms three regions. The microchannel height at the entrance was 1.2 mm, and it reduced to 800 µm and 400 µm in subsequent steps for all their geometry. Three geometries were tested having the overall dimension of 25 mm × 25 mm (SMFC1) with lengths of each section as 15 mm – 5 mm –

5 mm, 20 mm × 10 mm (SMFC29) with lengths of each section as 9 mm – 7 mm – 4 mm and 20 mm × 10 mm (SMFC25) with lengths of each section as 5 mm – 5 mm – 10 mm. The authors also tested with five different mass fluxes ranging from 98 kg/m^{2}s – 664 kg/m^{2}s. A maximum heat flux of around 420 W/cm^2 at a mass flux of 664 kg/m^{2}s was obtained for the SMFC29. A pressure drop of 3.5 kPa was recorded at the maximum heat flux. The authors observed minimum pressure drop fluctuations and obtained stable boiling at high heat fluxes.

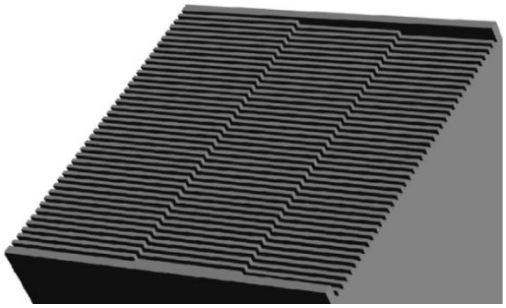

Figure 16: Schematic of the stepped microchannel [55]

A vapor venting technique using a hydrophobic membrane was first introduced by David et al. [56]. They used a porous PTFE membrane to cover the microchannel heat sink to extract the vapor. The vapor was then extracted to another microchannel on the other side of the membrane. Both microchannel sets were 130 µm wide, 134 µm deep and had 19 channels. The PTFE membrane had an average pore diameter of 220 nm and was the key component in their system. A maximum heat flux of 80 W/cm^2 was dissipated in the vented device and the authors also developed a pressure drop model that accurately predicted the pressure drop for their device.

Fazeli et al. [57] also used a similar hydrophobic vapor-permeable membrane in their flow boiling study. Pin fins were used to support the PTFE membrane. The authors were

able to enhance CHF and dissipate high heat fluxes while operating at 1-2 orders lower magnitude compared to other studies. They dissipated a heat flux of 380 W/cm^2 with a wall superheat of around 26 °C. The authors recommended further optimization of the membrane pore size, fin spacing and liquid irrigation pathways for improvement of heat transfer performance.

Recently, Miner et al. [58,59] studied the effect of microchannel cross-section expansion on flow boiling performance using R134-a. Three different expansion angles (0.5°, 1° and 2°) were used and compared with straight channels (0°). A maximum heat transfer rate was obtained with a 2° expanded microchannel. Significant decrease in pressure drop was also observed with this geometry. The mass flux was varied from 430 kg/m^{2}s to about 1500 kg/m^{2}s. The inlet subcooling varied form about 0.8 °C to 4.7 °C. The highest performance was recorded at 489 W/cm^2 with the 2° taper operating with a mass flux of around 1000 kg/m^{2}s. The authors also conducted analytical work [60] to support their experimental results.

2.2 Summary of Literature Review

The literature review presented above focuses in on flow boiling in microchannels using water as the fluid medium. In particular, the literature review section focused on the flow instabilities encountered during a flow boiling system. A summary of the literature review is presented below and this discussion forms the basis for the objective of this work.

1. Flow instabilities – The rapid bubble growth of the bubble in a channel causes the bubble to expand in both upstream and downstream directions. This in turn causes flow reversals, early CHF, and in some cases introduction of vapor in the inlet manifold region. The combination of the above leads to an unstable flow boiling system. Various researchers have observed these instabilities in their study.
2. Mitigating techniques – Various techniques were discussed to overcome the flow instabilities. Inlet restrictors and artificial nucleation sites were the most commonly used technique. These techniques assist in providing a stabilized flow, however they introduce a significant pressure drop. Recently, providing increased flow cross-sectional area has garnered a lot of attention.
3. Size and material – Common sizes reviewed for a heater surface varied between 10 mm – 25 mm. Most of the research is done on flat, horizontal (orientation) surfaces. Increase in surface area causes the issue of increase in power requirement to provide high heat fluxes. Copper and silicon are the most commonly used surfaces. For cost saving purposes, aluminum can also be used.
4. High heat dissipation – The goal of the flow boiling system is to dissipate high heat fluxes at low wall surface temperature. The system should provide high CHF with

high HTC. Increasing only CHF or heat flux is possible but the critical challenge lies in meeting this objective under a wall superheat constraint.

5. Low pressure drop – Reduction in pumping power helps in conserving energy, while maintaining a constant saturation condition along the channel reduces instability. Vapor blockage in the channel causes flow reversal and high pressure fluctuation. A technique which removes a bubble after its nucleation and clears the channel can provide high heat transfer and extend CHF.
6. Visualization – Visualization is required to understand the underlying mechanism occurring during the entire process. With the current research trend of mechanistic approach to flow boiling enhancement, visualization becomes critical. It also helps in forming flow pattern maps.
7. Pressure drop modeling – Theoretical understanding of the pressure drop is extremely important and provides predictive tools. Comparison with existing literature helps in providing confidence in the experimentally obtained data.
8. Critical heat flux – CHF marks the end of boiling as an efficient heat transfer process. Flow boiling in microchannels suffers from low CHF values. Extension of CHF is an important research area for multiple industries (nuclear and power generation). Different researchers have found different correlations to fit their heat transfer data. This discrepancy is due to the wide range of flow parameters involved.

2.3 Research Objectives

Based on the literature review, it was identified that a flow boiling system which provides a high heat transfer coefficient and high heat flux at low pressure drop is required. Microchannels have shown a lot of potential but due to flow instabilities, early CHF and a low heat transfer coefficient have not been able to deliver the required cooling performance.

The aim of the current study is to develop a new mechanistic approach for flow boiling in microchannels. The previous enhancements in microchannels which include artificial nucleation sites, reentrant cavities, micro pin-fins, and diverging channels have assisted in reducing flow instability. However, the heat transfer performance is still significantly low ($\leq$200 W/cm^2). This study will examine heat transfer, pressure drop, and flow visualization of water along the new geometry. With this new approach to heat transfer mechanism, a heat dissipation of over 1000 W/cm^2 is predicted. The goal of high heat dissipation will be accomplished with high heat transfer coefficient and low pressure drop constraints. Experiments will be performed for a wide range of influencing parameters such as flow rates, heat flux, and geometrical parameters to study their effect on flow boiling heat transfer and pressure drop performance.

High speed visualization will be conducted to clearly explain the underlying heat transfer mechanism for the new configuration. It will also provide flow regimes and flow pattern maps. Comparison of the bubble ebullition cycle with traditional microchannels and the new geometry will be presented.

The experimental observation will be substantiated with the pressure drop modeling for the new geometry. This will provide us with a theoretical understanding of the pressure drop components and their effects on various experimental parameters. Experimental data will be compared with the new pressure drop model.

Critical heat flux values for the new geometry at varying flow rates will be obtained through the experimental work. The heat transfer coefficient experimental data will be compared with existing models in literature.

Chapter 3: Experimental Setup

3.1 Proposed Design - OMM Geometry

Flow boiling instability and early CHF condition have been identified as a limiting factor in microchannels through the literature review section. Previously, Mukherjee and Kandlikar [36] suggested several diverging and stepped microchannel designs to overcome this problem. Since these designs are difficult to implement, a new open microchannel with manifold design is proposed. The main concept of the new geometry was to provide additional area for the expanding bubbles in the microchannels. This additional area was provided through the manifold region. The manifold design can be uniform (no taper) or tapered. For the uniform manifold, the microchannels have an open area above them as seen in Fig. 17. The issue with the closed microchannels is that the liquid and vapor occupy the same area, and this eventually leads to certain sections of the channel undergoing dryout. With the addition of the increased area, liquid would have easier access to the heater area, while the vapor will be in the manifold region (additional area).

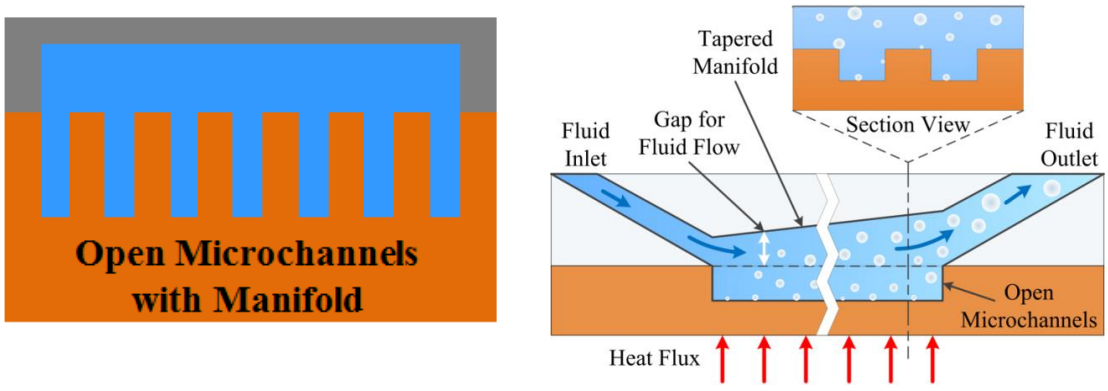

Figure 17: Schematic of the open microchannels with uniform and tapered manifolds

A modification to the uniform manifold design was the tapered configuration. A taper design provides a gradual increase in area from the inlet to the exit section as seen in Fig. 17b. A similar conceptual idea to uniform area in terms of increasing available area, the additional aspect was providing a direction of flow to the vapor in the manifold region. The tapered manifold with open microchannel design also addresses the two factors responsible for low CHF – removal of the vapor from the heat transfer surfaces and supply of liquid to the nucleation sites. The extra flow area provided by the manifold above the microchannels is helpful in removing the generated vapor without an excessive pressure drop penalty. Since vapor generation increases in the flow direction, a tapered manifold provides the extra space downstream for the vapor to flow away from the heat transfer surface. Finally, the open microchannel configuration has been shown to be very effective in enhancing pool boiling heat transfer [61], and is expected to provide similar enhancement under flow boiling conditions in the present OMM configuration.

The main disadvantage of the inlet restrictors and the tapered microchannels is the added pressure drop. The OMM design offers a lower pressure drop due to the availability of additional flow area. One of the key aspects of this design is that the microchannels promote nucleation and boiling heat transfer, while the open manifold region provides a path for the vapor to flow without adversely affecting the liquid flow to the nucleating cavities and the heat transfer regions inside the open microchannels.

3.2 Experimental Flow Loop and Data Analysis

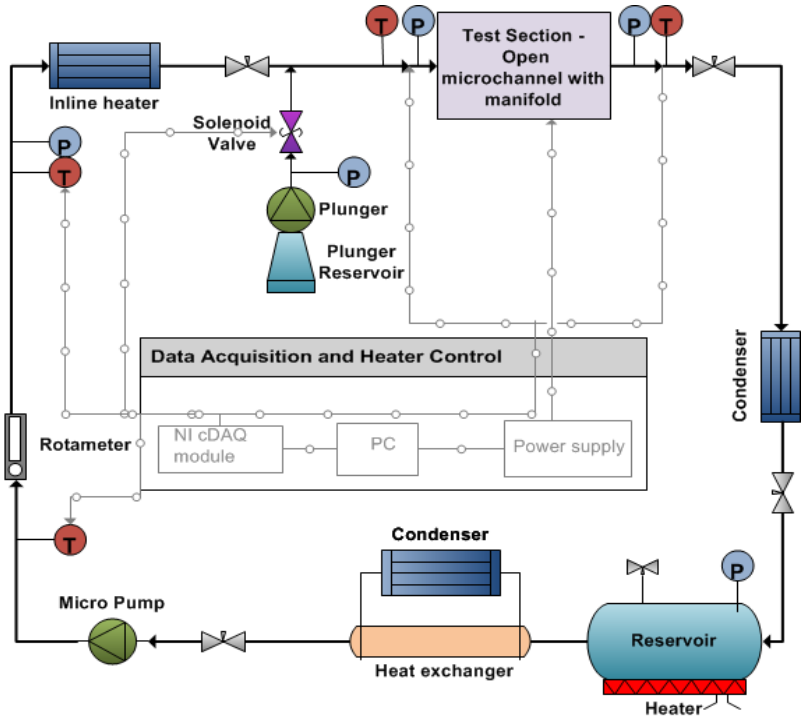

Figure 18: Schematic of the flow boiling test setup loop

Figure 18 shows the schematic of the experimental flow boiling setup. A five gallon pressure canner served as the reservoir for the distilled water. A hot plate was used to vigorously degas the water before the start of each test run (degassing procedure explained below). A Micropump® was used to drive the water through the entire loop. A heat exchanger was placed before the Micropump® to reduce the temperature of the water going through it. The flow rate was controlled through a rotameter and was varied between 40 – 350 ml/min for the current work. The water at a set flow rate would then enter the inline heater. The inline heater provided the desired inlet temperature to the test section. A subcooling of 10°C was provided in this work. The heated water would then enter the test

section and the mixture of water + steam would exit. The mixture would then be cooled by the condenser and the liquid would renter the reservoir.

3.1.1 Working fluid

For the current work, distilled water was used as the working fluid. Water was chosen for its superior thermal properties, non-toxic nature and ease of availability. Water has also been used by various researchers (as seen in literature review section) in their respective flow boiling studies, allowing direct comparison of current boiling performance with other studies. Use of other fluids (alcohols, refrigerants and binary mixtures) and its performance are further discussed in the ethanol study and future work sections.

3.1.2 Degassing procedure

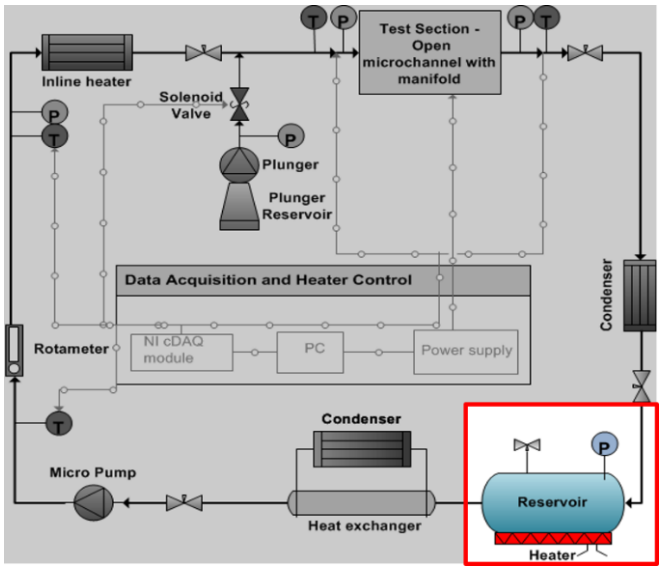

Figure 19: Schematic of the flow boiling test setup loop focusing on the degassing procedure

Dissolved gases are present in water and can hinder the thermal performance of the boiling system. Air will diffuse in a liquid (exposed to atmosphere) due to the natural

diffusion phenomena. Presence of these dissolved gases causes boiling to occur at temperatures lower than the actual saturation temperature of the liquid. This could impact the heat transfer and pressure drop performance of the system. A degassing procedure was used prior to each test run. The procedure followed was recommended by Steinke and Kandlikar [62]. The pressure canner is first heated up to 2 atm absolute pressure (121°C saturation temperature). Once the pressure is obtained, the deadweight is removed and the chamber is allowed to cool down to atmospheric pressure (Fig. 19). The dissolved gases are forced out of the canner with the steam. This procedure is repeated twice before the liquid enters the test loop.

3.1.3 Auxiliary cooling loop

Auxiliary cooling was provided in the system for cooling the system at CHF. At CHF, the vapor covers the surface and does not allow any liquid water to rewet the surface. The surface temperature drastically increases due to this factor and in certain cases the high temperature could melt the surrounding components and compromise the structural integrity of the system. In the current system, a higher pressure water reservoir (room temperature) in combination with a solenoid valve is used as the cooling unit. A 7.6 L (2 gal.) plunger was used to manually pressurize the CHF loop. The reservoir is pressurized to ~100 kPa (~15 psi) but, over the period of 5 hours of testing, some reduction in pressure is observed.

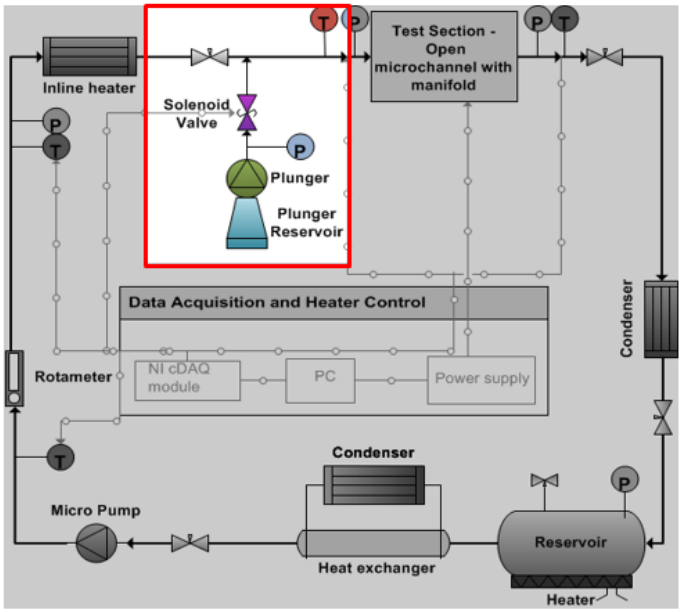

Figure 20: Schematic of the flow boiling test setup loop focusing on the auxiliary cooling loop

The reduction in pressure does not affect the performance of the cooling unit, since the pressure drop in the channel region is close to 1 psi. The solenoid is controlled via NI DAQ system, which has a maximum temperature limit setting. CHF leads to a temperature spike, which in turn activates the solenoid valve and releases the high pressure cold water in the system. The high pressure water immediately removes the vapor covering the heated surface and drastically reduces the surface temperature, thus preventing any damage to the system.

3.1.4 High-speed flow visualization

High speed visualization was accomplished with a Photron 1024 Fastcam CMOS camera and a 150 mm Nikon lens. Additional light required for imaging was provided using a Dolan-Jenner Fiber-lite MH-100 metal halide Machine Vision illuminator lamp.

The images were taken at 3,000 – 10,000 frames per second (fps). However, for most of the experiment, test videos were recorded at 3000 to 6000 fps to allow for a higher resolution, covering a larger area of the surface of the chip. The polysulfone manifold block was polished to a transparent finish to facilitate visualization. A Fiber-lite light source was placed near the manifold block to illuminate the chip surface and enable the camera to provide quality images. The high-speed camera was mounted to a 3-axis motor assembly, featuring 3 electric motors capable of moving the camera in 3 different axes (x-y-z). The Photron FASTCAM Viewer software was used for image optimization; it allows the user to select frame rate, shutter speed, and resolution settings, as well as the adjustment of brightness, contrast, and gamma level.

3.1.5 Sensors and data acquisition system

The system used multiple temperature and pressure sensors at various locations. For the temperature sensor, k-type thermocouples were used. All thermocouples were calibrated using an OMEGA Hot Point® Dry Block Probe Calibrator for operating temperature range. Details of the calibration and the calibration plots are discussed in the appendix section. A differential wet/wet Omega pressure transducer was connected between the inlet and the outlet of the test section to measure the pressure drop across the test section. The pressure transducer was calibrated using an OMEGA DPI 610 Pressure Calibrator and the calibration details are discussed in the appendix section. The pressure canner had a pressure (dial) gauge attached to it and was used for degassing procedure only while a pressure gauge was attached in the auxiliary cooling loop to provide the pressure reading from the plunger reservoir. Pressure gauges were used in the above mentioned

system, since the accuracy was not critical and the pressure data was not recorded for further calculations.

The Data Acquisition System (DAQ) used in this work was from National Instruments (NI) and a LabVIEW program was created to read and log all readings. An NI CompactDAQ-9174 4-slot USB chassis was selected. A pressure card (NI 9239) and a temperature card (NI 9214) were used for pressure and temperature measurements respectively. Data was logged for a time span of 10 sec at each heat flux. Each data point was recorded after a minimum waiting period of 10 min once steady state was reached at each heat flux. Steady state was reached at the point at which temperature changes fall below $\pm$0.2°C within a 10 sec time period. The LabVIEW VI also controlled the power supply and the auxiliary cooling loop. The VI was automated to release the cooling loop if the surface temperature exceeded beyond 140°C. This was done to prevent structural damage to the test section.

3.3 Heater and Test Section

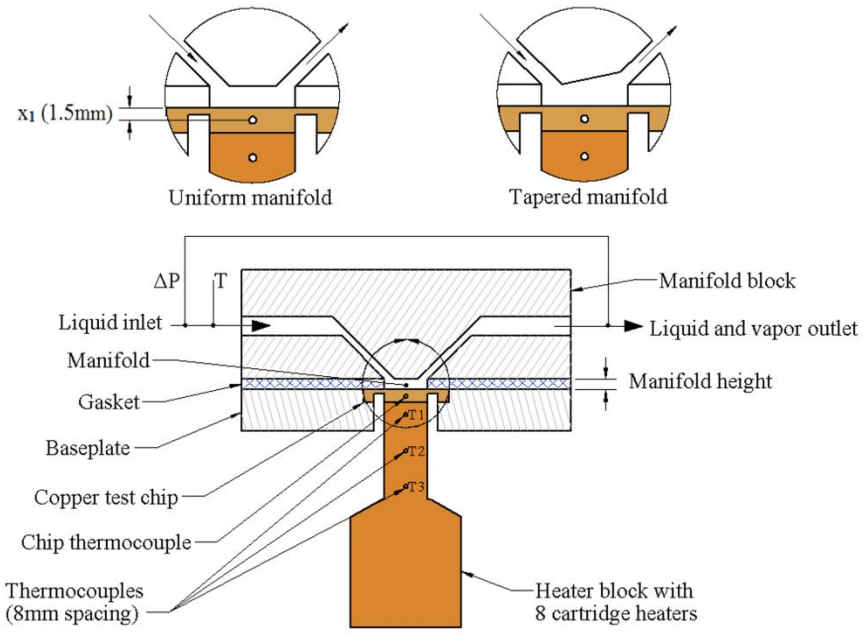

Figure 21: Schematic showing the uniform and tapered manifolds with the heater configuration (not to scale)

The heater section consisted of a copper block (C101 – oxygen free) with four cartridge heaters at the base section. The four 400 W cartridges were inserted into the copper heater and were connected to a 300 V, 5 A power supply. The middle portion of the heater consisted of three equidistant 5 mm deep thermocouple holes. 3 k-type thermocouples were press fitted into these holes and were used to measure the temperature gradient from the base to the test section. The temperature gradient was calculated using the three points, backward Taylor series approximation:

$$\frac{dT}{dx} = \frac{3T_1 - 4T_2 + T_3}{2\Delta x} \tag{2}$$

This temperature gradient was further used in calculating the heat flux which, in turn, was calculated using the one dimensional heat transfer equation, Fourier's Law:

$$q''_{eff} = -k_{Cu}\frac{dT}{dx} \tag{3}$$

Where k – thermal conductivity of copper (391 W/m K) and q_{eff}" is the effective heat flux. The effective heat flux was a difference between the actual heat flux and the heat losses. The entire copper heater was surrounded by ceramic to reduce the heat loss. The details of the heat loss study are provided in the appendix section. Briefly, a numerical simulation on Fluent was conducted to determine the heat loss to the surrounding. It was determined that 4-6 W were the heat loss values for a typical test run.

The surface temperature (T_s) was calculated through extrapolation and by using the known heat flux value and known distance (x_1) between the top thermocouple (T_1) and the surface. Rearranging Eqn. 1, the equation for surface temperature was obtained.

$$T_s = T_1 - q''\frac{x_1}{k_{Cu}} \tag{4}$$

The heat transfer coefficient was calculated from the surface temperature and the heat flux, based on the projected area of the heater base, and is given by Eqn. (5).

$$h = \frac{q''}{\Delta T_{sat}} = \frac{q''}{(T_s - T_{sat})} \tag{5}$$

Two surfaces were used as test sections: one plain surface and the other with microchannels. The active region for both surfaces was limited to a central 10 mm x 10 mm area. The microchannels were CNC milled and had a channel width of 217 μm (200 μm), fin width of 160 μm (200 μm), channel depth of 162 μm (200 μm) and length of 10 mm giving a hydraulic diameter of 185 μm for the microchannels. The dimensions of the

microchannels were selected from a previous work from Cooke and Kandlikar [63] and keeping within the channel classification for microchannels (200 µm > D_h > 10 µm). In the current study, the focus was not on obtaining the optimum channel dimension, hence the various geometrical parameters (channel width, fin width and channel depth) were not investigated. However, effects of these parameters have been studied in literature by various researchers. Harirchian and Garimella [24] studied the effect of channel width in their flow boiling study. They reported that the flow regimes and thermal performance for microchannels with 400 µm width and greater were similar, while microchannels with width less than 400 µm showed similar performance.

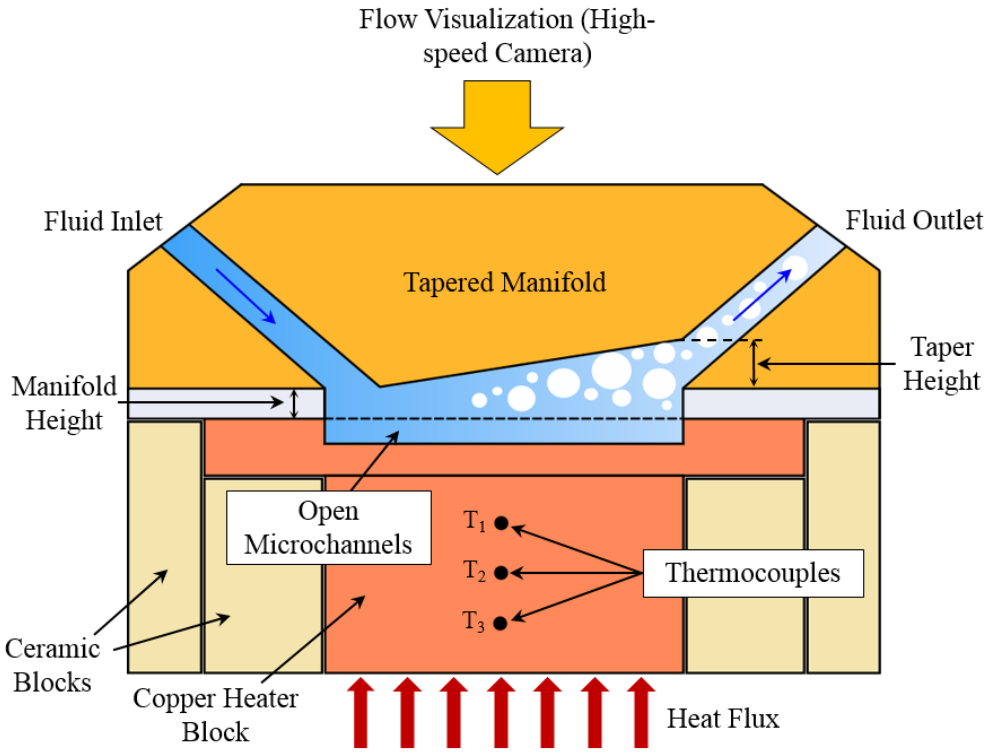

Figure 22: Schematic of the tapered manifold with heater geometry

3.4 Manifold Blocks

An in-depth study was conducted for the material selection of the manifold blocks. The manifold block needed to have the following properties: (1) Easy to machine – The block would have inlet and exit pathways, taper and additional through holes for assembly of the system. (2) High temperature resistance – The block would be in contact with high temperature liquid and steam for a long duration. (3) Transparent – Flow visualization was an important part of the study. Initial tests were conducted using Lexan (polycarbonate) due to the availability of the material, ease of machining and transparent nature. However, due to the low glass-transition temperature of the material (~90°C), the region above the active area of the surface started softening and thus compromising the integrity of the taper. Polysulfone was selected due to the high temperature resistance, machinability and reasonable cost. Polysulfone had to be polished to improve the transparency for flow visualization with the high speed camera.

Two types of manifolds (Fig. 23) were employed: the uniform manifold which had a flat surface without any recess in the block, and the tapered manifold, which provided a tapered gap above the microchannels from the inlet to the outlet.

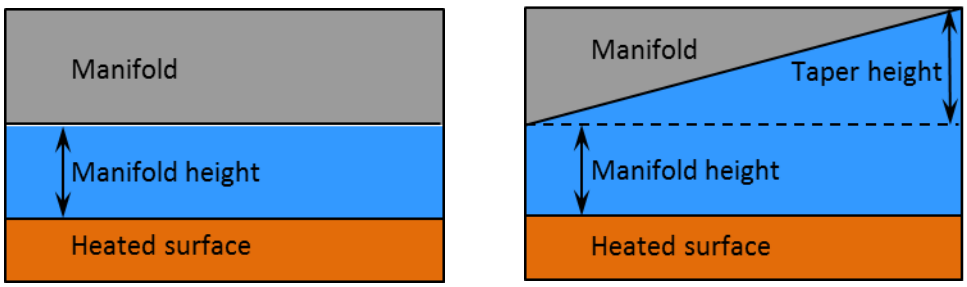

Figure 23: Schematic of the two types of manifold block (i) Uniform manifold (ii) Tapered manifold

Three different tapers were used in the current study and the taper gradient percentage was calculated as taper height over the heated length of 10 mm. The details of the manifold used in the current work are shown in Table 1.

Table 1: Manifold configuration details over a 10 mm long heated section for an inlet height of 127 μm.

Manifold	Taper height (μm)	Inlet height (mm)	Exit height (mm)
Uniform	0	0.127	0.127
Taper Gradient 2%	200	0.127	0.327
Taper Gradient 4%	400	0.127	0.527
Taper Gradient 6%	600	0.127	0.727

All the blocks were machined at the RIT machine shop using standard milling machine operations.

3.4.1 Manifold height

In both cases (uniform and tapered manifold) the manifold height was controlled by inserting an aluminum shim gasket of desired thickness between the chip and the manifold block. Five gaskets of thicknesses 0.127 mm, 0.254 mm, 0.508 mm, 1.016mm, and 1.524 mm were used to provide the desired manifold height over the microchannels.

A secondary compressible silicone gasket was also used to limit the heat transfer area to the microchannel region. A 10 mm × 10 mm opening in each gasket was aligned over

the 10 mm × 10 mm microchannel region to inhibit contact between the working fluid and the outer edges of the test chip. The active area of the chip was thus defined by the square opening in the gasket over the chip region with microchannel features. This secondary gasket also assisted in sealing the system.

3.5 Uncertainty Analysis

An uncertainty analysis is critical to an experimental work in order to have the recorded data closest to its fullest value. The Journal of Heat Transfer (JHT) - ASME standard for determining experimental uncertainties were followed in this work. The total uncertainty comprises of two parts; bias error and precision error:

$$U = \sqrt{B^2 + P^2} \tag{6}$$

The bias error also referred to as the systematic error is an estimate of the fixed, constant error. The precision error is the measure of random errors and unsteadiness. The following table list of measured parameters in the current work.

Table 2: Measured parameters in the flow boiling system

Parameter	Symbol	Units
Temperature	T	°C
Thermocouple distance	Δx	m
Thermal conductivity	k	W/m°C
Microchannel width	w	m
Microchannel fin width	f	m
Microchannel depth	d	m
Microchannel flow length	l	m
Volumetric flow rate	Q	m^3/s
Pressure drop	ΔP	kPa

Temperature uncertainty was determined through thermocouple calibration and 2 times standard deviation of a large sample (50 readings for a given temperature) for precision uncertainty. JHT is not specific about the number of sample readings and mentions only a

large sample reading (>30) to be taken for precision error measurement. The distance between the thermocouples (Δx), microchannel width, fin width, depth and flow length were determined using the laser confocal microscope. The accuracy of the laser confocal laser was 0.01 μm. Volumetric flow rate was obtained through the bucket method. It involved measuring the volume of fluid for a given time period. The scale used for measuring had an accuracy of up to 0.0001 g and the process was repeated 5 times for a given volume to taken into account any uncertainty due to human error (logging time). The total uncertainty in pressure drop was calculated as the sum of the bias uncertainty in measurement, obtained from the pressure sensor calibration, and the precision error, calculated from the standard deviation of samples of each data point.

Uncertainties for calculated values such as heat flux, surface temperature and heat transfer coefficient were determined using error propagation analysis given by the equation below:

$$U_p = \sqrt{\sum_{i=1}^{n} \left(\frac{\partial p}{\partial a} u_{ai} \right)^2} \tag{7}$$

where U_p is the uncertainty in the calculated parameter p and u_{ai} is the uncertainty of the measured parameter a_i. The uncertainty in any parameter is the sum of the components uncertainties used in that parameter. The total uncertainty in heat flux was derived using Eqn. (6) and is shown below.

$$\frac{U_{q"}}{q"} = \sqrt{\frac{{U_{k_{Cu}}}^2}{k_{Cu}^2} + \frac{{U_x}^2}{\Delta x^2} + \frac{9{U_{T_1}}^2}{\alpha^2} + \frac{16{U_{T_2}}^2}{\alpha^2} + \frac{{U_{T_3}}^2}{\alpha^2}} \tag{8}$$

In Eqn. (8), the total uncertainties in the three temperature values were obtained from the combination of bias and precision errors of their respective measurements. The total uncertainty in the heat transfer coefficient (U_h) was derived in terms of uncertainties in q" and surface and saturation temperatures using Eqn. (8) and is shown below:

$$\frac{U_h}{h} = \sqrt{\frac{U_{q"}{}^2}{q"^2} + \frac{U_{T_w}^2}{\Delta T_{sat}^2} + \frac{U_{T_{sat}}{}^2}{\Delta T_{sat}^2}} \tag{9}$$

Derivations for the above two equations 8 and 9 are provided in the appendix section. The total uncertainty in heat flux was consistently below 5% at high heat fluxes. The total uncertainty in heat transfer coefficient remained within 8% on average, with maximum values below 5000 W/m^{2}K. The total uncertainty in pressure drop was within 10%, though this uncertainty was predominantly caused by pressure drop fluctuations, leading to a large precision error. The bias error in pressure drop was very low due to high sensor accuracy. The uncertainty in wall temperature was consistently below 0.5%. At the highest flow rate the rotameter had an uncertainty of 3%, and at the low flow rate the uncertainty was 5%.

Chapter 4: Experimental Results With Uniform and Tapered Manifold

This chapter is divided into two parts, namely uniform manifold study and tapered manifold study. The first parts focuses on the experimental result obtained using a uniform manifold with a plain and microchannel chip for five different gaskets and five flow rates. These tests form the baseline for the OMM design. The second part focuses on the experimental study with tapered manifold using three different taper gradients with a single flow rate and height size. The results in the second study are compared with uniform manifold. Key takeaways in the form of conclusions are presented at the end of each study. For the boiling performance (uniform and tapered manifold), heat flux was calculated using Eq. 1 for a heater area of 100 mm^2.

4.1 Uniform Manifold Study

4.1.1 Uniform manifold with open microchannel and plain chip

The characterization of the OMM geometry was conducted by evaluating difference in plain and microchannel chip performance for the same gasket and flow rate. These configurations formed the baseline for the OMM design. The heat transfer performance was given in the form of the boiling curve with heat flux on the y-axis and wall superheat on the x-axis. Figure 24 shows the boiling curves for two flow rates, A = 333 mL/min, and B = 225 mL/min, a uniform manifold with spacing S = 0.254 mm for the plain and microchannel test chips. The microchannel chip performed significantly better than the plain chip for both flow rates. The plain chip dissipated 100 W/cm^2 at a wall superheat between 20 and 25 °C, and CHF was reached at this heat flux. The microchannel chip

dissipated over 255 W/cm^2 at 14.1 °C wall superheat for a flow rate of 225mL/min without reaching CHF. As the flow rate was increased to 333 mL/min, the performance slightly deteriorated, and the test was conducted only up to 140 W/cm^2. By comparison, at a wall superheat of 14.1 °C and flow rate of 225 mL/min, the plain test chip dissipated only 54.8 W/cm^2. Boiling curves for the plain test chip were unaffected by changes in the flow rate.

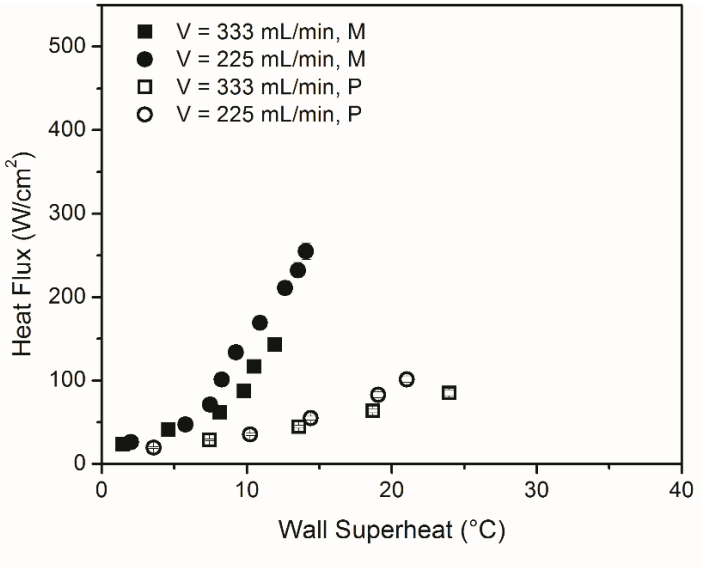

Figure 24: Comparison of boiling curves for microchannel and plain chips with uniform manifold and S = 0.254 mm at V = 333 mL/min and 225 mL/min

Surface area augmentation factor is one of the differences in the improved heat transfer performance between the two chips. The microchannel chip has an inherent surface area augmentation factor of 1.8 and therefore has 80% more area than the plain chip. The heat flux improvement beyond the area augmentation factor is due to the enhanced boiling mechanism in the present OMM configuration of open microchannels with a manifold. The introduction of the microchannel with uniform manifold causes differences in boiling behavior. When nucleate boiling occurs on a plain chip, the area surrounding a nucleation

site is obstructed by the vapor bubble and the effective wetted area of the chip is reduced. This is shown in Fig. 25 where portions of the plain chip under the nucleating bubble have dried out as seen from the lighter color in the marked region. The microchannel test chip avoids this problem by preventing large sections of the surface to be covered by a nucleating bubble. The geometry shows bubble nucleating activities in the channel while being underneath a vapor (see Fig. 25). The vapor occupies the additional area provided by the uniform manifold, while the liquid rewets the microchannel surfaces.

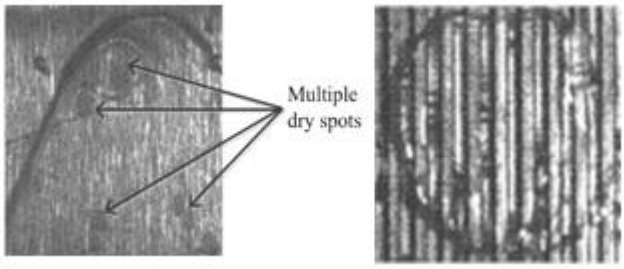

Figure 25: Plain surface showing dryspots (left image) and microchannel test chip (right image) under a bubble

4.1.2 Effect of manifold height

To study the effect of uniform height on flow boiling performance, five different gasket thicknesses (0.127 mm, 0.254 mm, 0.508 mm, 1.016mm, and 1.524 mm) were used. Boiling curves shown in Fig. 23 a-b were obtained with a constant flow rate of 333 mL/min and 152 mL/min respectively for the microchannel test chip, and the uniform manifold block.

For 333 mL/min, a maximum heat flux of 175 W/cm^2 at ΔT_{sat} = 13-15 °C was achieved using a manifold depth of 0.127 mm, 0.254 mm, 0.508 mm and 1.016 mm (Fig. 26 (a)). When the manifold depth was increased to 1.524 mm, the heat transfer performance drops significantly to a maximum heat flux of only 122 W/cm^2 at ΔT_{sat} = 22.0 °C. Figure 26 (b) shows the boiling curve with different manifold height for 152 mL/min. Comparable heat transfer performance is observed for three manifold heights of 0.127 mm, 0.254 mm and 0.508 mm with a maximum heat flux of ~190 W/cm^2. The smallest height (0.127 mm) showed the best performance with lower wall superheat. Similar to 333 mL/min, the maximum height of 1.524 mm showed significant performance deterioration. Similar conclusion of gap sizes have also been observed in literature [51].

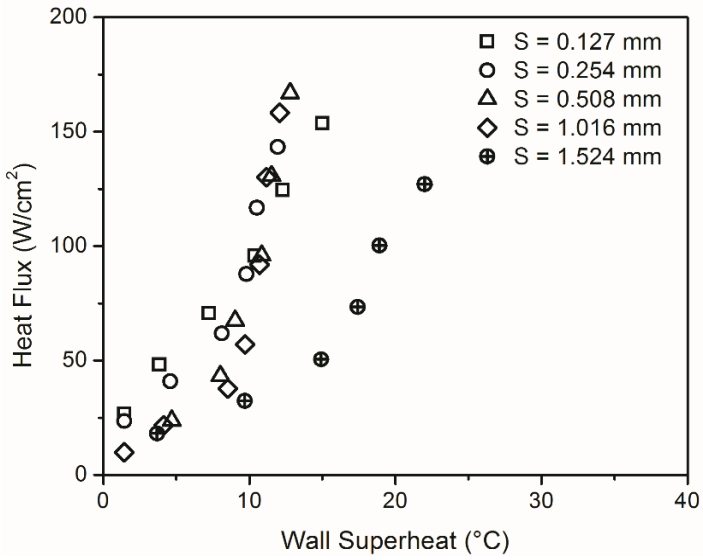

(a) 333 mL/min

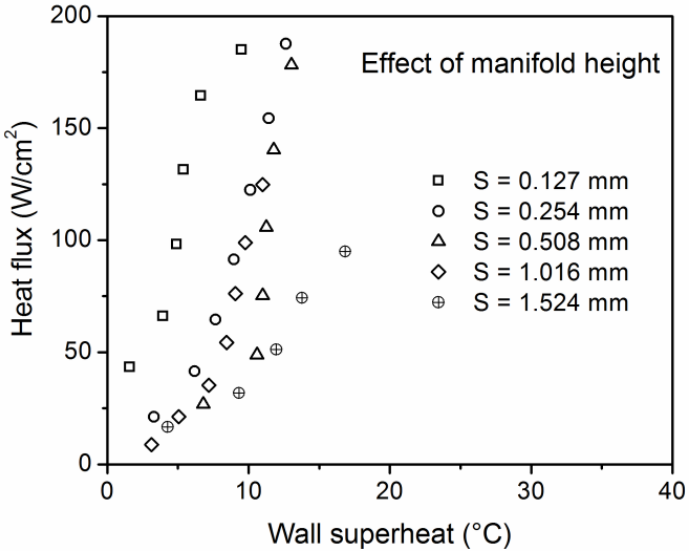

(b) 152 mL/min

Figure 26 a-b: Effect of manifold depth on boiling curves with the uniform manifold block and the microchannel test chip for two flow rates

4.1.3 Effect of flow rate

Three different tests were conducted with the uniform manifold in order to investigate the effect of flow rate and manifold depth on flow boiling performance. The first test run had a set manifold depth of 0.127 mm with five different flow rates (V = 333 mL/min, 225 mL/min, 152 mL/min, 80 mL/min and 40 mL/min) with a microchannel chip. The highest heat flux obtained for this manifold depth was 506 W/cm^2 at ΔT_{sat} = 26.2 °C with a flow rate of 152 mL/min as seen in Fig. 27. Tests using flow rates of 80 mL/min and 40 mL/min performed very similarly with no more than one or two degrees of wall superheat separating each test for any given heat flux. Higher flow rates of 333 mL/min and 225 mL/min showed reduced performance, as they typically had a ΔT_{sat} that was 5 - 10 °C higher than the other tests for any given heat flux. These test could have possibly achieved

higher heat fluxes. However, the tests were discontinued due to the increase in wall superheat. CHF was not reached in any of the tests.

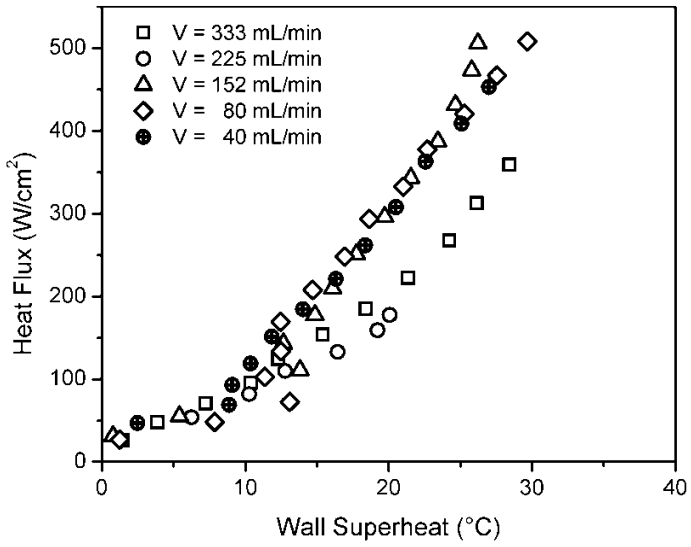

Figure 27: Effect of flow rate on boiling curves with a uniform manifold block and microchannel test chip with S = 0.127 mm and V = 333 mL/min, 225 mL/min, 152 mL/min, 80 mL/min and 40 mL/min.

The second set of tests used a manifold depth of 0.254 mm, a uniform manifold and a microchannel chip and the results are shown in Fig. 28. A maximum heat flux of 258 W/cm^2 at ΔT_{sat} = 14.6 °C was obtained with a flow rate of 152 mL/min for this configuration. The boiling curves for tests with flow rates of 225 mL/min and 152 mL/min have very comparable profiles, while the curve for 333 mL/min has a slightly lower heat flux for a given wall superheat in the low heat flux region. Higher heat fluxes could not be obtained as these tests were performed with an earlier version of the heater with a lower power rating.

These results show comparable performance with the previous manifold thickness of 0.127 mm. The performance can also be explained through similar mass fluxes at higher flow rates for S = 0.254 mm and lower flow rates for S = 0.127 mm.

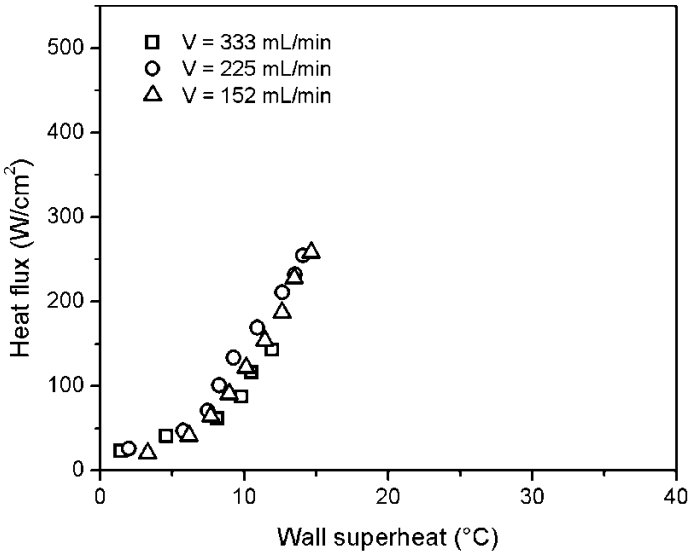

Figure 28: Effect of flow rate on boiling curves with the uniform manifold block and the microchannel test chip, with V = 333 mL/min, 225 mL/min, and 152 mL/min, and S = 0.254 mm

The final flow rate tests used a manifold depth of 1.524 mm, a uniform manifold and a microchannel chip (Fig 29). The flow rate of 333 mL/min produced the highest heat flux of 127 W/cm^2, and the boiling curve for each test was comparable in profile and performance. Only the lowest flow rate of 152 mL/min showed a slightly better performance. Performance with the manifold depth of 1.524 mm was substantially lower than those with the thinner manifold spacing.

The possible explanation for the drastic reduction in boiling performance can be explained through the reduction in mass flux and flow pattern. The flow pattern shows a

dominance of bubbly flow due to the large area provided, while in the case of a smaller height, annular flow dominates. Further, investigation is required through flow visualization.

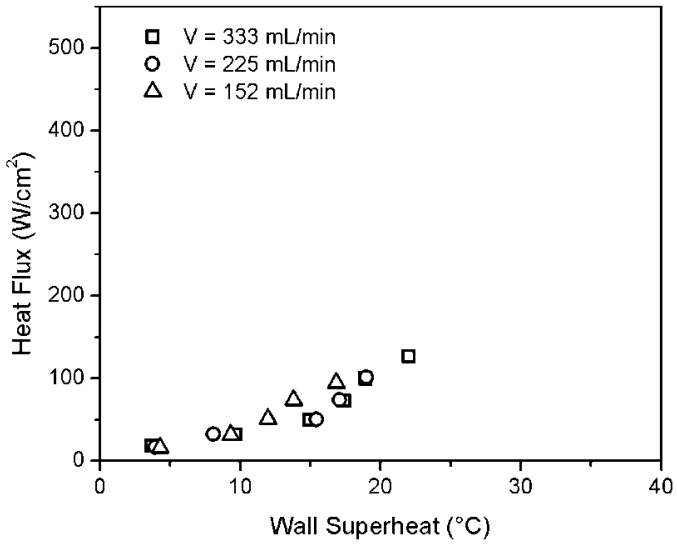

Figure 29: Effect of flow rate on boiling curves with the uniform manifold block and the microchannel test chip, with V = 333 mL/min, 225 mL/min, and 152 mL/min, and S = 1.524 mm

Figures 27 through 29 illustrate that flow rate has smaller effect on heat dissipation performance in comparison to manifold depth. Boiling curves were consistent across a wide range of flow rates for each depth, but manifold depths of 1.016 mm and thinner dramatically outperformed the largest depth of 1.524 mm throughout the range of heat fluxes tested.

4.1.4 Pressure drop concern

One of the constraints in obtaining high heat fluxes is having low pressure drop values. Low pressure drop allows for low pumping power and uniform saturation conditions along the channel length. Open microchannels with uniform manifold configuration can dissipate high heat fluxes >500 W/cm^2 with a high HTC of 193 kW/m^2°C. Figure 30 shows the pressure drop performance of the uniform manifold for varying flow rates at a heat flux of 400 W/cm^2 and a uniform height S = 0.127 mm. Pressure drop values were in the range of 25 kPa for low flow rate (40 mL/min). As the flow rate increased, the pressure drop also increased. For 152 mL/min, the pressure drop was in the region of ~75 kPa. At higher flow rates, further increment was observed.

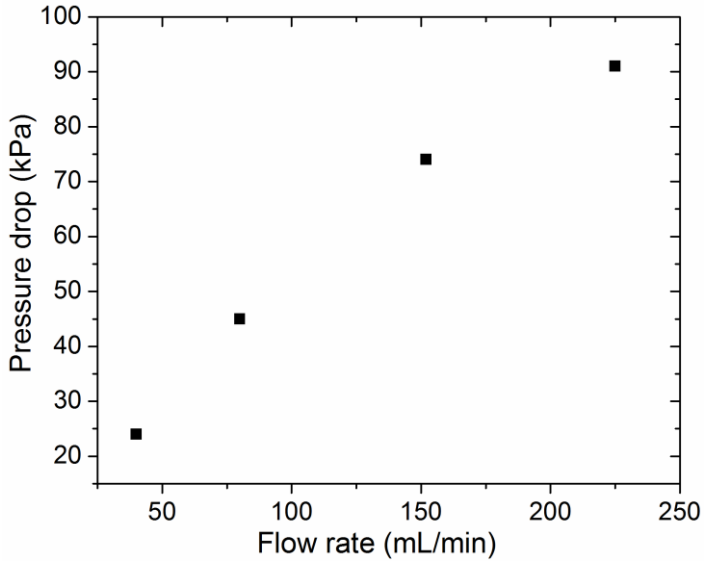

Figure 30: Pressure drop performance of varying flow rates for OMM with uniform height (S = 0.127 mm)

Open microchannel with uniform manifold can deliver high heat fluxes with low flow rates and small height size. However, there is a pressure drop penalty involved with the heat transfer performance. Furthermore, some backflow was observed with uniform gap. The introduction of taper can reduce the backflow and pressure drop. However, further investigation is required to evaluate the effect of taper configuration on pressure drop and heat transfer performance.

4.1.5 Conclusion – Uniform manifold study

A new flow boiling configuration with uniform gap is experimentally investigated. The experimental data shows the geometry is capable of achieving high heat fluxes with high heat transfer coefficient. The following conclusions are made from the study:

1. The open microchannel surface with uniform manifold shows a dramatic improvement in heat transfer performance over a plain surface with uniform height. Images from high speed video shows that liquid flow in microchannels and bubble expansion in the manifold region is one of the key reasons for performance enhancement.
2. Effect of manifold height was studied; five height sizes were evaluated ranging from 0.127 mm to 1.524 mm. 0.127 mm and 0.254 mm showed similar performance, with 0.127 mm height providing the highest heat flux of 506 W/cm^2. At higher flow rates, 0.127 mm to 1.016 mm had similar boiling curves. The largest manifold height of 1.524 mm had the worst overall performance.

3. A maximum heat flux of 506 W/cm^2 at a wall superheat of 26.2 °C was achieved using a uniform manifold with a spacing 0.127 mm, microchannel test chip, and a volumetric flow rate of 152 mL/min. Similar heat transfer performance was obtained with 80 mL/min, however the wall superheat was slightly higher.
4. Changes in volumetric flow rate for a given manifold depth have only a small impact on heat transfer performance. Varying the flow rates for manifold depths of 0.127 mm, 0.254 mm, and 1.524 mm produced similar boiling curves for each manifold depth.
5. Back flow was observed at low flow rates for uniform manifold. These flow reversals can be reduced with the introduction of tapered manifold.

4.2 Tapered Manifold Study

In this study, the focus is on the tapered manifold and reduction of pressure drop. Both uniform and tapered manifolds were again tested with the plain and microchannel chips. The pressure data was obtained using the differential pressure sensor. For all the test runs, the flow rate was kept constant at 80 mL/min, and a gasket of thickness 127 μm was used to provide a fixed height at the inlet manifold. The above two parameters were obtained from the uniform manifold study. The testing in the current study was limited to heat fluxes below 300 W/cm^2 due to heater limitations.

Three taper manifolds are introduced and compared with the previous uniform manifold. The configurations for the uniform and the tapered manifolds used in the current system are listed in Table 3. The inlet height remains constant for all test runs, while the exit height changed depending on the type of manifold used. Both the inlet and exit heights were referenced from the top plane of the microchannel to the top of the manifold. The mass fluxes at the inlet and outlet sections are calculated using the following equation:

$$G = \frac{\dot{m}}{A_c} \tag{10}$$

where the cross-sectional area A_c, is the actual flow area at a given section calculated as the sum of the total microchannel area and the manifold height area.

Table 3: Manifold configuration and mass fluxes at inlet and outlet for microchannel chip.

Manifold	Taper height (Outlet-Inlet height) (μm)	Inlet height (μm)	Exit height (μm)	Plain		Open microchannel	
				G_{inlet} (kg/m^2s)	G_{outlet} (kg/m^2s)	G_{inlet} (kg/m^2s)	G_{outlet} (kg/m^2s)
Uniform	0	127	127	1050	1050	372	372
Taper A	200	127	327	1050	408	372	238
Taper B	400	127	527	1050	253	372	175
Taper C	600	127	727	1050	183	372	138

The cross-sectional area at the inlet was the same for all manifolds (3.39×10^{-6} m^2), while the cross-sectional area at the exit for the tapered manifold varied depending on the taper height. The maximum exit quality observed in the current testing was below 0.1. The exit quality was calculated taking into the account the subcooling and was given by:

$$x = \frac{1}{h_{fg}}\left[\left(\frac{q''A}{\dot{m}}\right) - C_p\Delta T\right] \quad (11)$$

where q" is the heat flux, A is the projected area, $\dot{m}$ is the mass flow rate in kg/s, C_p is the specific heat of water, ΔT is the degree of subcooling and h_{fg} is the latent heat of vaporization.

4.2.1 Uniform manifold testing

The uniform manifold was tested with plain and microchannel chips first so as to establish the baseline results. The uniform manifold had a constant height provided by the gasket over the chip. Both the inlet and exit manifolds had a height of 127 μm in this case.

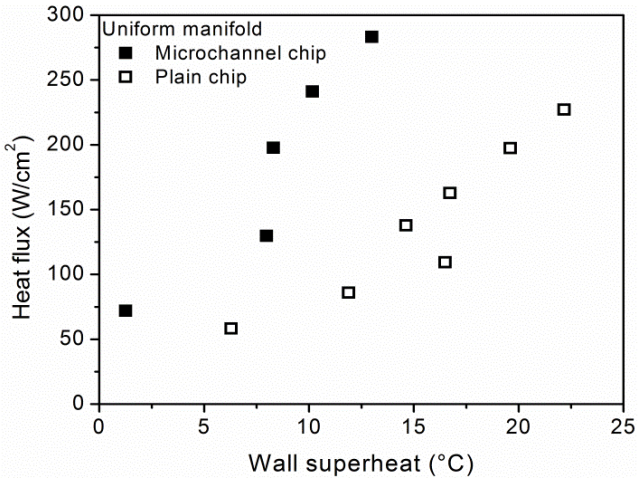

Figure 31: Boiling performance showing heat flux versus wall superheat for plain and microchannel chip with uniform manifold

Figure 31 shows the boiling performance of the two chips with the uniform manifold. The plain chip showed a slight boiling overshoot at a wall superheat of 17.7 °C. A maximum heat flux of 227.1 W/cm^2 at 22.1 °C wall superheat was recorded for the plain chip. The microchannel chip showed a similar overshoot but performed significantly better than the plain chip. A maximum heat flux of 283.2 W/cm^2 at a wall superheat of 12.9 °C was obtained. Testing was not continued at higher heat fluxes.

Figure 32 shows the heat flux and its corresponding pressure drop for the uniform manifold. The plain chip showed a pressure drop from 100 kPa at low heat fluxes to 158.4

kPa at high heat fluxes. The introduction of the microchannel chip does show a reduction in the pressure drop. At low heat fluxes, a pressure drop of 40 kPa is observed. For high heat fluxes, a maximum pressure drop of 62.1 kPa is seen at a heat flux of 250 W/cm^2. The overall pressure drop fluctuation for the microchannel chip increased with the increase in heat flux.

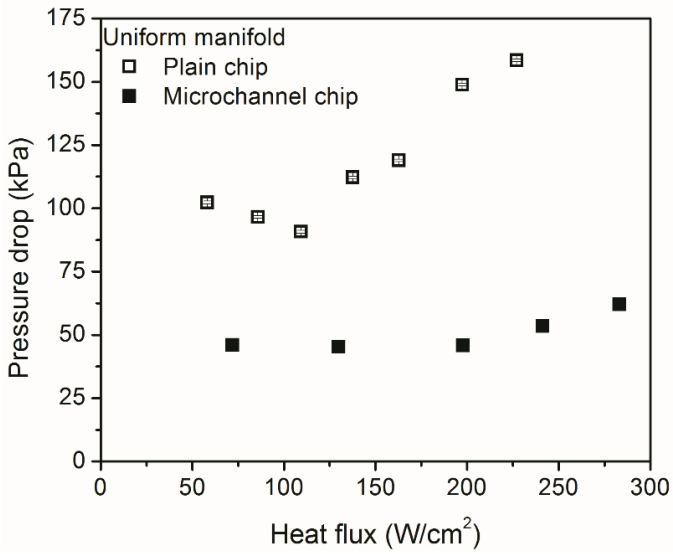

Figure 32: Pressure drop versus heat flux for plain and microchannel chip with uniform manifold

4.2.2 Tapered manifold testing

Tapered manifold was designed to provide additional flow area in the manifold along the flow direction to accommodate the vapor flow and reduce the pressure drop.

Figure 33 compares the boiling performance of the uniform and tapered manifold C for the microchannel and the plain chips. Expectedly, the microchannel chip performed better than the plain chip. The highest heat flux tested for the microchannel chip was 281.2 W/cm^2 at 10.1 °C wall superheat. For the plain chip, a maximum heat flux of 208.3 W/cm^2 at a

wall superheat of 15.6 °C was recorded. Boiling overshoot was not observed for both plain and microchannel chips.

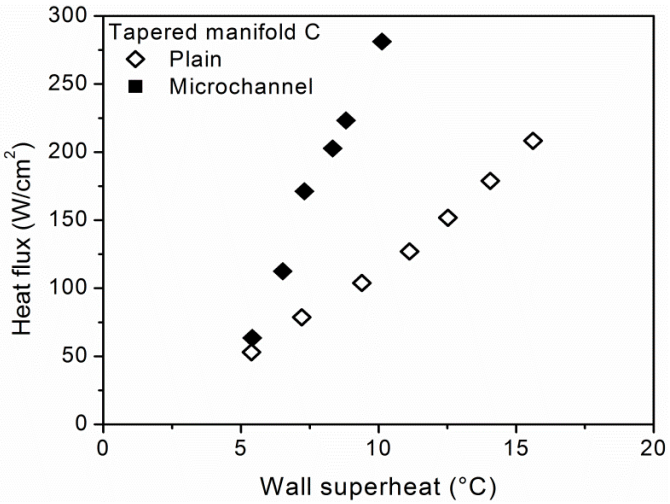

Figure 33: Boiling performance of plain and microchannel chip with the tapered manifold C

Figure 34 compares the pressure drops for the tapered manifold C for the microchannel and the plain chip. The effect of the tapered manifold is significant in terms of the pressure drop reduction over the uniform manifold for both chips. The plain chip shows a maximum pressure drop of 6.3 kPa at a heat flux of 208.3 W/cm^2, while the microchannel chip showed a pressure drop of around 2 kPa for a similar heat flux. The solid points shown on the graph are the average values over the pressure range. At intermediate heat fluxes, small negative values of pressure drop are seen. However, it is quite infrequent and insignificant and is not affecting the heat transfer performance adversely. Further, no back flow was observed during these tests. The plain chip shows an increasing trend of pressure drop with the heat flux, while the microchannel chip shows only a slight increase with the increasing heat flux.

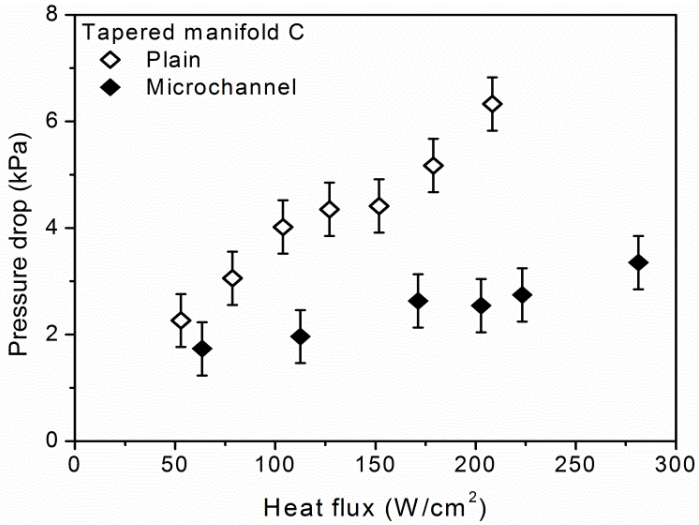

Figure 34: Pressure drop performance for plain and microchannel chips with tapered manifold C

4.2.3 Heat transfer and pressure drop performance with the plain chip

The effect of both types of manifolds on plain chip performance is discussed in this section. Figure 35 shows the boiling performance of tapered and uniform manifolds. The tapered manifold showed an improved performance compared to the uniform manifold. The uniform manifold showed a boiling overshoot and recorded a heat flux of 227.1 W/cm^2 at 22.1 °C wall superheat. The three tapered manifolds showed similar performances to one another. Hence, the effect of taper height itself was not significant in this case. Boiling overshoot was not observed with any of the tapered manifolds. The tapered manifold B recorded a heat flux of 255.1 W/cm^2 at a wall superheat of 17.7 °C.

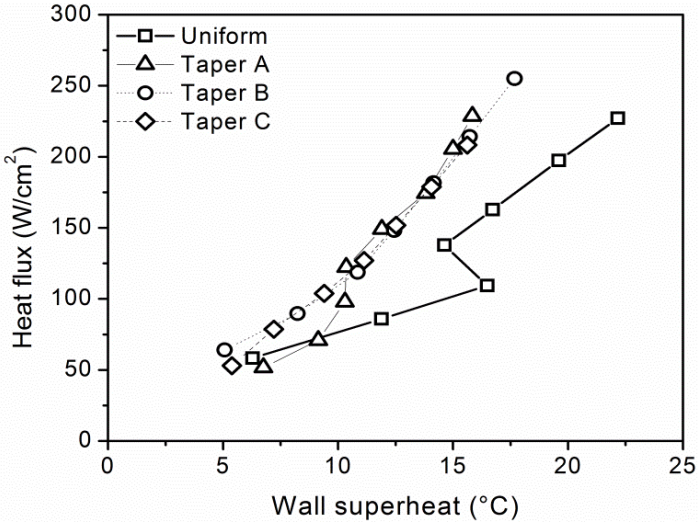

Figure 35: Boiling performance of plain chip with tapered and uniform manifold

The pressure drop performance of the plain chip with the uniform manifold and the three different tapered manifolds is shown in Fig. 36. The tapered manifolds show a significant pressure drop reduction compared to the uniform manifold. The uniform manifold showed the highest pressure drop values at both low and high heat fluxes. For the tapered manifold, the values were below 20 kPa over the entire range. The highest pressure drop was observed with the tapered manifold B at a heat flux of 255.1 W/cm^2 of 19.6 kPa. Tapered manifold C showed the lowest pressure drop over the entire heat flux range. A maximum pressure drop of 6.3 kPa at 208.3 W/cm^2 heat flux was recorded for the tapered manifold C. The introduction of a tapered manifold was thus seen to drastically reduce the pressure drop from 158.4 kPa (uniform) to 6.3 kPa (tapered manifold C) for similar heat flux values.

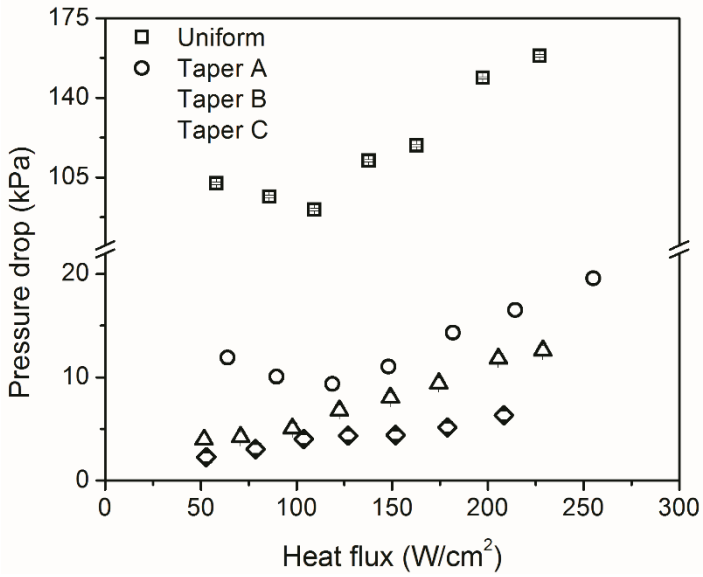

Figure 36: Pressure drop performance of plain chip with uniform and tapered manifolds

4.2.4 Heat transfer and pressure drop performance with the microchannel chip

Results of the microchannel chip with the uniform and the tapered manifolds are discussed in this section. Figure 37 shows the heat flux versus wall superheat plots for the two types of manifolds with the microchannels. Unlike the plain chip performance, the effect of varying the taper was observed to affect the heat transfer performance. The tapered manifold C recorded a heat flux of 281.2 W/cm^2 at a wall superheat of 10.1 °C. The uniform manifold however, showed a better performance than the tapered manifold A, although the testing was not continued to higher heat fluxes. CHF was not reached for any of the tests, hence showing potential for greater heat dissipation. The tapered manifold B dissipated a heat flux 239.1 W/cm^2 at a wall superheat of 8.6 °C. The slope of the tapered manifold A curve suggests that at higher heat fluxes, it might perform better than the uniform manifold.

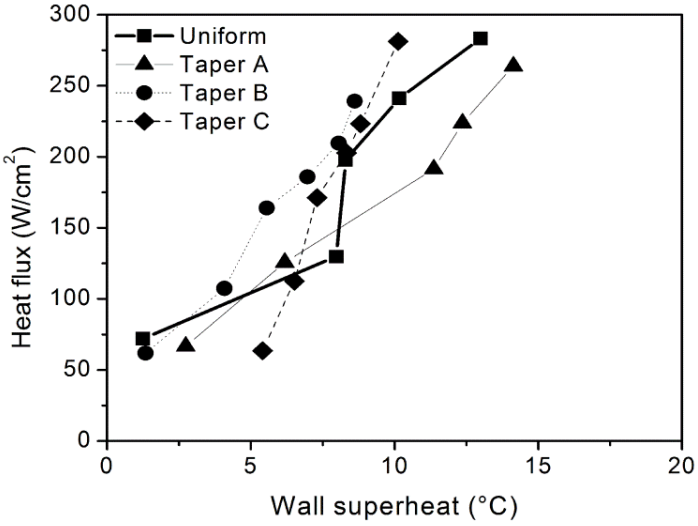

Figure 37: Boiling performance of the microchannel chip with uniform and tapered manifolds

Three tapered manifolds were tested with the microchannel chip and their pressure drop performance is shown in Fig. 38. The maximum pressure drop observed was 11 kPa for tapered manifold A at a heat flux of approximately 170 W/cm^2. A maximum pressure fluctuation of around 7 kPa was observed for all three tapered manifolds. The tapered manifold C showed the lowest pressure drop of 3.3 kPa at a heat flux of 281.2 W/cm^2 in comparison with the other two tapered manifolds. A maximum pressure drop of 10 kPa was observed with the tapered manifold B, and it showed lower pressure fluctuations compared to the tapered manifold A.

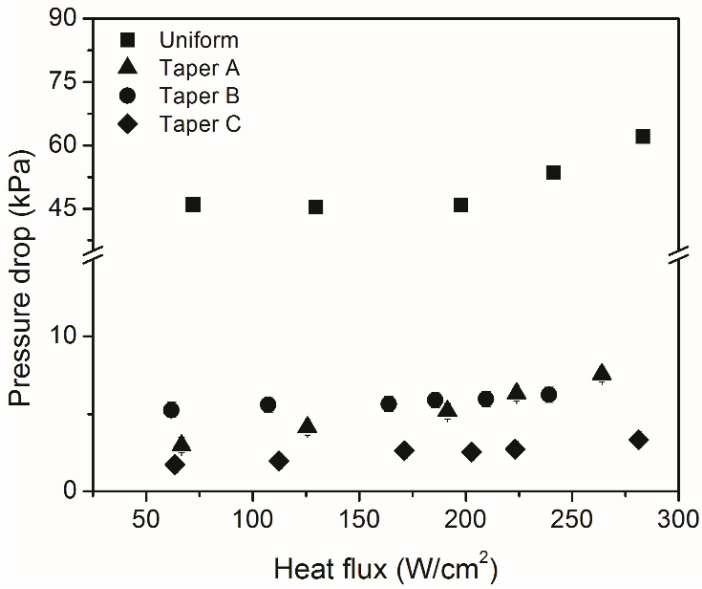

Figure 38: Pressure drop performance of microchannel chip with uniform and tapered manifolds.

4.2.5 Comparison between the microchannel and the plain chip with uniform and tapered manifold

Figure 39 shows the heat transfer performance for tapered manifold C with the microchannel chip and the uniform manifold with both chips. Expectedly, the microchannel chip showed significant performance improvement compared to the plain chip for both manifolds. The introduction of the tapered manifold yields similar performance at the mid-range heat fluxes (between the microchannel chip with different manifolds), but the heat flux is seen to rise for a given wall superheat at higher heat fluxes. The maximum heat flux obtained with the tapered manifold was greater than uniform manifold with the microchannel chip. Both plain and microchannel chips showed a small temperature overshoot with the uniform manifold. No temperature overshoot was observed with the tapered manifold.

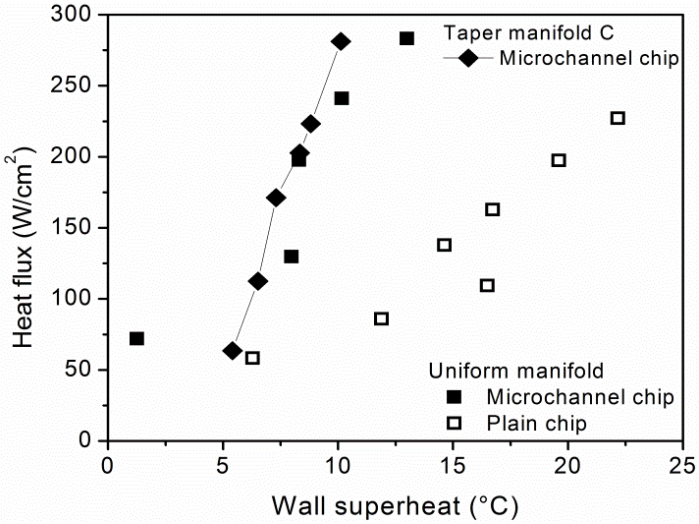

Figure 39: Boiling performance comparison for tapered manifold with microchannel chip and uniform manifold with both plain and microchannel chips.

Figure 40 shows pressure drop versus the corresponding heat flux with the uniform manifold and the tapered manifold C. The highest pressure drop was observed with the uniform manifold with the plain chip. At high heat fluxes (~225 W/cm^2), a pressure drop of 158.4 kPa was recorded with the plain chip. At a similar heat flux, the microchannel chip with a uniform manifold recorded a pressure drop of 50 kPa. The reduction in the pressure drop was mainly due to the increase in the flow cross-sectional area provided by the microchannels. The tapered manifold C showed the lowest pressure drop of ~2 kPa at a heat flux of 225 W/cm^2. The combination of tapered manifold with the microchannel chip clearly showed a significant pressure drop reduction over the entire range of heat flux. The expanding cross-sectional area along the flow direction was able to accommodate the increased vapor flow and resulted in an extremely low pressure drop. The overall increase in the pressure fluctuation with increasing heat flux is also limited for the tapered manifold, hence showing a more stable flow with the tapered manifold in comparison to the uniform

manifold, while simultaneously offering better heat transfer performance in terms of higher heat flux at a given wall superheat.

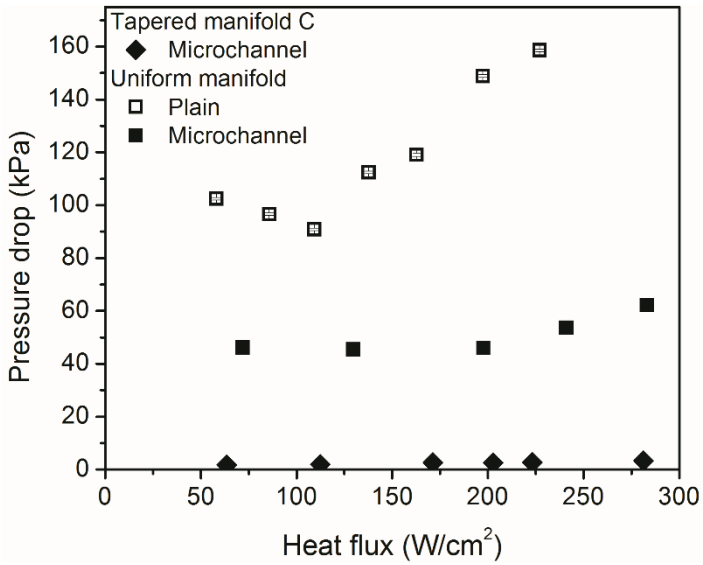

Figure 40: Pressure drop performance comparison with tapered manifold C with microchannel chip and uniform manifold with both chips.

Table 4 shows the maximum values for heat flux, wall superheat, heat transfer coefficient and corresponding pressure drop for plain and microchannel chips. Taper C with the microchannel chip showed the best performance in terms of pressure drop and heat transfer. For the plain chip, similar heat transfer performance was obtained for all three tapers. The tapered manifolds showed significant pressure drop reductions compared to the uniform manifold with the plain chip.

Table 4: Summary of all test runs for plain and microchannel chips including maximum heat flux, wall superheat, heat transfer coefficient and pressure drop.

Chip	Manifold	q''_{max}	ΔT_{sat}	h	ΔP
		W/cm^2	°C	$kW/m^2°C$	kPa
Plain	Uniform	227.1	22.1	102.4	158.4
	Taper A	228.6	15.8	144.4	12.6
	Taper B	255.1	17.7	144.3	19.6
	Taper C	208.3	15.6	133.5	6.3
µchannel	Uniform	283.2	12.9	217.9	62.1
	Taper A	263.8	14.1	186.7	7.5
	Taper B	239.1	8.6	277.6	6.2
	Taper C	281.2	10.1	277.8	3.3

The tapered manifolds with microchannel chips yielded a dramatic enhancement in heat transfer performance, while providing an extremely low pressure drop. This feature makes them particularly suited to cooling the high performance IC chips. The low pressure drop feature provides a very high coefficient of performance (ratio of heat removed to pumping power) that is particularly attractive for the 3D IC chip cooling architecture. For the tapered manifold C with the microchannel chip, a heat flux of 281.2 W/cm^2 is dissipated

at a wall superheat of 10.1 °C with a heat transfer coefficient of 277.8 kW/m^2°C. The corresponding pressure drop was only 3.3 kPa. Further performance enhancements are expected with optimizing the microchannel geometry and the taper configuration.

The main mechanism responsible for reducing the pressure drop with the tapered manifolds is the gradual increase in the flow cross-sectional area as the vapor is generated along the flow direction. As seen from Table 4, the cross-sectional area increases for tapered manifolds, and the pressure drop is correspondingly lower. The results for plain chips are affected due to the presence of backflow under relatively low heat flux conditions. The liquid flows through the microchannels promoting nucleation and is responsible for delaying the CHF. Further work on establishing the CHF limits for these configurations is suggested by redesigning the heater unit to deliver higher heat fluxes.

4.2.6 Conclusion – Taper manifold study

Four manifold (three taper and one uniform) blocks with plain and microchannel surface were experimentally investigated to evaluate the heat transfer and pressure drop performance. Three tapered manifolds with a gradual increase in the height toward the exit with an inlet height of 127 μm and the exit heights of 327 μm, 527 μm and 727 μm and a uniform manifold of a 127 μm height were tested with the microchannel and the plain chips in the current setup. The following conclusions are made from the study:

1. Uniform manifold: A heat flux of 227.1 W/cm^2 at a wall superheat of 22.1 °C was recorded with a plain chip, while a heat flux of 283.2 W/cm^2 at 12.9 °C wall superheat was recorded for the microchannel chip.
2. The combination of the microchannel chip and the tapered manifold significantly reduced the pressure drop in the system. Taper C (with inlet and exit manifold heights of 127 and 727 μm above the top surface of the chip) with a microchannel chip (450 μm depth, 181 μm wide channels and 195 μm wide fins) showed the best performance with the lowest pressure drop of 3.3 kPa compared to the 158.4 kPa pressure drop with the plain chip and the uniform manifold.
3. Taper manifold: A heat flux of 281.2 W/cm^2 at 10.1 °C wall superheat with taper C was recorded with the microchannel chip. The microchannel chip with the tapered manifolds showed significant performance improvement compared to the plain chip with the uniform manifold.
4. Similar improved performance in heat transfer coefficient for the microchannel chip with tapered manifold was observed in comparison to the plain chip with

tapered manifold. A maximum heat transfer coefficient of 277.8 kW/m^2°C was recorded with microchannel chip and taper C.

5. The main mechanism for the dramatic reduction in pressure drop is due to the increased flow cross-sectional area to accommodate the vapor generated along the flow direction. This combines the inherent benefits of microchannels in providing a superior heat transfer performance, with the flow stability and low pressure drop due to the tapered manifold.

Chapter 5: Flow Visualization

In this section, flow patterns and heat transfer mechanisms of an open microchannel and plain surface with tapered manifold are investigated. Various flow patterns are observed and their transitions with increasing heat flux are described. The underlying mechanisms of bubble nucleation, growth and departure are explored through high speed visualization. Furthermore, closed microchannel and open microchannel geometries are compared via bubble dynamics through high speed image sequences. Plain surface bubble ebullition cycle and flow conditions leading to CHF in the OMM geometry are also discussed.

High speed flow visualizations have been conducted by various researchers under different parameters to study various flow patterns in their systems. For example, Hetsroni et al. [64] observed two types of flow patterns, namely annular and dryout, in their study. Kandlikar [27] studied the heat transfer mechanisms in microchannels, focusing on flow instability and two-phase flow patterns (slug flow, annular flow, churn flow and dryout condition). Zhang et al. [65] observed nucleate boiling and eruption boiling in their single microchannel study. They also found the boiling mechanism to be strongly dependent on the wall surface roughness. Chen and Garimella [66] observed bubbly and slug flow at low heat fluxes. At higher heat fluxes, the authors observed annular and churn flow in the downstream section and flow reversal near the microchannel inlet. Harirchian and Garimella [24] studied the effect of various parameters on flow boiling regimes. The authors reported that the flow regimes for microchannels with 400 μm (width) and greater were similar, while microchannels with width less than 400 μm showed different flow

regimes. Recently, Tamanna and Lee [67] used expanding silicon microgap heat sink to study the bubble mechanism in their geometry through high speed visualization. Excellent reviews discussing the flow patterns for different flow conditions and other aspects of microchannel flow boiling are available in literature [68,69].

For the current setup, high speed visualization was accomplished with a Photron 1024 Fastcam CMOS camera and a 150 mm Nikon lens. Additional light required for imaging was provided using a Dolan-Jenner Fiber-lite MH-100 metal halide Machine Vision illuminator lamp. The polysulfone manifold block was polished to a transparent finish to facilitate visualization. The images were taken at 3,000 – 10,000 frames per second (fps). Experiments were performed at heat fluxes in the range of 50 – 500 W/cm^2. A fixed mass flow rate of 80 mL/min and an inlet subcooling of 10 °C were employed. High speed visualization of the boiling phenomena was captured to understand the flow patterns. Bubble nucleation, growth, departure and CHF conditions are all important in providing an insight into the underlying heat transfer mechanisms.

5.1 Flow Patterns

The flow patterns obtained with the microchannel chip and the tapered manifold are discussed in this section. These patterns were identified through high speed images obtained at 3000 fps. They can be broadly classified into five major flow regimes – bubbly, slug, intermittent slug/bubbly, annular, and inverted annular (post-CHF) flows.

Figure 41(a) shows the first regime, bubbly flow, at a low heat flux (~100 W/cm^2). Bubbles nucleate from various nucleation cavities in the microchannel (base of the channels), grow to the size of the channel width and expand onto the fin tops. Further expansion was observed on the fin tops before the eventual departure in the flow direction.

As the heat flux increases, more nucleation sites get activated and further expansion of bubbles also takes place. Slug flow, as seen in Fig. 41(b) forms the second flow regime. In this regime, the bubble expanded on top of the fin and coalesced with other expanding bubbles in the manifold region. Intermittent slug/bubbly flow (Fig. 41(c)) was observed as the next flow pattern with an increase in heat flux (~200 W/cm^2). A number of nucleation sites were active and large vapor bubbles were observed downstream. Both the liquid and vapor phases were distributed over the active area as seen from the figure. In annular flow, the manifold region was mostly comprised of vapor while the channels were filled with liquid. The nucleating bubbles inside the channels fed onto the existing vapor bubbles on the fin tops (further discussed in the mechanism section). At higher heat fluxes (>300 W/cm^2), the annular regime showed stable flow boiling as seen in (Fig. 41(d)). In this regime, the liquid filled the channels and the manifold region was mainly occupied by the vapor. As the heat flux further increases, the liquid film in the channel decreases in thickness. Inverted annular regime was observed once the system reached CHF. This flow pattern, as the name suggests, was the opposite of annular flow. The channels were occupied by the vapor phase and the manifold region was filled with liquid (Fig. 41(e)). This flow regime causes significant increase in the surface temperature and adversely affects the heat transfer performance. The high temperature associated with CHF could also lead to structural damage to the components.

The flow patterns described in the preceding paragraphs were observed in the tapered manifold and open microchannel geometry at a fixed flow rate. Further descriptions on each of the flow patterns along with the image sequences are provided in the following sections to explain the heat transfer mechanisms.

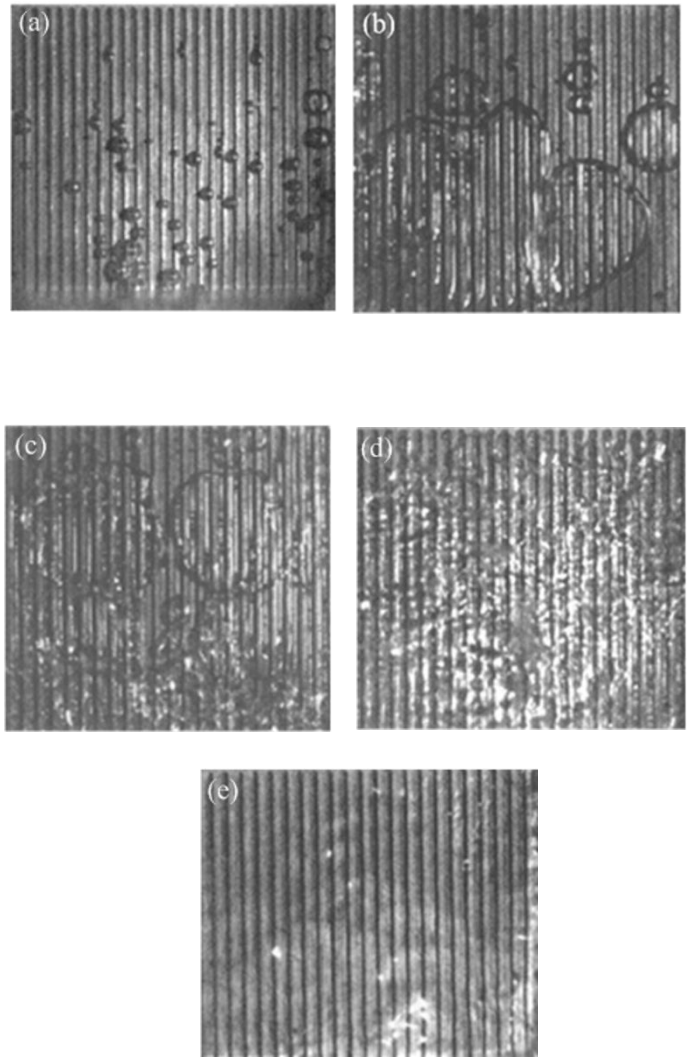

Figure 41 (a-e): Flow regimes for tapered manifold and microchannel geometry (a) Bubbly flow, (b) Slug flow, (c) Intermittent slug/bubbly flow, (d) Annular flow and (e) Inverted annular flow (CHF).

5.2 Flow Pattern Map

Effect of flow rate on flow regimes were further explored through flow pattern maps. The flow patterns for the three mass fluxes tested were plotted with liquid and vapor superficial velocities as co-ordinates as seen in literature. The liquid (j_l) and vapor (j_g) superficial velocities were given by:

$$j_l = \frac{G(1-x)}{\rho_l} \tag{12}$$

$$j_g = \frac{G(x)}{\rho_g} \tag{13}$$

where G is the mass flux, x the exit quality, and ρ_l and ρ_g are the liquid and vapor densities respectively.

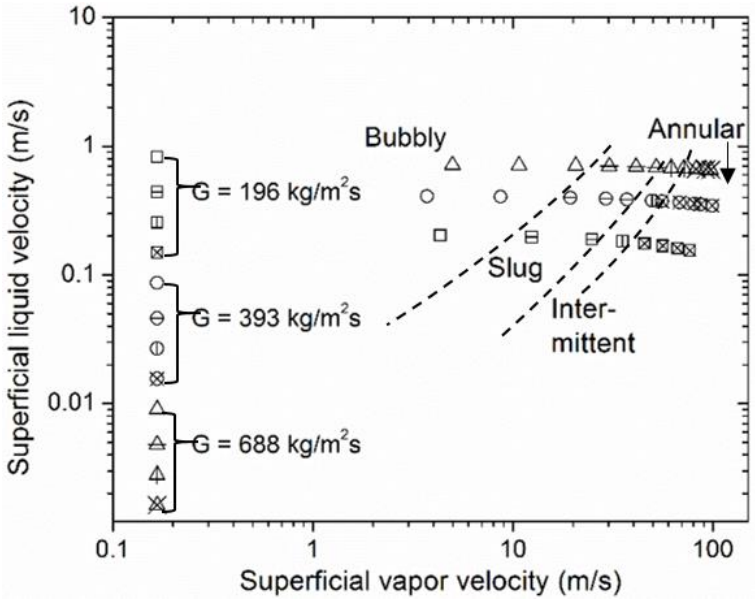

Figure 42: Flow pattern map on superficial vapor and liquid velocity (j_g and j_l) co-ordinates with three mass fluxes of 196, 393 and 688 kg/m^{2}s over a heat flux range from 50-500 W/cm^2

Figure 42 shows the flow pattern map of microchannel with a 4% tapered manifold for three mass fluxes. The bubbly flow regime occurs at low liquid and vapor superficial velocities for all mass fluxes. The transition from bubbly to slug flow for a higher mass flux occurs at a higher j_g, showing the increase in the bubbly flow pattern range. For the lower mass flux, a quick transition was observed form bubbly to slug flow. This is due to the extra space above the microchannel and the gradually increasing cross-sectional area. The low liquid inertia due to the low flow rate allows the bubble to expand in the downstream direction after nucleating. Slug flow and intermittent regime occurred at a higher exit quality for the lower mass fluxes. The transition to annular flow occurs at higher superficial vapor velocity with the increase in the liquid superficial velocity.

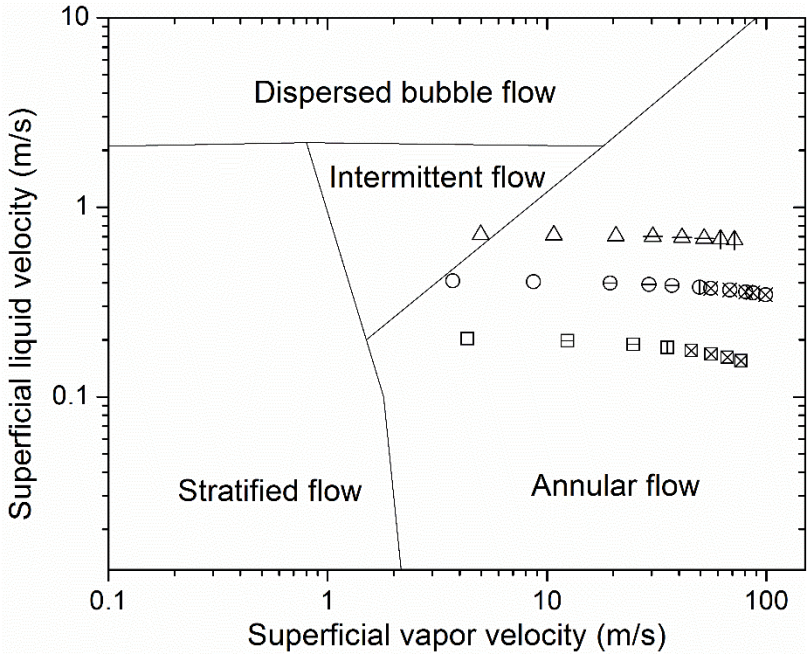

Figure 43: Taitel–Dukler flow pattern map with experimental data points

The Taitel and Dukler [25] map has often been used in literature for better understanding of the flow regimes. The data points obtained in the current study were plotted on these maps as shown in Fig. 43. The flow pattern map showed the majority of the data points in the annular regime, and some in and around the intermittent regime. This is however, not true with the observations from the current experiments. Moreover, no data points were present in the bubbly flow regime in the map. While, during the experimental test runs bubbly flow was observed at low heat fluxes for all three flow rates. Similar results were reported by other researchers using the increased flow cross-sectional area geometries [55].

The Taitel and Dukler flow regime map was developed for adiabatic conditions and showed good prediction in the earlier works for macroscale tubes. The departure from this map with the current data could be due to the complex geometry involving open microchannels and a tapered manifold. Further study is warranted to come up with a comprehensive flow pattern map for tapered geometries. Specifically, the effect of taper and heat flux needs to be explored with a concurrent relation with the heat transfer and pressure drop performance. The present map however indicates significant differences between the tapered manifold configuration and the established microscale and macroscale flow pattern maps.

5.3 Bubble Nucleation Mechanism in Bubbly and Slug Flow

In traditional microchannels, channels are covered with a cover plate (top surface) and under stable boiling conditions bubbles nucleate in the channel and grow downstream in the flow direction. The expansion of the bubbles gives rise to the well-known elongated flow pattern. However, at higher heat fluxes a nucleating bubble grows in both upstream and downstream directions. This leads to explosive bubble growth and in turn to flow instability. By providing a tapered manifold above the microchannels, bubbles have room to grow away from the microchannels into the manifold and depart from the microchannel region without any resistance. This avoids flow instabilities due to flow reversal.

Detailed images of specific bubble nucleation and growth phenomena were further investigated. Figure 44 shows a nucleating bubble sequence at a relatively low heat flux of 100 W/cm^2. The flow direction was from top to bottom as indicated by the white arrow. The left image for Fig. 44(a) shows bubble nucleation and the right side shows a schematic representation of the image for depicting the mechanism. The bubbles nucleate from the bottom surface of the microchannel. The individual frames of other videos with varying taper showed similar bubble nucleation at the base of the channel. Figure 44(b) shows the expansion of the bubble on the fin top, while a new bubble nucleates from the same site. Figure 44(c) shows further growth of the bubble in the manifold region as nucleation continues in the channel.

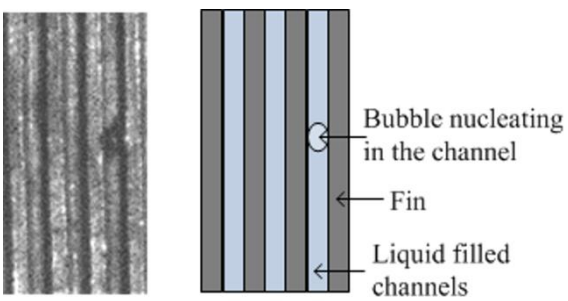

(a) Bubble nucleation on the bottom surface of a microchannel

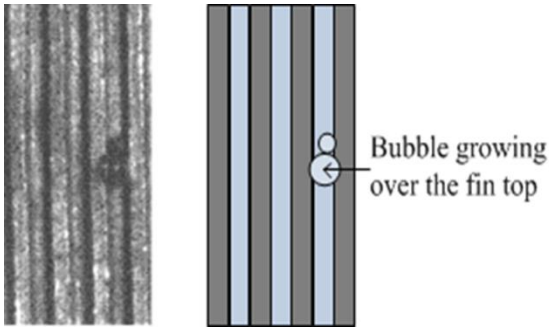

(b) Bubble growth on the top wall (fin top) of the microchannel

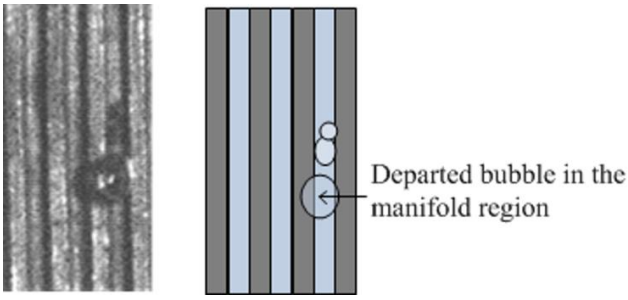

(c) Departed bubble expanding in the manifold region and new bubble nucleation in the channel

Figure 44 (a-c): Successive images of bubble nucleation, growth and departure at low heat fluxes.

Figure 45 shows a sequence of images that provide an insight into the underlying mechanism of bubble nucleation in the OMM geometry. Figure 45(a) shows a bubble nucleating at the base of the microchannel and another large bubble passing over the microchannels in the manifold region. When the bubble in the manifold region overlaps the nucleating bubble, nucleation continues to occur in the other regions of the

microchannel as seen in Fig. 45(b). The individual image shows a number of bubbles present in the channel region while vapor occupies the manifold on top. This indicates that the channels are filled with liquid even when vapor is present in the manifold region. Due to the presence of liquid in the channels, the active nucleation sites continue bubble nucleation, growth and departure. Figures 45 (c) and (d) show a bubble growing and eventually bursting underneath the bubble in the manifold region. Once the bubble covering the nucleation site departs as shown in Fig. 45(e), normal bubble nucleation resumes.

The individual frames from Fig. 45 show that the large vapor remains in the manifold region, while allowing the channel region to maintain liquid flow. This fundamental pattern was seen to exist at higher heat fluxes also.

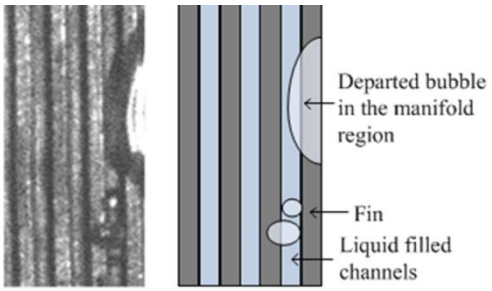

(a) Bubbles nucleating in the channel and a departed bubble in the manifold region.

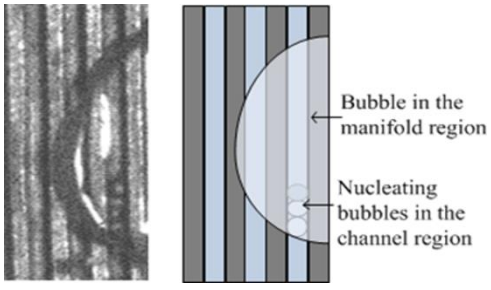

(b) Nucleating bubbles in the channel underneath a bubble in the manifold region

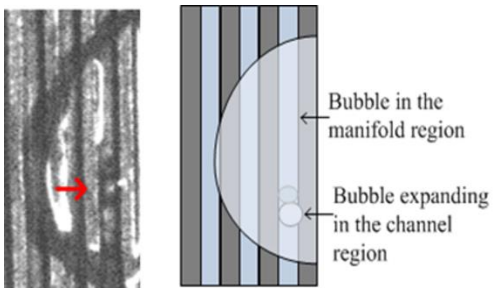

(c) Bubble growing in the channel underneath a bubble in the manifold region

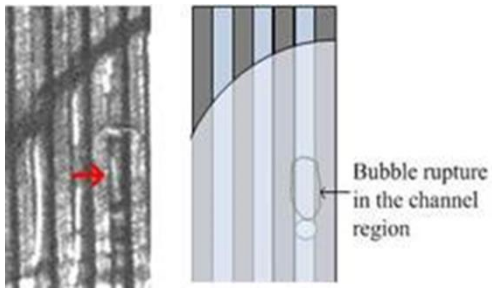

(d) Bubble rupture in the channel underneath a bubble in the manifold region

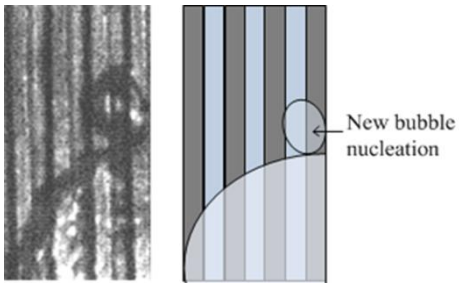

(e) Bubble growing in the channel underneath a bubble in the manifold region

Figure 45 (a-e): Successive images of bubble mechanism in OMM geometry

5.4 Intermittent Slug/Bubbly Flow

Figure 46 shows an intermittent slug and bubbly flow pattern in the OMM geometry. The image shows the entire open microchannel surface at a moderate heat flux of 200 W/cm^2. In the figure, different phenomena illustrated through individual frames from Figs. 44 and 45 are seen. At various locations (center marked in the figure), several departed bubbles are seen in the manifold region.

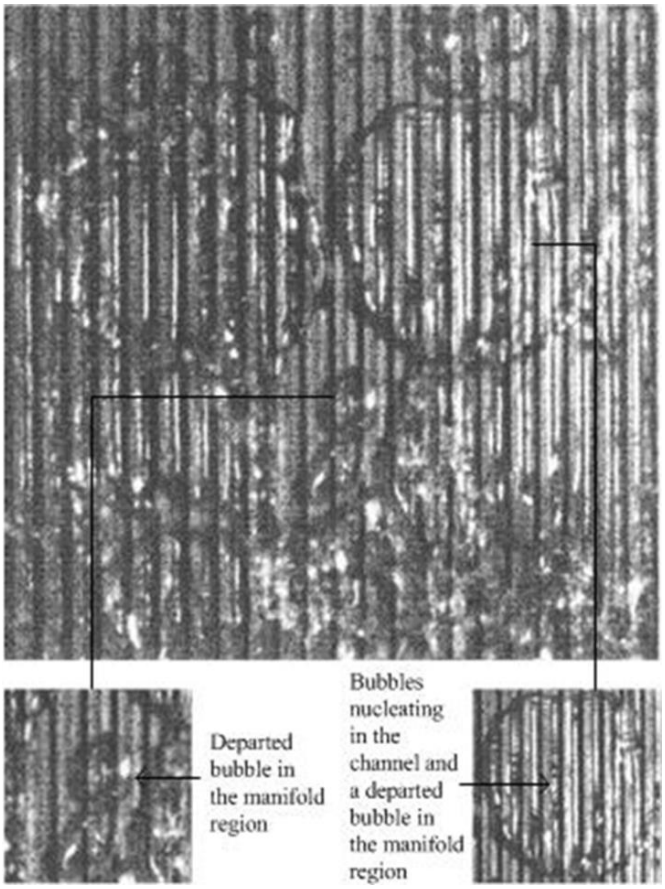

Figure 46: Bubble nucleation, growth and departure mechanism at higher heat flux.

Bubble growth and nucleation are also observed in the channel region as shown in Fig. 46. Similar to Fig. 44, bubble nucleation was observed at the base of the microchannel while vapor was present at the top in the manifold region. Bubble growth is also seen in the channel underneath the vapor indicating that the channels are liquid filled. Hence the same mechanism for bubble nucleation, growth and departure exists at higher heat fluxes for the OMM geometry.

At still higher heat fluxes, the entire manifold area was covered with vapor as seen in Fig. 47(a). The channels were flooded with water; hence in the next frame Fig. 47(b) we see bubble nucleation and growth from underneath the vapor blanket. The extra flow cross-sectional area available in the flow direction due to taper allows bubbles to expand while leaving the channels filled with oncoming liquid. This mechanism helps in extending CHF and overcoming the flow instability.

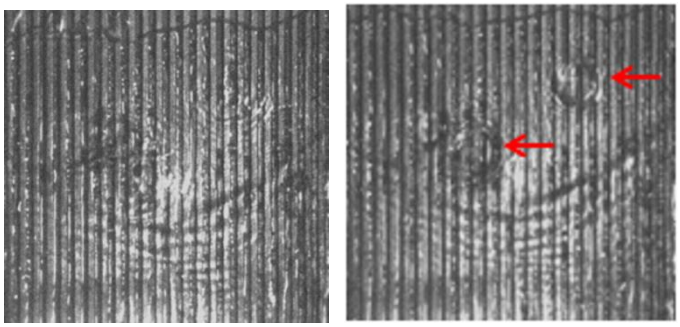

(a) (b)

Figure 47 (a-b): Images showing bubble nucleation and growth in the channels under the vapor occupied manifold region at a higher heat flux.

5.5 Annular Flow

Figure 48(a) shows a high speed image of the annular flow regime. Similar to the intermittent regime (Fig. 46), bubble nucleation occurs in the channel region. However, the majority of nucleation occurs at the section close to the inlet (upstream). The channels are liquid filled with occasional nucleation activity in the downstream region. The regime shows a high rate of bubble nucleation and departure. At heat fluxes of > 300 W/cm^2, this regime shows stable boiling with a similar bubble ebullition cycle as explained through previous figures.

Figure 48(b) shows a transition flow pattern between the annular and the inverted annular flow regime. In the image, bubble nucleation was observed near the inlet side of the microchannel chip in the channel region. In the downstream section, no bubble nucleation was seen from the channels and occasional dry spots were observed.

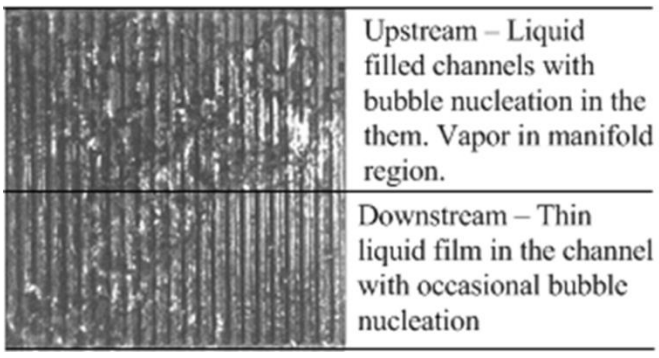

(a) Annular flow regime

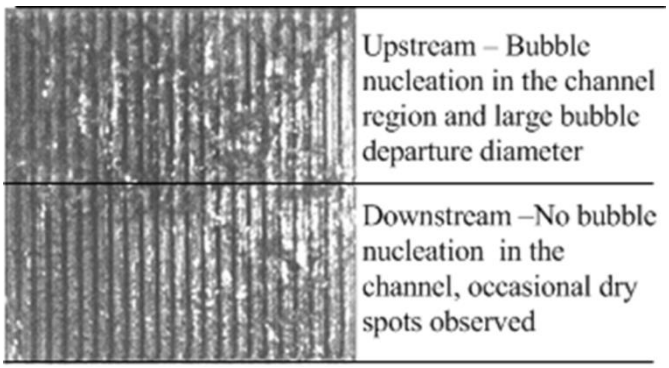

(b) Transition from annular flow to inverted flow regime

Figure 48 (a-b): Individual frames showing the annular flow and the transition flow regime.

5.6 Critical Heat Flux

Critical heat flux limits the thermal performance of a system and occurs when the vapor film covers the entire heated surface. This vapor film does not allow liquid rewetting of the surface which leads to extremely high surface temperatures and could comprise structural integrity of the system as well. The image sequence in Fig. 49 shows transition annular flow, intermittent CHF, rewetting and eventually the inverterd annular flow. Fig 49(a) shows rapid bubble nucleation near the entrance of the microchannel. The bubbles nucleate from the channel and depart downstream in the manifold region. However, no bubble nucleation was seen from the downstream microchannel section, indicating dryout and presence of vapor in the channel. In the next sequence (Fig. 49(b)), due to the rapid nucleation at the microchannel entrance region, the rapid expansion and coalition of the bubbles leads to the onset of intermittent CHF. Fig 49(c) shows an intermittent CHF taking place. The entire microchannel surface was covered with vapor and no nucleation from within the channel region was seen. In the next image shown in Fig. 49(d), the oncoming liquid inertia overcomes the vapor blanket on the channel and bubble nucleation was

observed at the inlet channel section. The downstream section however was still under CHF-like condition. Rewetting and rapid nucleation resumes near the upstream section in the microchannel region (Fig. 49(e)). The image shows some rewetting in the downstream region, however the surface reverts to dryout conditions quickly. The image sequence seen in Fig 49 (a) – (e) is repeated multiple times, charactertized by brief periods of dryout and then rewetting due to initiation of nucleation at the inlet. Eventually, the final image (Fig. 49(f)) shows that CHF was reached with the inverted annular flow pattern.

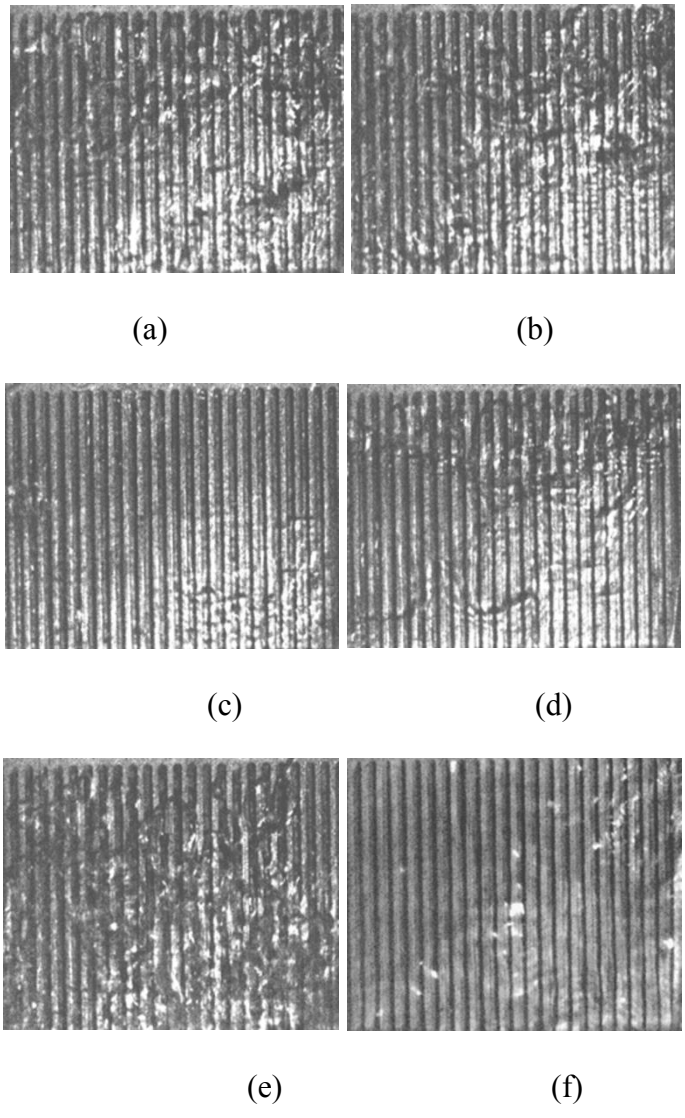

Figure 49 (a-f): Images showing the transition from annular to inverted annular flow

5.7 Heat transfer mechanism for plain surface

5.7.1 Bubble nucleation

Figure 50 shows a sequence of nucleation and growth of a bubble on a plain surface with tapered manifold at low heat fluxes. The flow direction was from top to bottom as indicated by the black arrow. In the first three images (a-c), bubble nucleation and growth were observed. Figure 50(d) shows further expansion and last two images (Figs. 50(e) and (f)) show bubble coalescence. During the bubble growth (from Fig 50(c) onwards), no dry out spots were observed underneath the bubble. This indicated a presence of a thin film on the surface underneath the expanding bubble.

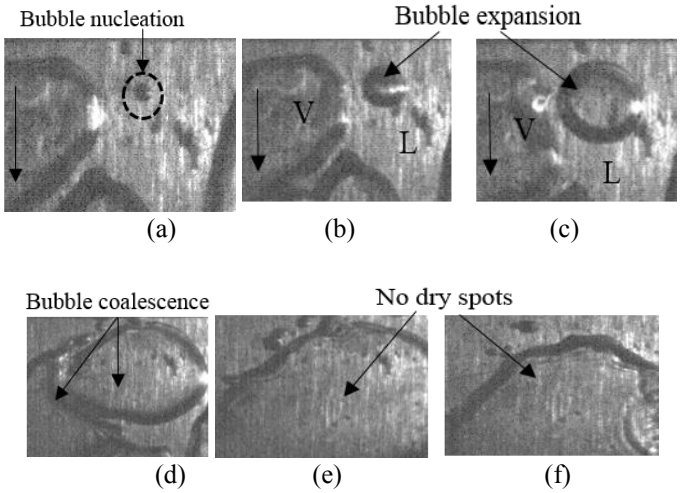

Figure 50 (a-f): Successive images of bubble nucleation and growth at the lower heat fluxes

5.7.2 Dry spot formation

Fig 51(a) shows a bubble nucleating underneath an expanding bubble (as shown by the highlighted region). The nucleation spot forms a dry spot after the collapse of the bubble (Fig. 51(b)). The dry spot increases in size due to the absence of liquid rewetting and more dry areas appear as seen in Fig. 51(c). Dryout was seen to be initiated from the active nucleation sites covered by the oncoming large bubble. It is thus seen that nucleation and dryout are closely interlinked. At higher heat fluxes, these dry regions are expected to grow rapidly and may act as precursors to CHF. In the low heat flux ranges tested, dryout was not seen to be initiated from other regions in the thin liquid film formed under the bubble.

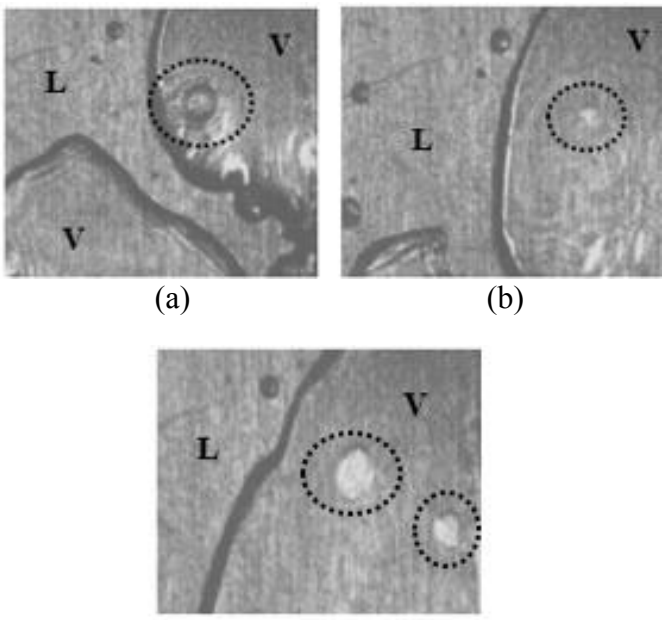

Figure 51 (a – c): Formation of dry spots in the OMM geometry

5.7.3 Bubble growth

As heat flux increases, more nucleation sites become active and lead to further expansion and coalescence of nucleating bubbles. However, increased dry spots were also observed on the surface. Figure 52 shows an image sequence at a higher heat flux of 100 W/cm^2. Figures 52(a) and (b) show bubble growth in all directions when the bubbles are relatively small. Figure 52(c) shows bubble expansion in the flow direction downstream. Formation of dry spots was observed as seen in Fig. 52(d) close to the nucleation site. As the bubble expands further, several dry spots were seen in Fig. 52(e) at various locations. Individual frames of bubble growth (see Figs. 52(b-e)) show that the majority of bubble expansion occurred towards the downstream direction. This was due to the effect of the taper manifold, further discussed in the next section.

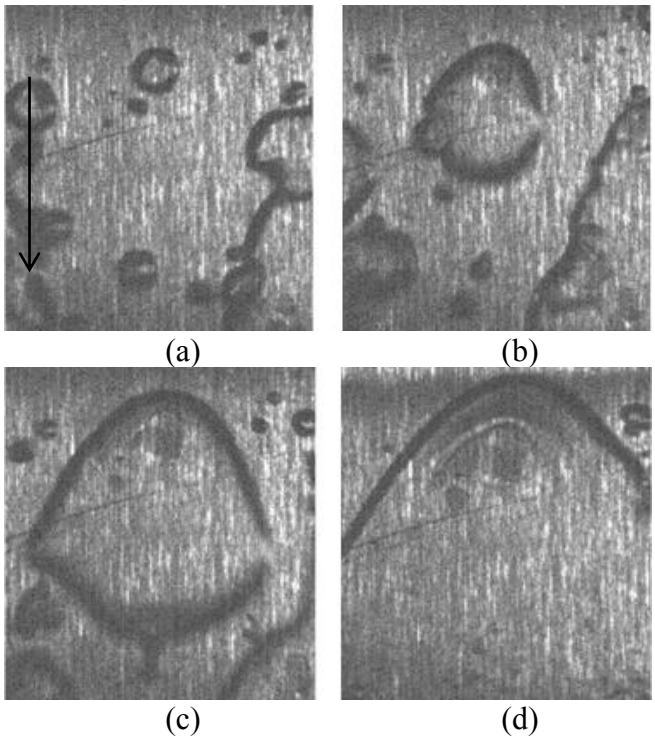

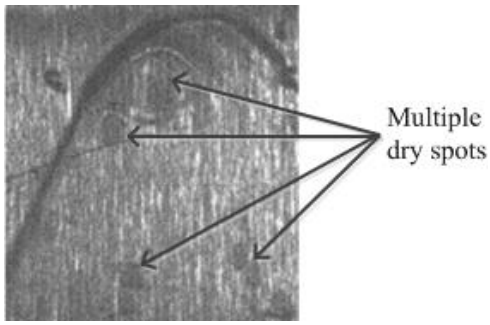

(e)

Figure 52 (a-e): Individual frames showing bubble expansion and multiple dry spots on the surface

Figure 53 shows an individual frame of the entire plain surface at high heat flux. Liquid presence at the center of the surface was observed, while vapor covers on both sides of the liquid. As seen from the image, multiple dry spots were observed in the two vapor sections underneath the liquid film. Bubble nucleation was observed in the liquid section as shown in the figure below.

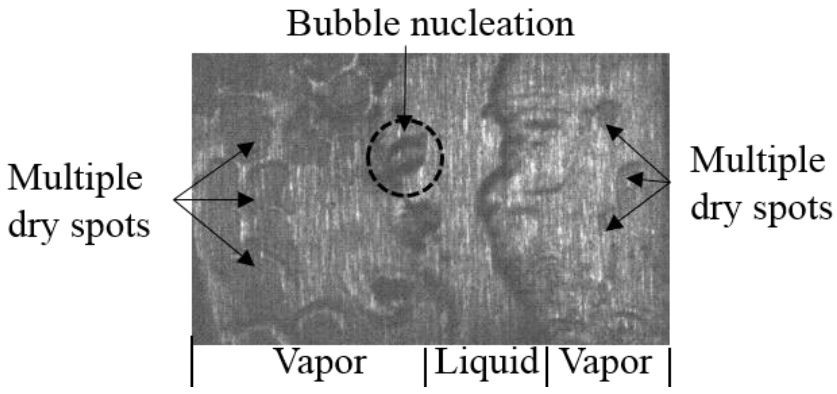

Figure 53: Image of the entire boiling surface showing multiple dry spots at higher heat flux

5.7.4 Critical heat flux

The CHF marks the end of nucleate boiling and limits the thermal performance of the flow system. It occurs when the vapor films cover the heated surface and does not allow rewetting of liquid to occur. This leads to high surface temperature and structural damage to the system. Figure 54 shows the image of CHF for plain surface in the OMM configuration. Figure 54 (a) shows some nucleation activity in the upstream section (inlet) of the plain surface, while the downstream section displays complete dryout. Figure 54 (b) shows CHF with the vapor film covering the entire surface and no nucleation activity was seen. Liquid was observed flowing over the vapor blanket showing the inverted annular flow pattern. The auxiliary high pressure reservoir was activated to cool the surface so as to minimize damage to the manifold block.

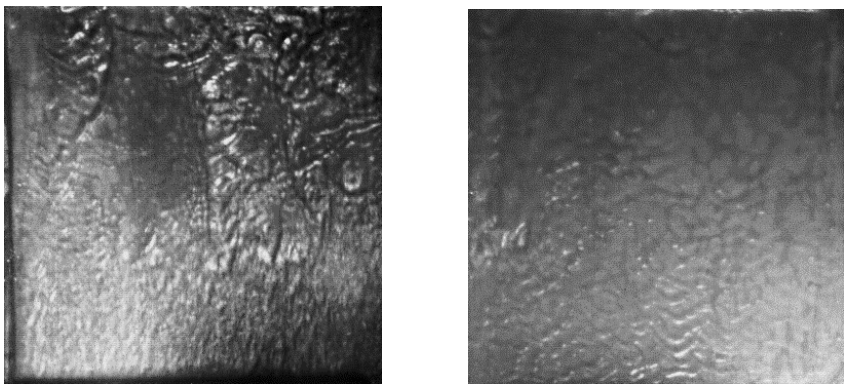

(a) (b)

Figure 54: Images showing pre and post CHF for uniform manifold configuration

5.8 Comparison of Bubble Nucleation Mechanism Between Plain and Microchannel Surface

For the plain surface, dryout is initiated when an oncoming departed bubble covers an active nucleation site as seen from the sequence of images shown in Fig 55. In case of a microchannel surface, nucleation occurs in the channel and the bubble grows and departs in the manifold region, keeping the channel filled with liquid. When a departed bubble arrives over a nucleation site in the microchannel (Fig. 45), the bubble nucleation continues in the channel. The addition of microchannel and taper provides increased cross-sectional area which has a significant impact on the bubble growth. This mechanism prevents dryout formation at low heat fluxes and provides a significant increase in heat transfer performance.

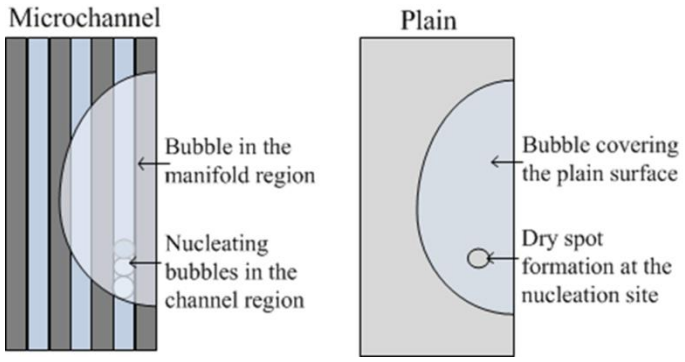

Figure 55: Schematic representation of the difference in the bubble nucleation mechanism for microchannel and plain surface.

5.9 Comparison of Closed Microchannel and OMM Geometry

Closed microchannels (microchannels with a cover plate) have been extensively studied by earlier researchers [38,64]. Balasubramanian and Kandlikar [70] reported flow instability due to explosive growth of bubbles in their flow boiling study as shown in Fig. 56. Rapid bubble growth in the microchannel causes the bubble to grow explosively in both upstream and downstream directions. The explosive bubble growth rate occurs due to the surrounding superheated liquid environment that the bubble experiences after nucleation. This rapid bubble growth leads to flow reversal and flow maldistribution in parallel channels. The walls of the microchannel remain exposed to the rapidly growing bubble, creating local dry patches and causing a reduction in the heat transfer performance. In certain cases, the bubble expands back into the inlet header due to flow reversal and causes severe pressure and temperature fluctuations. More importantly, these can lead to early CHF and damage the structural integrity of the system. Inlet restrictors have been used to overcome flow maldistribution, however the overall heat transfer performance with microchannels was still low.

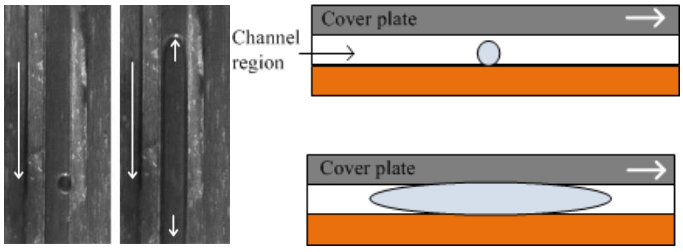

Figure 56: Closed microchannel showing flow instability (Balasubramanian and Kandlikar [70])

The bubble nucleation, growth and departure mechanism for the OMM geometry is seen in Fig. 57. The bubbles nucleating in the channels are termed as the primary bubbles, while the bubbles flowing in the manifold region are called secondary bubbles. As seen from Figs. 44-46, heat transfer performance is increased and flow instabilities are drastically reduced by providing space for secondary bubbles to expand and flow in the manifold region. The localized expansion of a primary bubble in both upstream and downstream directions within the channel region does not have any detrimental effect on the overall stability of the system because of the large interconnected vapor space available in the manifold. The flow remains stable in the downstream direction.

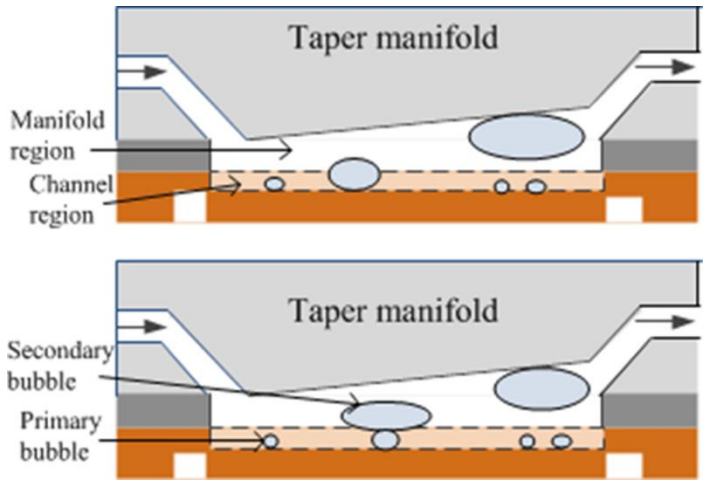

Figure 57: Open microchannel with tapered manifold showing bubble dynamics.

5.10 Conclusions – Flow Visualization

High speed visualization was employed to study the flow patterns and heat transfer mechanisms for open microchannel with tapered manifold geometry. The following conclusions were made through this study:

1. Five flow patterns namely, bubbly flow, slug flow, intermittent slug/bubbly flow, annular flow and inverted annular flow (CHF) were identified with the OMM geometry.
2. For bubble nucleation process in the OMM geometry, the bubbles nucleated from the base of the channel and grew over the channel fin in the manifold region.
3. The departed bubbles occupied the space in the manifold region and expanded in the flow direction due to the taper.
4. The channels remain filled with liquid while the large bubbles flow in the manifold over the microchannels. Bubble nucleation continues to occur in the channel even when the vapor occupies the manifold area over it and similar mechanistic pattern is observed at higher heat fluxes.
5. Taper helps in the overall stability and is not affected by the perturbation due to the nucleation and localized explosive growth of bubbles in the microchannel.
6. Localized lateral expansion of the bubbles in the channels did not have any adverse effect on the heat transfer performance due to the large available vapor space (manifold region) above the microchannels.
7. For the plain surface, dry spots were observed at active nucleation sites covered by an oncoming vapor bubble. This dry spot region grew until rewetted by the liquid stream.

Similarity between pool boiling and flow boiling in microchannels reported in [35] is also seen to be applicable to flow boiling in tapered OMM configuration.

8. Nucleation and bubble growth (primary bubble) in the microchannels and merger with the vapor in the manifold region (secondary bubble) are seen as the main mechanism responsible for enhanced heat transfer performance.

Chapter 6: Pressure Drop Modeling

Accurate prediction of pressure drop is critical in designing multiphase systems, since it is closely related to the pumping power of the device. However, the accuracy of prediction is generally not good in multiphase systems and the average error of 30% is typical even with the advanced models. In general, pressure drop modeling can be broadly classified into two approaches [69]: homogeneous flow model and separated flow model.

The homogeneous model [71] is based on the assumption of equal liquid and vapor phase velocities. The model treats the two-phase flow as a pseudo single-phase flow with suitably phase-averaged viscosity and density equations. It is one of the most widely used model that provides reasonable prediction of pressure drop over a wide range of parameters. The model has been used successfully for various fluids [72–75] including refrigerants, carbon dioxide, nitrogen gas and polyethylene glycol ether. It has shown a good predictive ability for both adiabatic and diabatic conditions, especially in the bubbly, churn and wispy annular regimes, where uniform phase velocities are a reasonable approximation.

For separated flow model the velocity of each phase is calculated separately. A two-phase multiplier is used depending on the flow conditions to scale the single-phase pressure drop. The two-phase multiplier is based on the form proposed by Lockhart and Martinelli. The model uses empirical correlations to relate the two-phase multiplier and void fractions to the independent variables of the flow. This requires curve fitting based on experimental data. The model has been widely used for annular flow pattern.

Bowers and Mudawar [76,77] used the homogeneous model for their microchannel and minichannel heat sink geometries. The model predicted well for their R-113 experimental data within ±30% error band. In a later publication, the authors added the effects of flashing and compressibility to the homogeneous model. Field and Hrnjak [72] used four different refrigerants in their adiabatic pressure drop study for a rectangular channel with a hydraulic diameter of 148 μm. They compared their experimental data with the homogeneous model and separated flow model. The authors developed a new Chisholm parameter C used in the separated flow model. Saisorn and Wongwises [78] investigated the applicability of various viscosity correlations in their air-water experiments. McAdams et al. and Beattie and Whalley showed good agreement between their models and their own experimental data. Lee and Mudawar [79] investigated the pressure drop model for their microchannel heat sink arrangement at various mass flux and heat flux conditions with R134a and noted that the homogeneous model underpredicted their data. They developed a new correlation using the separated flow model which gave a mean deviation of less than 10%.

Choi and Kim [80] used water and nitrogen gas in a single microchannel for their adiabatic two-phase pressure drop study. They investigated the homogeneous model with seven different viscosity averaging schemes and the separated flow model with ten different correlations. For the homogeneous model, Beattie and Whalley's viscosity equation showed the best prediction with a minimum deviation of ±50%. The authors also proposed a new correlation. The homogeneous model has also been used in the application of condensation in a vertical tube. Dalkilic et al. [81] used ten different viscosity correlations in their study and found that Owens, Lin et al. and McAdams et al models showed the least deviation with experimental data within ±30%.

In this section, the homogeneous model with seven viscosity averaging schemes is used to predict the frictional pressure drop data for the OMM geometry. The acceleration and area change terms are obtained from the equations presented by Collier [71]. Separated model can be undertaken once a large data bank is available for empirical correlation. Experimental data with water from uniform and tapered manifold configurations with two copper chips (plain and microchannel) were obtained and compared with the homogeneous model predictions. A comparison among various taper gradients is also discussed with different viscosity models. Various components (friction, acceleration and area change) of the homogeneous model are discussed individually through pressure drop and heat flux plots. Lastly, images from a high speed camera are shown for plain and microchannel chips for gaining an insight into phase distributions across the microchannels and suitability of the homogeneous model.

6.1 Pressure Drop Analysis

The differential pressure sensors were located at the inlet-outlet manifolds. The pressure drop calculations consisted of the summation of the single phase region (due to the inlet subcooling) and the two phase region. Single phase pressure drop in the inlet and in the channel region are discussed first and then the two-phase pressure drop modeling is presented.

Single phase pressure drop components (as seen in Fig. 58) are subdivided into inlet region and channel region. The inlet region consists of pressure drop components due to pipe and duct before the channel region. The channel region consists of contraction losses and pressure drop over the single phase channel length region.

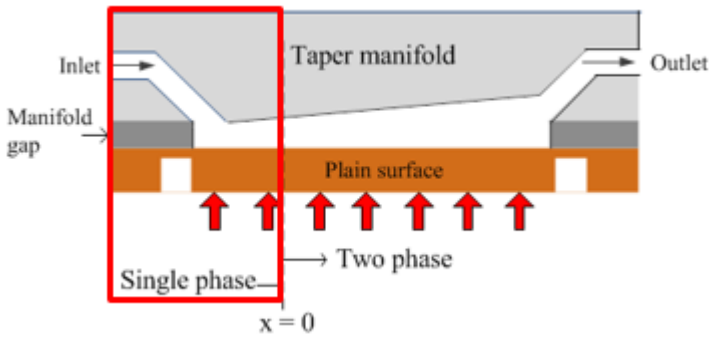

Figure 58: Schematic of the tapered manifold highlighting the single phase pressure drop region

6.1.1 Single phase inlet region (minor losses)

The inlet region consisted of the frictional pressure drop from the pipe and the duct region (see Fig. 58) and was calculated using the below equations:

$$\Delta P_{inlet} = \frac{2f\rho u_m^2 L}{D} \tag{14}$$

$$u_m = \frac{\dot{m}}{\rho A_c} \tag{15}$$

$$Po = fRe \tag{16}$$

where f is the fanning friction factor, u_m is the mean velocity and Po is the Poiseuille number. The Poiseuille number depends on the flow-channel geometry and is given by the equation below [82].

$$Po = 24(1 - 3553\alpha_c + 1.9467\alpha_c^2 - 1.7012\alpha_c^3 + 0.9564\alpha_c^4 - 0.2537\alpha_c^5 \tag{17}$$

where α_c is the aspect ratio and the Poiseuille number for the circular inlet section is taken as 16 [83]. For the rectangular duct leading to the manifold duct, the Poiseuille number was calculated through the Eq. (17).

6.1.2 Single phase channel region

The channel region for single phase consisted of the frictional pressure drop component and the entrances losses. These were calculated through the equation shown below:

$$\Delta P_{sp} = \frac{\rho u_m^2}{2}\left(K_{ent} + \frac{4 f_{app} L_{sp}}{D_h}\right) \tag{18}$$

where K_{ent} is entrance loss due to the area change at the inlet, f_{app} is the apparent fanning friction factor which takes into account the pressure drop due to friction and the developing region effects, L_{sp} is the single phase length in the channel and D_h is the hydraulic diameter. The entrance loss value was obtained through the graphs from Kays and London [84]. The single phase distance (L_{sp}) at which the water becomes saturated (thermodynamic quality x=0) was calculated from the following equation:

$$L_{sp} = \frac{\dot{m} C_p \Delta T_{sub}}{q"W} \tag{19}$$

where W is the chip width (10 mm), ΔT_{sub} is the degree of subcooling, and q" is the total heat transferred. The apparent fanning friction is calculated through the Poiseuille number by calculating a non-dimensional length x^+ given by:

$$x^+ = \frac{L_{sp}/D_h}{Re} \tag{20}$$

The above value with the aspect ratio value is used to obtain the $f_{app}Re$ through a look up table derived by Phillips following the procedure outlined in [93].

6.1.3 Two-phase region

The two-phase pressure drop region (as seen in Fig. 59) consists of pressure drop in the channel region, expansion losses and exit losses in the pipe and duct.

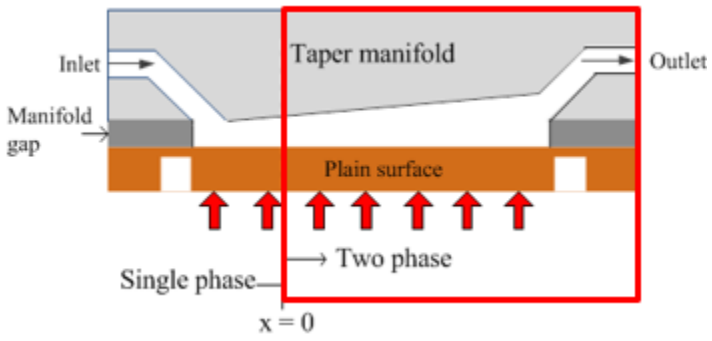

Figure 59: Schematic of the tapered manifold highlighting the single phase pressure drop region

The two phase region length L_{tp}, is given by:

$$L_{tp} = L - L_{sp} \tag{21}$$

The two-phase friction factor is calculated using:

$$f_{tp} = 0.079 \left(\frac{GD_h}{\mu_{tp}}\right)^{-0.25} \tag{22}$$

where L is the total channel length (10 mm) and L_{sp} is the single phase region length.

The two-phase pressure drop consists of frictional, accelerational, and gravitational components. The gravitational term was zero since the test section was kept horizontal. The homogeneous model was used for the two-phase pressure drop calculations. For the uniform manifold, the homogeneous model consisted of the friction, acceleration and gravity components. The frictional pressure drop term was calculated using seven different viscosity averaging schemes, while the acceleration term was calculated using the equations from Collier [71]. The gravity term was zero for the horizontal test section. The integrated form with the frictional and accelerational terms is given as follows:

$$\int_0^{L_{tp}} -\left(\frac{dP}{dz}\right) dz = \frac{\frac{2f_{TP}G^2v_f}{D_h}\left[1 + x\left(\frac{v_{fg}}{v_f}\right)\right] + G^2 v_{fg}\frac{dx}{dz}}{1 + G^2 x\left(\frac{dv_g}{dp}\right)} \tag{23}$$

where x is the exit quality, v_f is the specific volume of the liquid, v_{fg} is the difference in the specific volume of saturated liquid and vapor, G is the mass flux and f_{TP} is the two phase friction factor.

For the tapered manifold, to account for the increase in the cross-sectional area due to taper, an additional area term was added to the frictional and the accelerational terms. A similar equation to that of the uniform manifold was used with the addition of the following area change term to Eq. (23):

$$-\left(\frac{dP}{dz}_{taper,area}\right) = \frac{\frac{-2G^2 v_f}{A_c}\left[1 + x\left(\frac{v_{fg}}{v_f}\right)\right]\frac{dA}{dz}}{1 + G^2 x\left(\frac{dv_g}{dp}\right)} \quad (24)$$

where A_c is the cross-sectional area and dA/dz is the change in cross-sectional area along the channel length (two phase region). Since the quality change was quite small over the test section, an average quality and the average mass flux at the center of the two-phase flow length were used.

The two-phase friction factor in Eq. (23) was calculated using different two-phase viscosity averaging schemes. Various researchers have employed different models for the two-phase viscosity [86–91]; the well-established models reported in literature are shown in Table 2.

Table 5: Various two-phase viscosity averaging schemes used in the homogenous model

1	Owens	$\mu_{tp} = \mu_f$
2	Cicchitti et al.	$\mu_{tp} = x\mu_g + (1-x)\,\mu_f$
3	Lin et al.	$\mu_{tp} = \frac{\mu_f \mu_g}{\mu_g + x^{1.4}(\mu_f - \mu_g)}$
4	McAdams et al.	$\frac{1}{\mu_{tp}} = \frac{x}{\mu_g} + \frac{1-x}{\mu_f}$
5	Akers et al.	$\mu_{tp} = \frac{\mu_f}{\left[(1-x) + x\sqrt{\frac{v_g}{v_f}}\right]}$

6	Beattie and Whalley	$\mu_{tp} = \omega\mu_g + (1-\omega)(1 + 2.5\omega)\,\mu_f$ $\omega = \frac{xv_g}{v_f + xv_{fg}}$
7	Dukler et al.	$\mu_{tp} = \frac{xv_g\mu_g + (1-x)v_f\mu_f}{xv_g + (1-x)v_f}$

The exit quality was calculated taking into account the inlet subcooling as given by:

$$x = \frac{1}{h_{fg}}\left[\left(\frac{q''A}{\dot{m}}\right) - C_p\Delta T_{Sub}\right] \tag{25}$$

where h_{fg} is the latent heat of vaporization, A is the projected area, C_p is the specific heat capacity, and ΔT_{Sub} is the degree of subcooling.

6.1.4 Two-phase exit region (minor losses)

Similar to the inlet single phase losses Eq. (14), the exit losses were calculated at the exit, and the frictional pressure drop in the rest of the non-heated region was calculated using the two-phase friction factor (f_{TP}).

$$\Delta P_{sp\_exit} = \frac{\rho u_m^2}{2}\left(K_{exit} + \frac{4f_{TP}L}{D_h}\right) \tag{26}$$

$$\Delta P_{exit} = \frac{2 f_{TP} \rho u_m^2 L}{D} \quad (27)$$

where K_{exit} is the exit loss due to the area change at the exit and similar to the entrance losses, the exit loss value was obtained through the graphs from Kays and London [84].

6.1.5 List of key assumptions

1. Homogeneous fluid behavior: Equal liquid and vapor velocities. The two-phase flow behaves like a single phase.
2. Mass flux calculation: Average mass flux calculation is taken for the two-phase channel region.
3. Average exit quality is considered for the two-phase channel calculations. Exit quality is taken for the pipe outlet calculations
4. Similar to mass flux, average hydraulic diameter is taken for the two-phase channel region.
5. Pressure exit/outlet is taken as atmospheric pressure for fluid property relating to pipe outlet calculation.
6. Fluid properties for calculations which include liquid and vapor viscosities, and liquid and vapor specific volume for the microchannel regions are calculated by assuming average inlet pressure value. The inlet pressure value is referenced from the experimental pressure drop value, where the exit pressure is 1 atm.
7. Blasisus equation for two-phase friction factor was used for calculation of $F_{tp.}$

8. For two-phase viscosity calculation, six different models from literature were used and compared.
9. Heat flux values was calculated based on projected area (100 mm2) and uniform heat flux condition was taken.
10. For single phase pressure drop calculation, all fluid properties were taken for temperature ~90°C.

6.2 Results

The channel pressure drop was obtained from the experimental pressure drop value after subtracting minor losses and pressure drop in the single phase inlet region and two-phase exit region. The maximum heat flux tested was limited to 300 W/cm^2 due to the heater capacity. None of the tests reached CHF. Pressure drop predictions from the homogeneous model are compared with the experimental data for all four test section configurations described in Table 1. Seven viscosity averaging schemes shown in Table 2 were investigated. For the uniform manifold, all seven viscosity models are compared with the experimental data.

Results for uniform manifold configurations with plain and microchannel chips are presented. For all the plots, pressure drop results are plotted as a function of heat flux. Mean absolute error (MAE) was calculated using the following equation:

$$MAE\% = \frac{1}{N}\sum\left|\frac{\Delta P_{exp} - \Delta P_{model}}{\Delta P_{exp}}\right| \times 100 \tag{28}$$

All comparison plots include data points >100 W/cm^2. This was done to avoid the effect of subcooled flow boiling. Pressure drop modeling of subcooled effects is not undertaken in this work. Four different combinations were tested:

- Plain chip with uniform manifold
- Microchannel chip with uniform manifold
- Plain chip with tapered manifold

- Microchannel chip with tapered manifold

The results of comparison of experimental pressure drop data with different models for these four configurations are described in the following sections.

6.2.1 Plain chip with uniform manifolds

Figure 3 shows a comparison of the experimental results for a uniform manifold and a plain chip with the homogeneous model using different viscosity averaging schemes. The experimental data shows a maximum pressure drop of 158 kPa at a heat flux of 227 W/cm^2. The pressure variation in the test section is rather large, and a segmented analysis is warranted to take into account for vapor phase density variation with pressure. For the current comparison however, the mean properties over the test section are utilized. This assumption is quite reasonable for OMM configuration due to the very low pressure drop values.

An increasing trend of pressure drop with heat flux is observed for the experimental data as seen in Fig. 49. The homogenous model underpredicts when compared with the experimental data for all the viscosity models. The model shows an increasing trend in pressure drop vs. heat flux plot, similar to the experimental data points. The Owens viscosity model shows the least MEA (30%) compared to the other models, while the Dukler et al. viscosity model shows the highest error (52%). Ciccihitti et al. and Lin et al. underpredicted with an MAE of 30%. McAdams et al. and Akers et al. showed an average

MAE of 37%, while Beattie and Whalley and Dukler et al. showed a maximum error of 51% in the predicted pressure drop values.

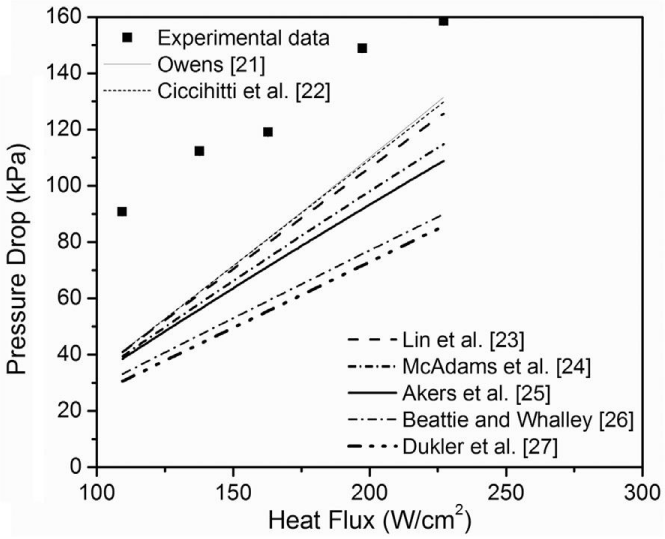

Figure 60: Pressure drop variation with heat flux of seven averaging viscosity schemes using the homogeneous flow model for a plain chip with a uniform manifold

6.2.2 Microchannel chip with uniform manifolds

Figure 50 shows the comparison of experimental data with homogeneous model (seven viscosity models) for uniform manifold and the microchannel chip. A maximum pressure drop of ~60 kPa is obtained at the highest heat flux (225 W/cm^2). The reduction in pressure drop compared to the plain chip is due to the increased cross-sectional area provided by the introduction of microchannels.

The model underpredicts compared to the experimental data. Similar performance to plain chip is observed, with Owens showing the least MAE of 36% and Dukler et al. showing the highest MAE of 67%. The remaining viscosity models fall between Owens and Dukler et al.; this trend continues for all configurations tested in this work. The model also shows an increasing trend of pressure drop with heat flux.

For both chips (plain and microchannel) with uniform manifold block, the homogeneous flow model underpredicted the experimental data. However, similar increasing trend of the experimental pressure drop with heat flux was observed with the model. Among the seven viscosity averaging schemes used to calculate the frictional component of the homogeneous flow model, Dukler et al. showed the lowest deviation. The average MAE% for Owens viscosity scheme was 33%, while Dukler et al. showed the maximum deviation (average MAE of 59%) for both chips. McAdams et al. scheme was in the middle of the predictive models tested. In Figs. 3 and 4, the uncertainty bars are similar to the symbol sizes, and hence are not visible in the plots.

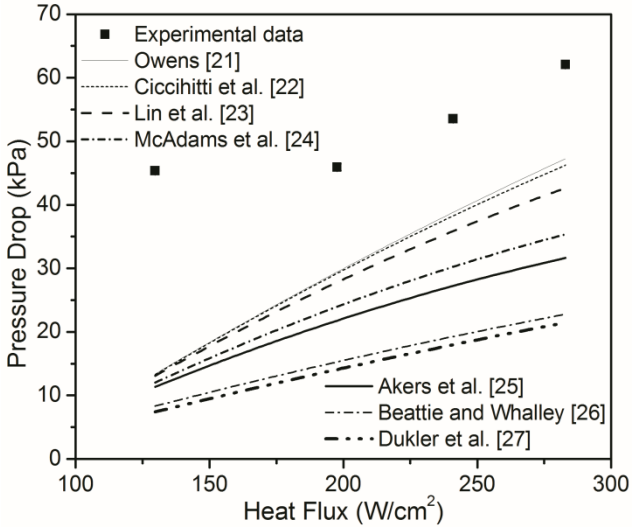

Figure 61: Pressure drop variation with heat flux of seven averaging viscosity schemes [21-27] using the homogeneous flow model for a microchannel chip with a uniform manifold.

6.2.3 Plain chip with tapered manifolds

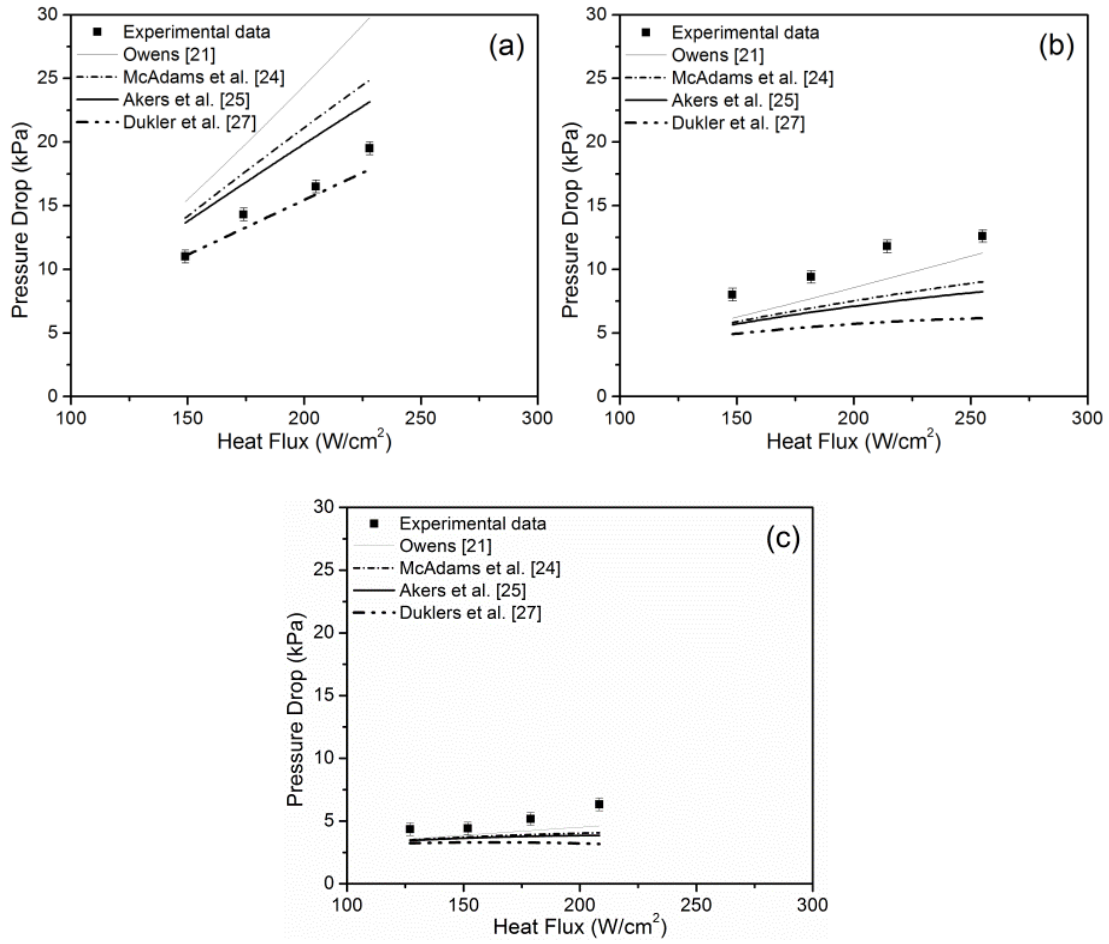

Figure 62: Comparison of the homogeneous flow model with different averaging viscosity schemes and experimental data over a plain chip for taper gradient varying from (a) 2%, (b) 4%, and (c) 6%.

All viscosity models (independent of the configuration) followed the same pattern as shown in Fig. 51 with Owens [66] predicting the highest value and Dukler et al. the lowest. Hence, for tapered manifold modeling presented in this section, only four viscosity models were selected (Owens [66], McAdams et al., Akers et al. and Dukler et al.).

The experimental data for the plain chip with three levels of manifold taper gradient were compared with the homogeneous model as shown in Fig. 51. The introduction of the

tapered manifold showed a dramatic reduction in the pressure drop compared to the uniform manifold. For all tapered configurations, the maximum pressure drop was below 20 kPa at the highest heat flux. The pressure drop reduced as the taper gradient increased steadily from 2% to 4% and 6% as shown in cases (a)-(c).

Figure 51 (a) shows the 2% taper gradient manifold data comparison. The homogeneous flow predictions show good agreement with Dukler et al. and overpredicted with the other viscosity averaging models. Experimental pressure drop increased with increasing heat flux. This trend is predicted well with all models. An MAE of 5% was obtained with Dukler et al. an average of 32% for McAdams and Akers et al., and 45% for Owens.

For 4% taper gradient shown in Fig. 51 (b), the experimental pressure drop is seen to increase with heat flux, although at a lower rate as compared to 2% taper gradient shown in Fig. 5(a). Owens underpredicted with the experimental data with an average MAE of 18%. A similar increasing trend was observed as the experimental data with the viscosity model. Dukler et al. viscosity model showed a maximum deviation of 45%. McAdams et al. and Akers et al. showed an average MAE of 30%.

Figure 51 (c) compares the 6% taper gradient data with the homogeneous model. The experimental data shows only a modest increase with heat flux. All models also showed a slight increment in pressure drop with increasing heat flux, similar to the Dukler et al. viscosity model for 4% taper gradient. A maximum deviation of 37% MAE was obtained with the Dukler et al. viscosity model which shows a slight decrement with increasing heat flux.

6.2.4 Microchannel chip with tapered manifolds

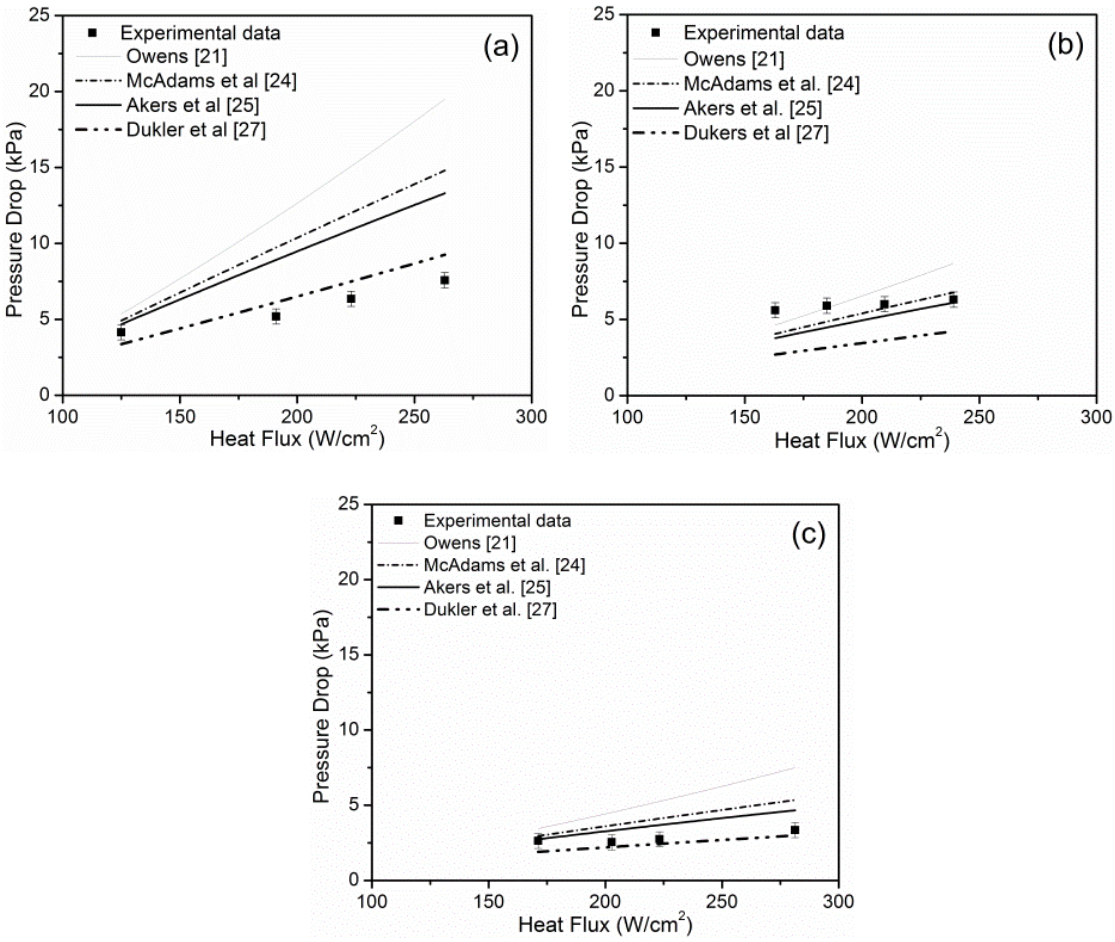

Figure 63: Comparison of the homogeneous flow model with different averaging viscosity schemes and experimental data over microchannel chip for taper gradient varying from (a) 2%, (b) 4%, and (c) 6%.

Figure 52 shows a comparison of the experimental data with three tapered manifolds with a microchannel chip using various viscosity schemes under the homogeneous model. The combination of tapered manifold and microchannel yielded a sharp reduction in the pressure drop for all three taper gradients. For this configuration and for all taper gradients, the maximum pressure drop was below 10 kPa for all heat fluxes.

For all three taper gradients, in general the homogeneous flow model shows good agreement with the experimental data. For 2% taper gradient, Dukler et al. gave the lowest MAE% while Owens was the highest MAE%, due to overprediction. For both 4% and 6% taper gradient, McAdams et al. and Akers et al. gave an average MAE 18% and 21% respectively. A similar increasing trend of pressure drop with heat flux was observed with all the viscosity models. Figure 52 shows that the homogeneous flow model can be used to predict microchannel and tapered configuration with reasonable MAE% of below 30% for a given viscosity averaging model.

The comparisons presented in Figs. 51 and 52 show that the pressure drop variation with heat flux follows different trends for different taper gradients. This variation is further explored and the role of different pressure drop components is presented in the following section.

6.3 Discussion

6.3.1 Overall pressure drop predictions for tapered manifolds

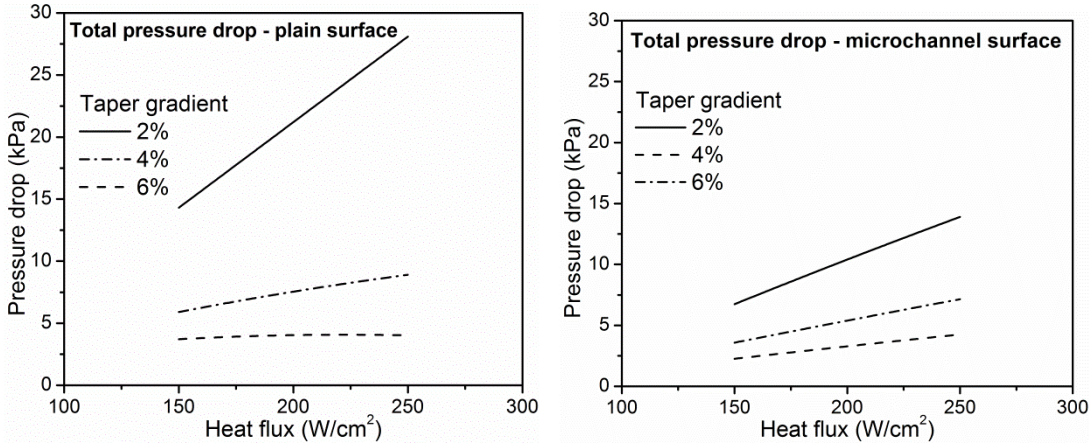

Figure 64: Comparison of the homogeneous model flow model for taper gradients varying from 2% - 6% for (a) plain and (b) microchannel chip

From the results, it is seen that the pressure drop trend with heat flux seems to be affected by the taper gradient. This is further explored for both plain and microchannel chips using the McAdams et al. viscosity averaging model. Figure 53 shows the comparison of three taper gradients for both (a) plain chip, and (b) microchannel chip. The plain chip (Fig 53a) shows the highest pressure drop with increasing trend for 2% taper gradient. The trend changes for 4% and 6% taper gradient, while the latter (6%) shows a slight decreasing trend with increasing heat flux. The microchannel chip as seen in Fig 53 (b) shows an increasing trend in pressure drop with heat flux for all taper configurations. However, the slope varies between the taper gradients and the steepness of the slope decreases from 2% to 6%.

In order to explore the reasons for the differences in pressure drop trends with heat flux, the variations in the individual components of the pressure drop from the homogeneous flow model for plain and microchannel chips are analyzed further.

6.3.2 Plain chip

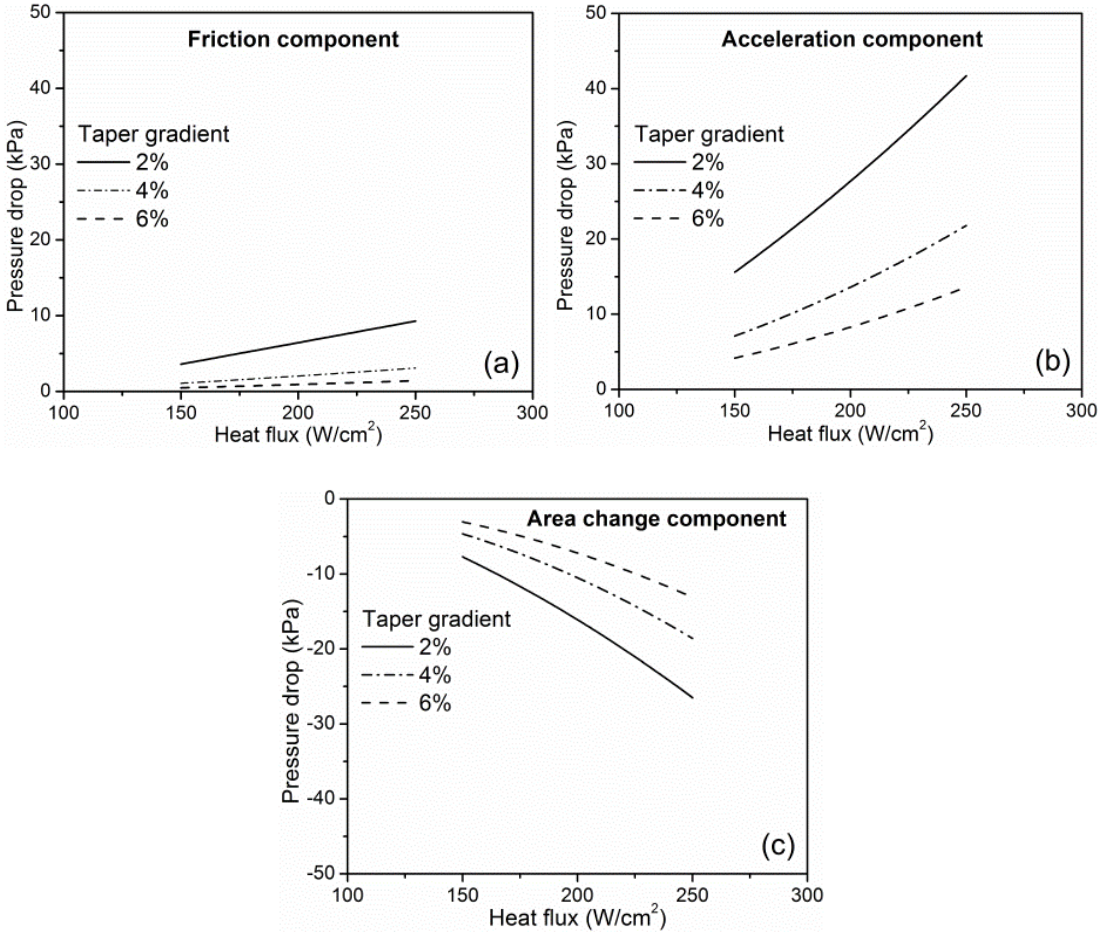

Figure 65 (a) – (c): Variation of the individual pressure drop components with heat flux for all tapered manifold configurations for a plain chip, (a) friction component, (b) acceleration component, and (c) area change component.

Figure 54 shows the variation of friction, acceleration and area change components of the homogeneous model for all three taper gradients with a plain chip. For the frictional component (Fig. 8a), an increasing trend is observed with an increase in heat flux for all taper gradients, with 2% gradient showing the highest pressure drop contribution. For the acceleration component (Fig. 54b), similar increasing trend is observed for all taper gradients. The overall acceleration contribution is significantly greater than the frictional component. At 250 W/cm^2 for 2% taper gradient, the acceleration contribution is >40 kPa while the frictional component is ~10 kPa. For both friction and acceleration, the increasing trend of the model is due to the increase in exit quality and two-phase flow length with increase in heat flux.

Figure 54 (c) shows the area change contribution to the homogeneous pressure model. The pressure drop yields negative values indicating a pressure recovery. An increasing trend is observed for pressure recovery from the area component with the 2% taper gradient showing the highest pressure recovery. The slight decreasing trend in the total pressure drop with heat flux observed in Fig. 7 (a) for 6% taper gradient can be explained through the sum of the three components shown in Fig. 8. The increase in pressure recovery from the area change contribution at higher heat fluxes balances the increase in the combined friction and acceleration components for this case.

6.3.3 Microchannel chip

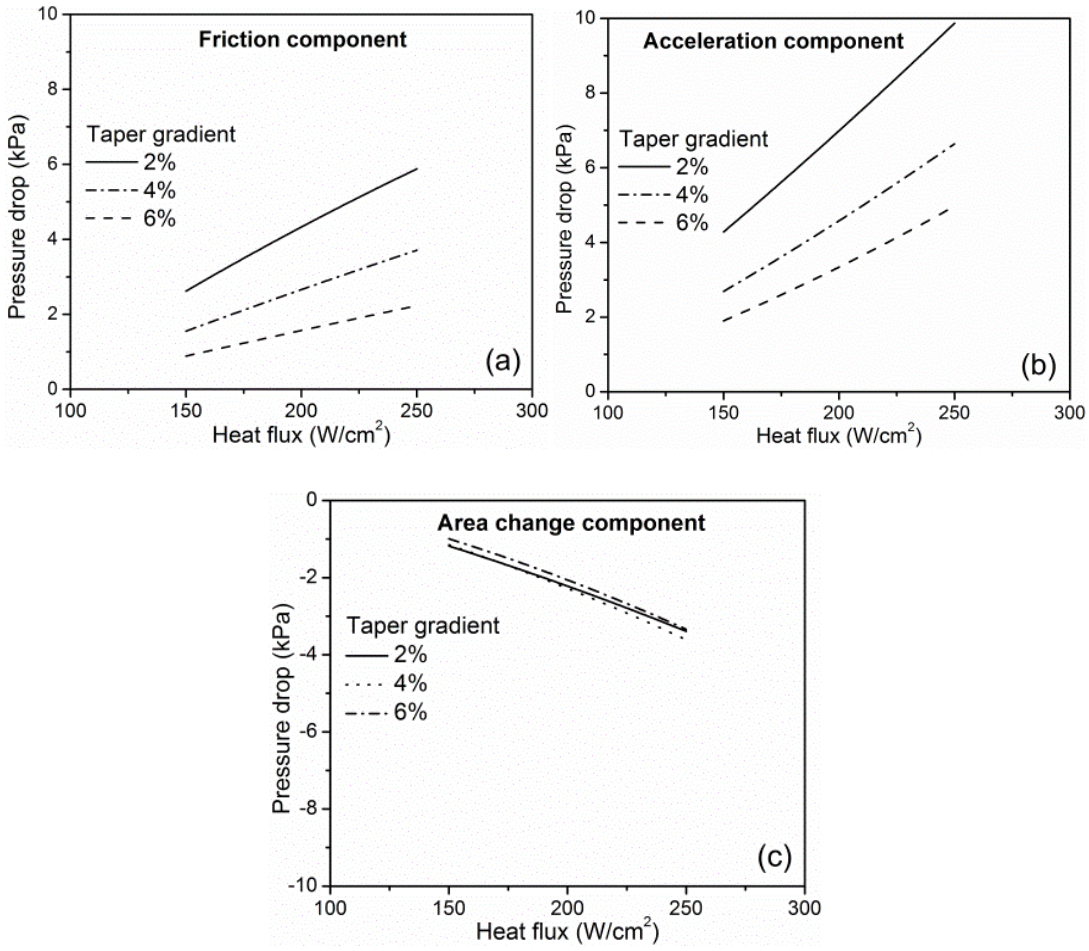

Figure 66 (a) – (c): Variation of the individual pressure drop components with heat flux for three tapered manifold configurations for a microchannel chip, (a) friction component, (b) acceleration component, and (c) area change contribution.

Similar to Fig. 54, Fig. 55 shows the comparison of three taper gradients for various components of the homogeneous model for a microchannel test chip. Both friction and acceleration terms (Fig. 9 a-b) show increasing trend with 2% taper gradient having the maximum pressure drop contribution. Unlike the plain chip, the pressure drop contributions for friction and acceleration components are close to each other (<10 kPa).

For the area change component for the microchannel chip (Fig. 55 c), the differences between the three tapers are not as pronounced as they were for the plain chip (Fig. 54 c). Also, the pressure drop recovery is significantly lower than the plain chip counterparts. Mass flux is identified as the key reason behind the lower values and minimal difference between the three tapers. The microchannels provide a higher cross-sectional area for a given manifold height as compared to a plain chip. This reduces the effect of taper which in-turn reduces the overall variation in mass flux. The reduced pressure drop values are due to the reduction in mass flux, which is a squared term in the numerator of Eq. (9).

It is seen from Figs. 53-55 that the pressure recovery due to increasing flow cross-sectional area due to taper is instrumental in overall reduction in pressure drop. The taper thus is seen to be advantageous in providing an increased area to accommodate vapor generated along the flow length and also in providing a pressure recovery effect.

6.3.4 Visualization

In order to explore the applicability of the homogeneous flow model further, flow patterns were investigated to study the relative phase distributions in the flow channels. A high speed camera was used to take images at 3000 frames per second of flow boiling for all configurations. The manifold was made of a transparent material facilitating flow visualization over the chips. Figure 56 shows a sequence of three successive high speed images 0.2s apart for a plain chip with tapered manifold (2% gradient) at a heat flux of 150 W/cm^2. The images show both the liquid and vapor phases mixed well within the plain chip region. The main assumption of uniform phase velocities in the homogeneous flow modeling is valid for the plain chip with tapered manifold as seen from the successive

images. Hence, it is expected that the model will predict well with experimental data for the plain chip. This supports the results between the experimental data and model prediction seen earlier in Figs. 53 and 55.

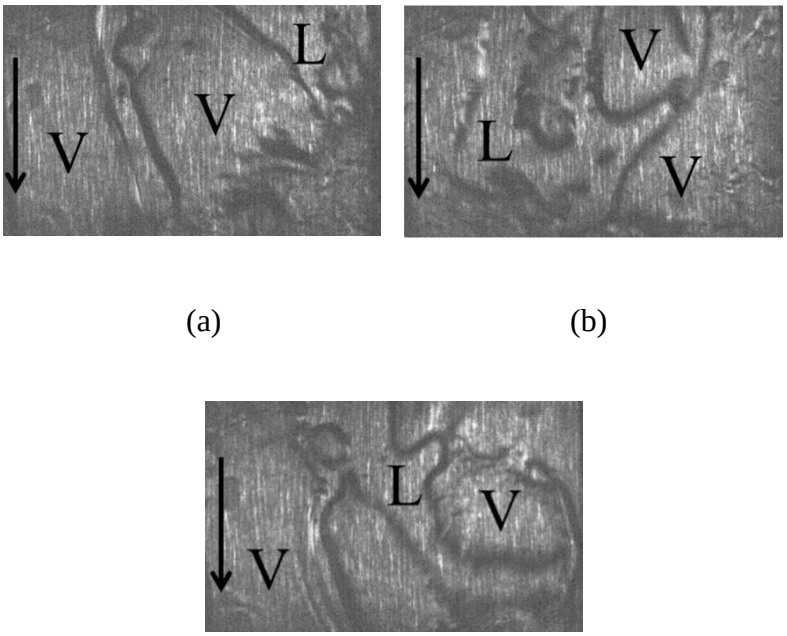

(a) (b)

(c)

Figure 67: Successive images at 0.2 s time interval of flow boiling in tapered manifold geometry and a plain chip.

Figure 57 shows similar successive images of flow boiling with a microchannel chip at a heat flux of 150 W/cm^2. The channels are filled with liquid, and vapor flows in the manifold region. Nucleation occurs within the channel and feeds the vapor present in the gap. Nucleating bubbles formed within the channels are forced away due to the high velocity in the manifold. The liquid and vapor travel together due to bubbles expanding in the microchannels and the manifold region. Lateral expansion of these bubbles is not seen.

The channeling effect seen for the plain chip is not present, and the two phases seem to act as a pseudo single-phase. Expectedly, we see that the homogeneous model predictions match well with the experimental pressure drop data.

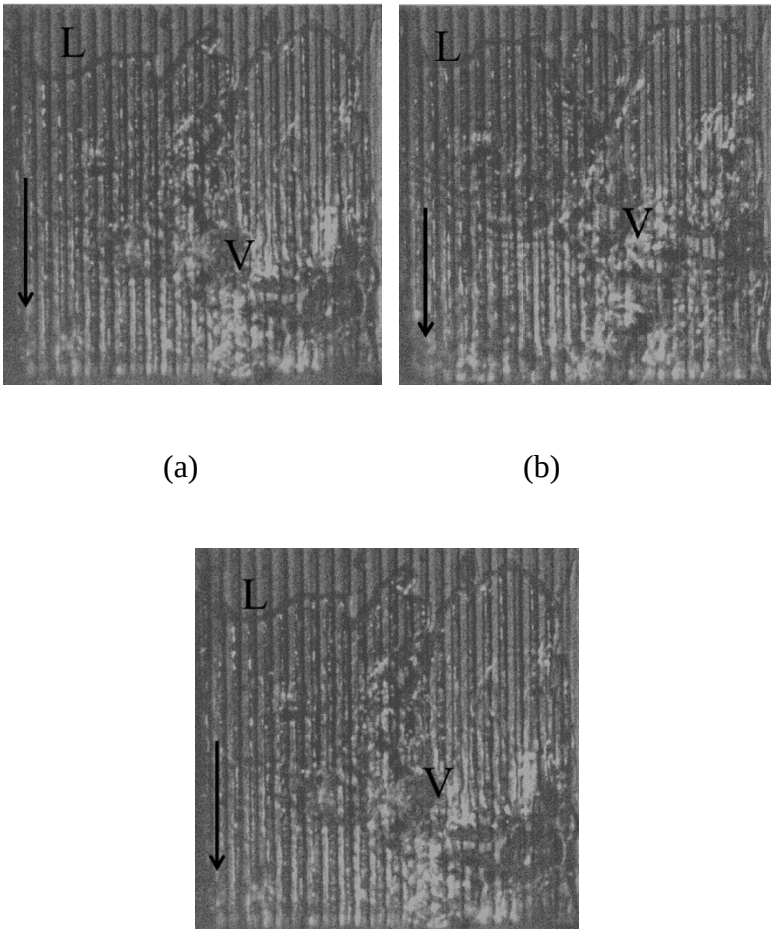

(a) (b)

(c)

Figure 68: Successive images at 0.2 s time interval of flow boiling in tapered manifold geometry and the microchannel chip.

6.4 Conclusions

Pressure drop analysis for the OMM geometry was conducted using the homogeneous flow model. Experimental data for uniform and tapered manifold configuration using plain and microchannel chips were used for comparison with the model. Seven viscosity averaging schemes model were employed in the homogeneous flow. The following conclusions are made from the study:

1. The combination of the tapered manifold geometry with microchannel was effective in reducing the pressure drop in the flow boiling system. For the three taper gradients of 2%, 4% and 6%, a pressure drop of less than 10 kPa at the highest flux was obtained with the microchannel chip.
2. Seven viscosity averaging schemes were used with all geometries to obtain the frictional pressure drop for the homogeneous flow model. Regardless of the configuration, all models followed a similar trend in predicting the pressure drop as a function of heat flux. Owens predicted the highest pressure drop value while Dukler et al. predicted the lowest value.
3. For the uniform manifold, the homogeneous flow model underpredicted the experimental data for both plain and microchannel chips. Owens viscosity model showed the least error with an MAE of 33%.
4. For tapered manifold and a plain chip, the homogeneous flow model showed different pressure drop trends depending on the magnitude of the taper gradient. An increasing trend with low MAE was obtained with 2% and 4% taper gradient. However, a slight decreasing trend was observed with 6% taper gradients.

5. Availability of a larger flow area and pressure recovery due to increase in the cross-sectional area along the flow length were seen to be responsible in reducing the overall pressure drop in the tapered manifold geometry.
6. The homogeneous model is able to predict pressure drop values for a plain chip with uniform or tapered manifold configurations within the 30-40% MAE.
7. For a microchannel chip and tapered configuration, the homogeneous model predicts well within a reasonable MAE of <30% with McAdams et al. and Akers et al. viscosity averaging schemes. A similar increasing trend of pressure drop with increasing heat flux from the homogeneous flow model was seen.
8. High speed images show that for both chips and tapered manifold geometry, the fundamental assumption of the homogeneous model of equal liquid and vapor velocity holds well. This was also confirmed through the pressure drop predictions from the homogeneous flow model for this geometry.

Chapter 7: Critical Heat Flux and Heat Transfer Modeling

7.1 Critical Heat Flux

The main objective of this study has been to enhance flow boiling heat transfer while reducing pressure drop by understanding the underlying mechanism of the liquid-vapor interaction in microchannels. Flow boiling in closed microchannels, i.e. microchannels with a cover plate, has been studied in the past for dissipating high heat fluxes. However, the liquid-vapor interaction inside the confined space leads to flow boiling instabilities, which in turn, reduces the thermal performance of the system. The underlying physics of bubble generation in small passages indicates that the nucleating bubbles be removed from the channel region without disrupting the incoming liquid supply stream for limiting the pressure drop. Low pressure drop in a system facilitates uniformity of saturation temperature along the flow length and a lower pumping power.

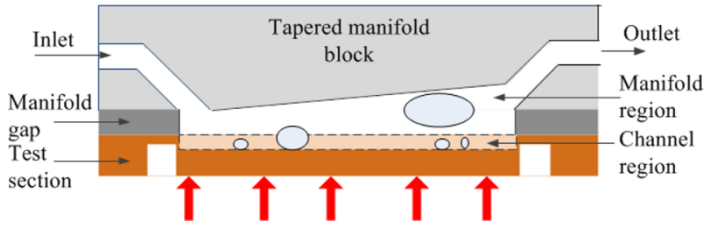

Figure 69: Schematic of the test section showing bubbles emerging from the channel and expanding

A schematic representation of a bubble emerging from the microchannel into the manifold and expanding in the flow direction is also shown. The bubbles nucleate at the bottom of the channel and expand over the fin top, unlike traditional microchannels where bubbles expand in both the upstream and downstream directions within the microchannels causing flow disruption and instability. The introduction of a tapered manifold gap above

the microchannels allows the bubbles to grow and expand into the manifold region. This mechanism allows constant rewetting of the channel area assisting in improving the heat transfer performance. The pressure drop during flow boiling in constant area channels consists of frictional, gravitational and acceleration components. An additional pressure recovery term is introduced for the tapered geometry due to its increasing flow cross-sectional area causing a reduction in flow velocity [92]. The kinetic energy of the flow is thus converted into a pressure recovery term. It is given by:

$$-\left(\frac{dP}{dz}_{taper,area}\right) = \frac{-2G^2 v_f}{A_c}\left[1 + x\left(\frac{v_{fg}}{v_f}\right)\right]\frac{dA}{dz} \tag{29}$$

Where A_c is the cross-sectional area, G is the mass flux, v_f is the specific volume of the liquid, v_{fg} is the difference in the specific volume of saturated liquid, x is the quality and dA/dz is the change in cross-sectional area along the channel length (two-phase region). This additional term introduces a pressure recovery effect during the bubble expansion in the flow direction, and consequently a reduction in the total pressure drop is obtained [93].

Literature has shown that an increase in mass flux in a uniform cross-section channel leads to an increase in the heat dissipation rate in a flow boiling system, but is accompanied with a large increase in pressure drop. Cikim et al. [94] obtained a pressure drop of over 100 kPa at a mass flux of 5000 kg/m^{2}s (Re ~4500) for a circular channel of inner diameter 249 µm, while the pressure drop was 1450 kPa with a mass flux of 20,000 kg/m^{2}s (Re ~25,000). These extremely high pressure drops are unacceptable in many practical

applications, such as electronics cooling. For the current geometry, a moderately higher liquid inertia force is employed to increase the performance, but the pressure drop does not increase disproportionately as the tapered configuration provides a pressure recovery component, which increases with increasing heat flux. This provides a pathway for extending critical heat flux (CHF) beyond 1 kW/cm^2 as this has been a target heat flux in electronics cooling applications. By combining the two approaches of utilizing separate liquid-vapor pathways and increasing mass flux, a heat dissipation beyond 1 kW/cm^2 is demonstrated in this work.

The flow rates used in the earlier study with tapered manifold were in the range of 40-80 mL/min with an inlet gap of 127 µm. This resulted in a liquid Reynolds number (Re) of 219-437 based on the inlet flow area in the microchannels and the gap regions. In this section, higher flow rates of 140-300 mL/min (corresponding Re of 766-1642) are employed using the taper configuration that resulted in the highest pressure recovery during the earlier tests. Kalani and Kandlikar [92] studied the effect of taper over 2%-6% range and found that the pressure drop was lowest with the 6% taper. Hence the 6% taper is selected in the present work. The microchannel dimensions are selected on the basis of results from previous work that showed the best heat transfer performance; channel width 200 µm, channel depth 200 µm and fin width also 200 µm. The microchannels were machined on a CNC machine with an average roughness of ~2 µm.

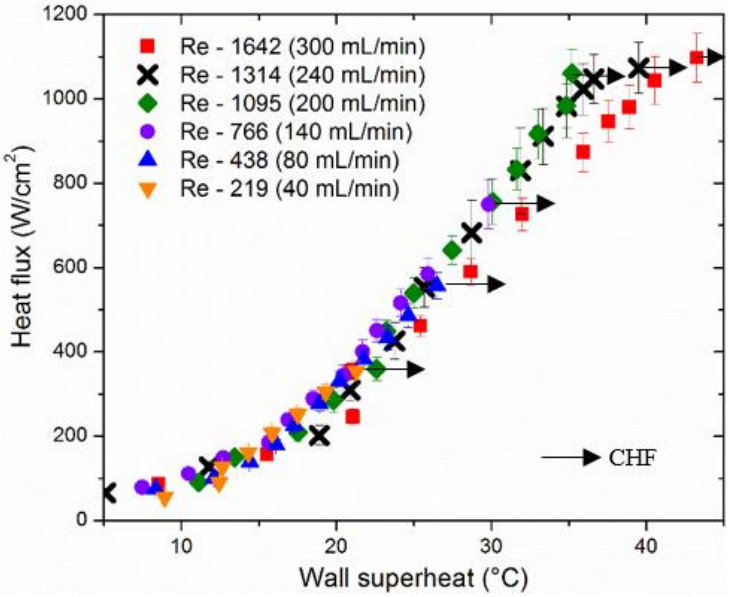

Figure 70: Flow boiling curve for different flow rates (CHF increasing with Re) in open microchannels with tapered gap.

Figure 70 shows the flow boiling curve plotted with wall superheat versus heat flux for different inlet liquid Reynolds numbers, Re. The inlet liquid was slightly subcooled by 10 °C to prevent two-phase flow at the inlet. The arrows in the figure represent the CHF point for the given flow rate. For 40 mL/min, a CHF of less than 400 W/cm^2 was recorded. A CHF of over 1 kW/cm^2 (1.07 kW/cm^2) was recorded with a wall superheat of 35°C for 200 mL/min. A maximum heat flux of 1.1 kW/cm^2 was obtained at a wall superheat of 43°C for 300 mL/min. However, for the flow rate of 350 mL/min, the test was terminated before CHF because the wall superheat exceeded 45°C. This was done to prevent structural damage to the manifold block.

Figure 71 shows the CHF versus the inlet Re comparing the current experimental data and closed microchannel data [95]. It is seen from Fig. 71 that CHF increases with an increase in flow rate, in agreement with a similar trend reported in literature. A significant increase in CHF is observed when Re increases from 219 to 1095. However, only a

marginal increase in CHF is obtained for flow rates over 200 mL/min. This trend of increasing CHF with Re indicates that the bubbles emerging from the microchannels are assisted by the inertia force of the liquid flowing in the manifold region and allow for constant rewetting of the channels.

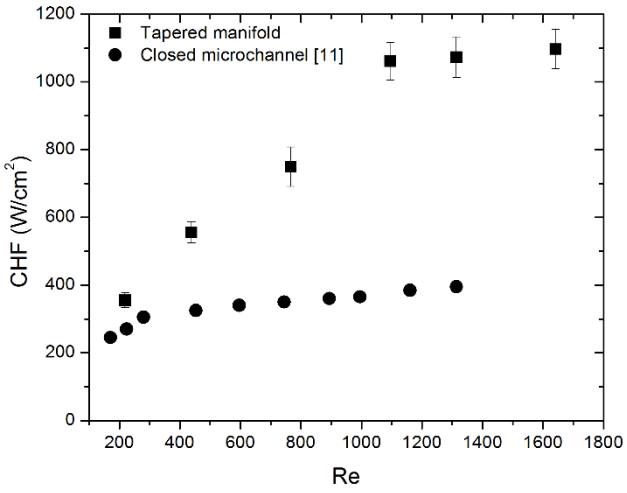

Figure 71: CHF versus inlet Reynolds number.

For comparison, the closed microchannel data by Balasubramanian et al. [95] is also shown in Fig. 3. A maximum CHF of 395 W/cm^2 was recorded for Re of 1313. However, the relatively high heat flux obtained in the closed microchannel is due to the large channel depth of 1190 µm used in their work, compared to a channel depth of only 200 µm in the present tapered configuration. The large channel depth provide additional surface area, but resulted in a large wall superheat similar to tall fin structures. As a result, the heat transfer coefficient (HTC) would suffer in the closed microchannels. Before comparing the HTC performance, the pressure drop results are presented next to show the pressure recovery

arising from the tapered gap. The liquid inertia and forces encountered during rapid evaporation play a key role on the CHF enhancement.

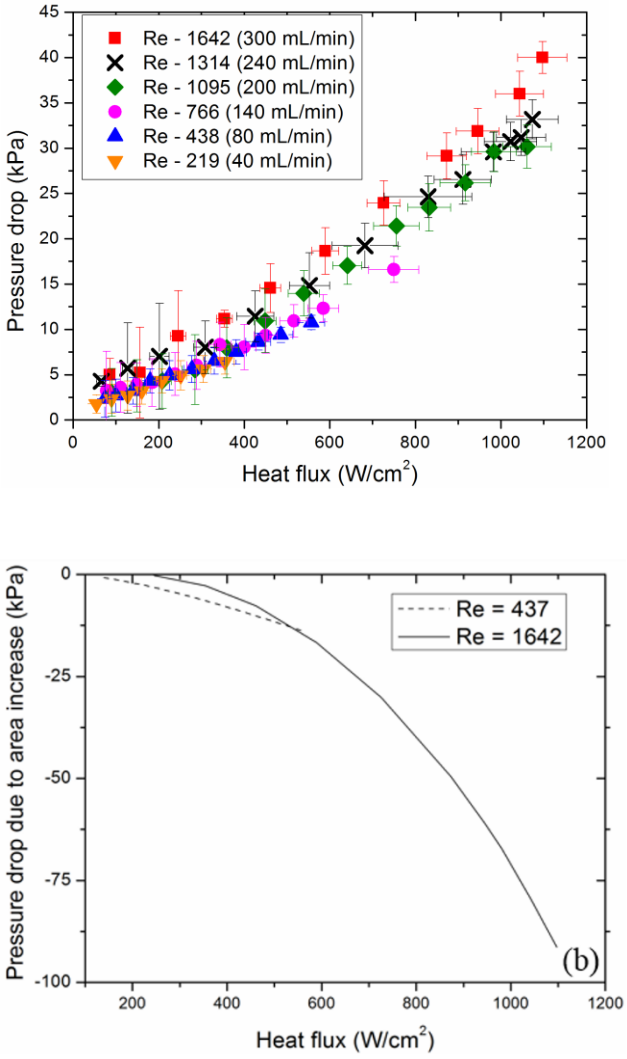

Figure 72: Pressure drop versus heat flux (a) Different inlet flow Reynolds numbers for the open microchannels with a tapered gap and (b) Pressure drop component due to area increase versus heat flux for two flow rates

Figure 72 shows a plot of pressure drop versus heat flux for different Re from the present work. For lower flow rates (40 and 80 ml/min), a maximum pressure drop of less

than 10 kPa was recorded for a heat flux of ~500 W/cm^2. For a heat flux of 1 kW/cm^2, a pressure drop of 30 kPa was recorded for a flow rate of 200 mL/min. A maximum pressure drop of 42 kPa was obtained for a CHF of 1.1 kW/cm^2 at the highest flow rate of 300 mL/min. This increasing trend of pressure drop with increasing Re was consistent with the trends observed in literature. The pressure drop increases with heat flux; however, for higher flow rates beyond a certain value, the pressure drop seems to increase without any appreciable gain in the CHF values. The actual value of pressure drop is considerably lower than that for microchannels due to the pressure recovery term arising from Eq. (1).

The effect of the pressure recovery component is further explored in Fig. 72(b). The plot shows a comparison of the pressure drop due to area increase against heat flux for two Reynolds number. The pressure drop values are shown as negative to indicate a pressure recovery. For Re = 1642, a pressure recovery of ~ 90 kPa at a q"$_{CHF}$ of 1.09 kW/cm^2 was obtained, while for Re = 438 at q"$_{CHF}$ of 556 W/cm^2, a pressure recovery of ~14 kPa. These two pressure recovery values represent the amount of pressure recovered and in turn, the amount by which the overall system pressure is lowered. However, at a lower flow rate (Re = 438) the overall pressure recovery is lower since the heat flux is low, showing that at higher heat fluxes we can get substantial pressure recovery (up to 90 kPa). This recovery term is not present in the traditional microchannel geometry since there is no increase in the flow cross-sectional area. Hence the closed microchannel will have a much higher pressure drop.

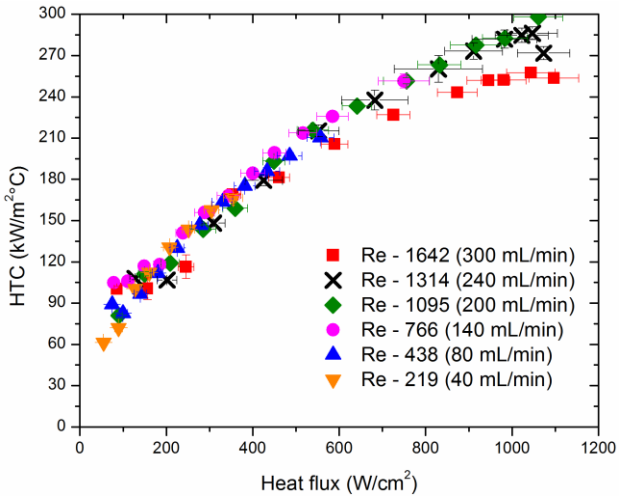

Figure 73: HTC vs heat flux for different flow Reynolds numbers.

The thermal performance of the tapered gap geometry is also presented in terms of the HTC plots as shown in Fig. 5. A maximum HTC of 295 kW/m^2°C is obtained for Re of 1095 and 1314. The HTC increased with increasing Re up to Re=1095 and then remained constant for Re=1314; however for Re of 1642 a lower value of HTC was obtained. Thus it is seen that the performance increases up to a certain value of Re, beyond which the performance is seen to deteriorate. This is the result of vapor blanketing caused by the bubbles spreading into microchannels at higher flow rates as the bubbles are unable to overcome the increased inertia force from the liquid flowing in the gap region. Instead of assisting the bubble removal, the higher liquid inertia forces prevent the bubbles from emerging from the microchannels into the taper region. The bubbles spreading into the microchannels dispel the liquid present in the channels and cause rapid growth of dry patches in the liquid film under the vapor core occupying the channels. Comparing the performance with closed microchannels, the tapered configuration HTC (295 kW/m^2°C) is significantly higher than that for the closed microchannels (~25 kW/m^2°C). As discussed

earlier, the tall fins in the closed microchannels lead to a higher wall superheat and consequently a lower HTC. Thus, higher CHF and higher HTC are obtained in the present configuration at lower pressure drops as compared to the closed microchannels. A detailed summary of the heat transfer performance in various enhanced microchannel geometries is discussed in the next section.

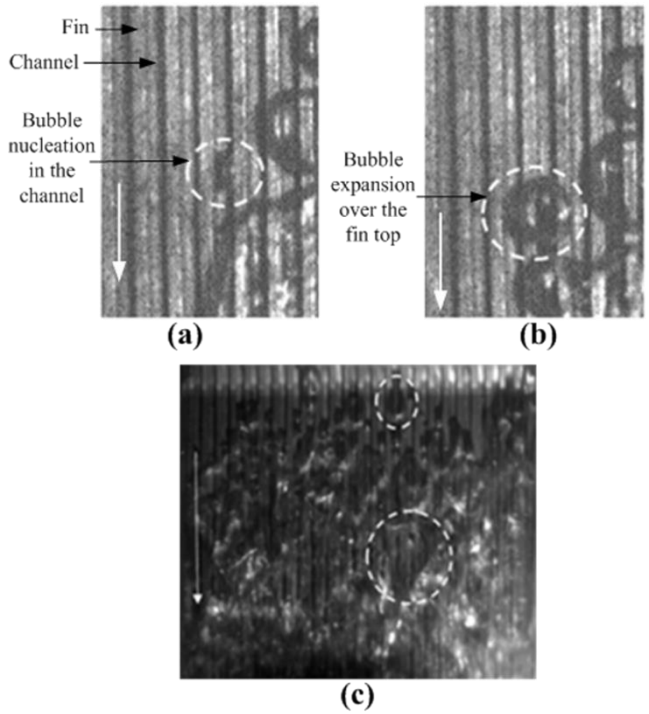

Figure 74: High speed images of bubble nucleation and expansion in the tapered manifold region at (a-b) low heat flux (~100 W/cm^2) and (c) high heat flux (~500 W/cm^2)

Figures 74(a-b) show the bubble nucleation and expansion process at a low heat flux of ~100 W/cm^2. Flow direction is from top to bottom in all images. The images were recorded at 10,000 frames per second (fps) and show only a part of the heated microchannel surface observed through a transparent cover. The bubble nucleates at the base of the channel and expands on the fin top in the gap region. This allows the channel region to be continually

rewetted by the oncoming liquid. The underlying bubble nucleation and emergence pattern observed here is also seen to exist at higher heat fluxes as well.

Figure 74 (c) shows the entire microchannel surface (image taken at 3000 fps) at a heat flux of ~500 W/cm^2 for Re of 1095. The circle near the inlet (top of the figure) indicates the bubble nucleating in the channel and expanding on the fin top as seen during low heat fluxes. The second highlighted area shows liquid presence (confirmed by nucleation of a small bubble in the liquid film under a larger vapor bubble in the manifold above) in the channel downstream while a mixture of liquid-vapor occupies the manifold (gap) region.

Utilizing the liquid inertia force to expel the bubbles rapidly from the microchannels, the CHF as well as HTC are improved, while the pressure drop is kept low. However, beyond a certain flow rate, the liquid inertia force prevents bubble migration and subsequent expansion in the manifold region. Figure 75 shows an image of the bubble nucleation and departure taken at 10,000 fps for 300 mL/min. The image shows bubbles nucleating and departing in the channel region and no expansion is seen in the manifold gap region. For higher flow rates (>240 mL/min), the nucleating bubble is unable to expand in the manifold region and is forced to remain in the channel. This eventually leads to bubble expansion within the microchannel followed by dry spot formation under the vapor core occupying the channel and an earlier CHF.

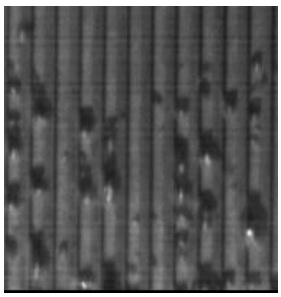

Figure 75: Shows high speed image of bubble nucleation and departure at 300 mL/min

Balancing the liquid inertia force with respect to bubble emergence dynamics from the microchannels into the manifold is seen to be a critical factor in enhancing the flow boiling heat transfer. The taper gap manifold introduces a pressure recovery term and is responsible for the low pressure drop in this configuration. Further gains are expected by analyzing the effect of these forces in arriving at the optimum microchannel and taper dimensions.

7.2 Comparison with Literature

Table 6: Summarizes the heat transfer and pressure drop performance of various enhanced microchannel geometries by various researchers.

Author, year	**Microchannel geometry**	**q''_{CHF} (W/cm^2)**	**h ($kW/m^2°C$)**	**ΔP (kPa)**	**G (kg/m^2s)**
Kandlikar et al. 2013	OMM	506	193	60	394
Balasubramanian et al., 2013	Stepped microchannel	420	168	<5	664
Miner et al., 2013	Diverging microchannel	489	Not reported	40	1000
Zhu et al., 2015	Microchannels with micropillar array	1470	~260	> 65	1849
Woodcock et al., 2015	Piranha pin fin	700	75	120	7000
Fazeli et al., 2015	Vapor venting	380	~150	28	40
Current work, Kalani and Kandlikar, 2015	Tapered manifold	1073	290	30	984

Table 6 shows the results of previous investigators focusing on high heat dissipation. It is seen that the pressure drop becomes significantly higher for cases approaching >1 kW/cm^2. Zhu et al. [96] employed short fins in their 500 μm square microchannel. They did not

report the pressure drop value with G=1849 kg/m^{2}s, but indicate that the pressure drop is 65 kPa at a heat flux value of ~1250 W/cm^2. The heat flux of 1073 W/cm^2 is reached in the current work with a high heat transfer coefficient of 290 kW/m^2°C with a simultaneous low pressure drop value of 30 kPa with a relatively modest mass flux of 984 kg/m^{2}s.

7.3 Heat Transfer Modeling

Accurate prediction of heat transfer coefficient can assist in cost reduction and proper design of heat exchanger, evaporator, boilers and other two-phase equipment. A correlation can further assist in understanding the effect of various parameters in flow boiling. A number of issue arises in predicting accurate heat transfer coefficient data which include presence of instabilities in the system and different range of parameters such as heat flux, mass flux and geometry. Furthermore, the complex nature of flow boiling in microchannel which include liquid-vapor interaction, nucleation of bubbles, thin film evaporation and presence of expanding bubbles within thin film make it extremely difficult to present a comprehensive analytical model.

The correlation work can be broadly classified into two categories. Experimental researchers developing correlation to present their own data and in some cases some additional data with similar parameters form the first category. The second category of correlations are developed based on a large data set bank involving a number of parameters over a wide range of values. These correlations tend to cover a broad range of operating values and are hence more valuable. For the current work, the heat transfer coefficient experimental data is compared with Kandlikar and Balasubramanian [97]. This correlation is an extension of the original Kandlikar correlation [98,99] which was applicable only to the turbulent flow data. The new correlation focuses on microchannel geometries and low Reynold number values. The correlation introduces the laminar flow utilizing the single-phase, all liquid heat transfer coefficient based on $Re_{LO.}$ The correlation is formulated based on the available data in the literature and is given below:

For $Re_{LO} \geq 100$;

$$h_{TP} = larger\ of \quad \begin{matrix} h_{TP,NBD} \\ h_{TP,CBD} \end{matrix} \tag{30}$$

$$h_{TP,NBD} = 0.6683Co^{-0.2}(1-x)^{0.8}h_{LO} + 1058Bo^{0.7}(1-x)^{0.8}F_{Fl}h_{LO} \tag{31}$$

$$h_{TP,CBD} = 1.136Co^{-0.9}(1-x)^{0.8}h_{LO} + 667.2Bo^{0.7}(1-x)^{0.8}F_{Fl}h_{LO} \tag{32}$$

Where Co is the convection number, Bo is the boiling number, h_{LO} is the single-phase all-liquid flow heat transfer coefficient and F_{fl} is the fluid surface parameter.

For $100 \leq Re_{LO} \leq 1600$

$$h_{LO} = \frac{Nu_{LO}k}{D_h} \tag{33}$$

The convection number is the modified Martinelli parameter used in correlating flow boiling heat transfer and is given by:

$$Co = \left(\frac{1-x}{x}\right)^{0.8}\left(\frac{\rho_v}{\rho_l}\right)^{0.5} \tag{34}$$

The boiling number is used to non-dimensionalize heat flux with mass flux and latent heat and is given by the formula below:

$$Bo = \frac{q^{"}}{Gh_{LV}} \tag{35}$$

F_{Fl} is a fluid-surface dependent parameter and represents the nucleation characteristics of the liquid on the given heater surface, which in turn depends on the nucleation site density, fluid properties responsible for nucleation, etc. However, such information is not easily available and has been correlated against combinations for commercial tube surfaces. The table below provides values of this parameter of fluids on copper and brass surfaces:

Table 7: Recommended F_{FL} values

Fluid	**F_{FL}**
Water	1.00
R-11	1.30
R-12	1.50
R-13B1	1.31
R-22	2.20
R-113	1.30
R-114	1.24
R-134a	1.63
R-152a	1.10
R-32/R-132	3.30
R-141b	1.80
R-124	1.00
Kerosene	0.488

For the current work, copper and water is used for the experimental work hence $F_{fl} = 1$ for the model. The two-phase heat transfer coefficient correlation has two dominant modes of heat transfer, the nucleate boiling region – where the nucleate boiling is the dominant

mode of heat transfer and the convection dominant region – where the heat transfer takes place from wall to liquid through convection. Below is the list of key assumptions used in the model to calculate predicted heat transfer coefficient values.

7.3.1 Key assumptions:

1. Heat flux values calculated based on projected area (100 mm^2)
2. Nusselt number for liquid only is taken as 8.24 based on parallel plate/flat channel and constant heat flux boundary condition assumption
3. Average hydraulic diameter (between inlet and exit outlets) value are assumed
4. Similar to hydraulic diameter, average mass flux values are used for the calculation
5. Values assumed for remaining calculations: k_L = 0.663 W/mK, ρ_L = 958 kg/m^3, ρ_V = 0.6 kg/m^3 and h_{LV} = 2257 kJ/kg

7.3.2 Results

Experimental heat transfer coefficient values were compared with the predicted values from the correlation at varying heat fluxes and flow rates. The below graph (Fig. 76) shows the comparison with HTC as the y-axis and heat flux as the x-axis for 200 mL/min. A single flow rate is shown in the figure below to avoid overcrowding of data points and predicted values for multiple flow rates. Similar graphs with varying flow rates are provided in the appendix section of the document.

A maximum HTC of 295 kW/m^2°C was obtained at heat flux of over 1 kW/cm^2 and shows an increasing trend of HTC with heat flux. The model underpredicts compared to the experimental data. The model also shows an increasing trend of HTC with heat flux, similar to the experimental data points. The predicted values show good agreement with experimental values with an average MAE of 21%. Further improvements in the model can be made by refining some of the key assumptions.

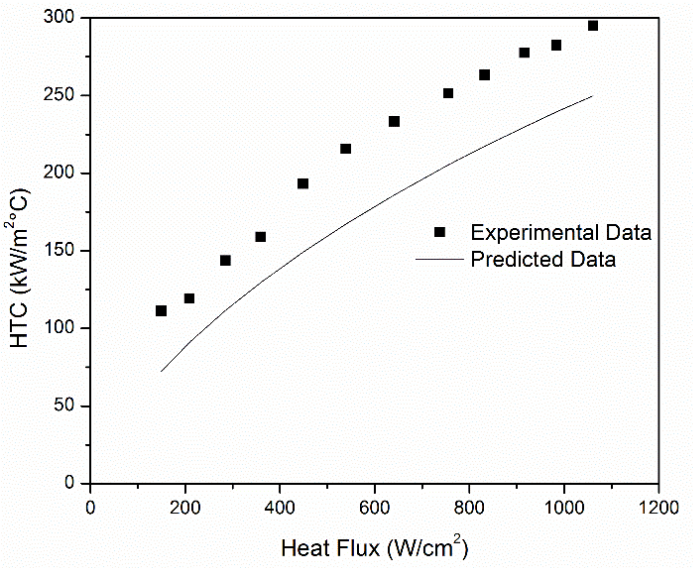

Figure 76: Comparison of heat transfer coefficient experimental data with Kandlikar and Balasubramanian [97] correlation for 200 mL/min

Figure 77 compares the experimental heat transfer coefficient values for all tested flow rates with the predicted values from correlation. The axes for Fig. 77 are given by the experimental and predicted heat transfer coefficient values with ±30% error lines. Good prediction of predicted heat transfer coefficient values with an average of ±30% is seen with the correlation. For the flow rates between 80 mL/min – 240 mL/min, an average MAE of ~30% is observed. The lowest flow rate of 40 mL/min and the highest flow rate of 300 mL/min show the maximum error. This can be explained with the calculation of h_{LO}

values. The single phase heat transfer coefficient values (h_{LO}) increases with increase in flow rate, the current model does not take that into account. The h_{LO} value is calculated based on the Nusselt number which provides a good estimation. Improved model accuracy will be observed with the above mentioned change and some further more refinement of the key assumptions.

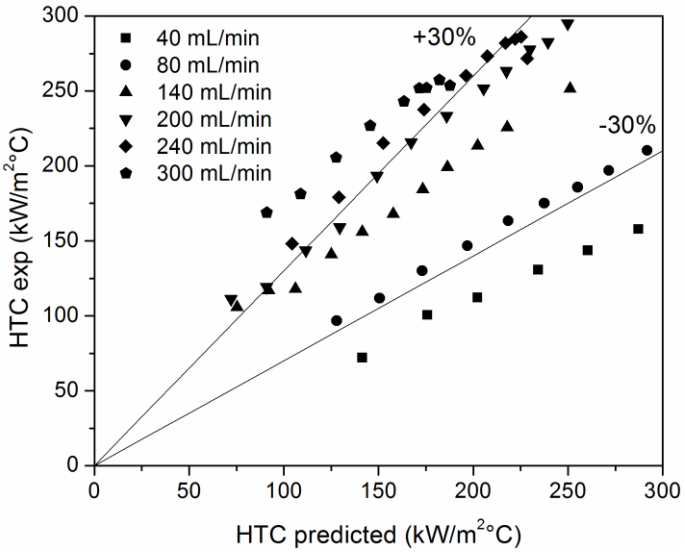

Figure 77: Comparison of heat transfer coefficient experimental data with Kandlikar and Balasubramanian [97] correlation for all flow rates

7.3.3 Conclusions

The aim of this study was to extend the CHF values by increasing the flow rate, but without the pressure drop penalty associated with higher flow rates. The following conclusions are made through this study:

1. A maximum CHF of 1.07 kW/cm^2 was obtained with a HTC of 295 kW/m^2°C and a pressure drop of 30 kPa using a moderately high flow rate of 200 mL/min.
2. CHF increased with increasing flow rate. A marginal increase in CHF value was observed beyond the flow rate of 200 mL/min and with CHF almost plateauing with further increase in flow rate. The wall superheat at CHF however increased at higher flow rates.
3. High HTC values of 295 kW/m^2°C were obtained with 200 and 240 mL/min. Further increase in the flow rate yielded lower HTC values of below 250 kW/m^2°C.
4. Low pressure drop system was achieved with the tapered manifold. The pressure recovery effect due to the additional increase in flow cross-sectional area assists in providing a low pressure drop in the system. For 1 kW/cm^2 a pressure drop of 30 kPa was obtained for a flow rate of 200 mL/min.
5. High speed visualization showed the bubble nucleation process in the geometry, the bubbles nucleated in the channel and grew over the channel fin in the manifold region. The flow was not affected by the localized growth of bubbles in the microchannel.
6. Vapor blanketing caused due bubble spreading in the channel region is seen as one of the key reason of performance deterioration at higher flow rates. The

increased liquid inertia does not allow bubble to exit the channel region and forces expansion in the channel.

7. Heat transfer coefficient experimental values were compared with Kandlikar and Balasubramanian correlation for all flow rates. Good prediction (an average MAE of ±30%) with similar increasing trend of HTC with heat flux was observed.
8. The highest and the lowest flow rate showed the maximum error (>±30%). Model accuracy can be improved by refining some of the key assumptions.

Chapter 8: Key Contributions and Recommendations

8.1 Contributions

Since the realization in 2001 that flow boiling in microchannels can lead to high heat flux dissipation in electronics cooling applications, significant research has been directed toward improving the CHF and HTC of this configuration [2]. It had become apparent by 2005 [33,37,38] that microchannels could not deliver on this promise, and so intense research ensued in order to overcome the difficulties in achieving this high heat flux dissipation requirement. With this background, the goal of this research was to develop a novel flow boiling microchannel system with water which would provide significant performance enhancement (high heat dissipation in excess of 1 kW/cm^2) for electronics cooling applications. Extensive experimental work with the new geometry has been conducted, covering a wide range of parameters so as to study their effect on the flow boiling performance. Flow régimes, underlying mechanisms, heat transfer performance as well as pressure drop modeling associated with the new geometry was undertaken. Theoretical modeling led to some key findings which enabled a surpassing of the 1 kW/cm^2 barrier with a high HTC and low pressure drop. Some of the key findings from this work are listed below:

- Open microchannels with uniform and tapered manifold geometry were designed and tested experimentally. The purpose of the new design was to provide additional area for the expanding bubbles along the flow length of the microchannels in order to enhance heat transfer performance and reduce the pressure drop penalty. An experimental investigation of various parameters such as flow rates, manifold

configuration and geometrical parameters (which include manifold height and taper gradient) was undertaken.

- Combining liquid inertia with a tapered gap configuration provided a new mechanistic pathway for increasing the heat transfer performance. This design allowed the nucleating bubbles to emerge from the microchannels and expand in the gap region, thus creating a separate liquid-vapor pathway.
- This study achieved the goal of dissipating heat fluxes beyond 1 kW/cm^2 using microchannels. Using the open microchannel geometry with a 6% taper manifold and an inlet liquid flow Reynolds number of 1095, a record high critical heat flux (CHF) of 1.07 kW/cm^2 with a heat transfer coefficient of 295 $kW/m^2°C$ and a pressure drop of 30 kPa was recorded.
- A pressure drop model was developed in order to simulate pressure drop in this geometry. It employed a homogeneous flow model for the variable flow cross-sectional area geometry. An additional area term was presented in the model to account for the tapered geometry due to its increasing flow cross-sectional area. This additional term introduced a pressure recovery effect during the bubble expansion in the flow direction and, consequently, was critical in explaining the low pressure drop observed experimentally. The model showed good prediction capability (MAE<30%) with the experimental data obtained in this study.
- High speed visualization was conducted at 3,000 - 10,000 frames per second in order to identify the underlying mechanism of bubble generation and two-phase flow pattern in the system. Flow regimes, bubble ebullition cycle for plain and microchannel surfaces and CHF mechanisms were explained through high speed

visualization. The images also showed that the high liquid inertia resulted in the bubbles being expelled rapidly from the microchannels, improving the CHF and HTC without adversely affecting the pressure drop.

- The experimental data for the heat transfer coefficient was compared with an established correlation from literature for all flow rates. Good prediction (average MAE ~±30%) with a similar increasing trend of heat transfer coefficient with heat flux was observed with the correlation.
- The work was disseminated through 5 international journal articles and 5 international conference proceedings.

8.2 Future Recommendation

Open microchannels with manifolds were introduced in this work, providing insight into a new mechanistic pathway to improve heat transfer and pressure drop performance in high heat flux dissipating applications. Experimental work over a wide range of parameters and modeling were conducted for the new geometry. Some suggestions for the future work are presented below, based on the current research work done so far:

- Performance enhancement: The aim to exceed a CHF value of 1 kW/cm^2 was achieved with a high heat transfer coefficient and low pressure drop. Further reduction in wall superheat with an accompanying increase in heat transfer coefficients beyond 500,000 W/m^2°C is desirable. In literature, porous structures have been used to reduce wall temperature by enabling early bubble nucleation and providing additional nucleation sites inside the porous matrix. It is recommended to use a porous structure on this geometry for the purpose of lowering wall superheat and possibly increasing the heat transfer performance.
- Experimental parameters: Investigation on the effects of subcooling and orientation can be conducted to provide a more comprehensive understanding of the new geometry proposed in this study.
- New geometries and extending CHF: CHF occurs due to vapor preventing rewetting of the heater surface. With the understanding from the flow visualization of the current study, new gemoetries with varying inlet/outlet configuration can be designed to further extend CHF.
- Predictive tools: Pressure drop modeling was undertaken using the homogeneous flow model. Improved accuracy with experimental data can be obtained by using

the separated flow model approach. Preliminary work on heat transfer coefficient correlation was also undertaken. Further improvements in the model can be made by including a wider range of data generated for a more comprehensive parameter range as well as different orientations.

- CHF modeling: Develop a CHF model using the insight gained from the flow visualization studies, specifically by considering the forces acting on the nucleating bubbles as they emerge from the microchannel region into the manifold area. This would provide understanding of the physical phenomena (primary forces acting inside the channel) of the tapered geometry, which can lead to refinement of the geometry.
- Numerical approach: Simulating two-phase flow with similar experimental conditions of bubble nucleation in the new microchannel geometry can lead to further understanding of the underlying mechanisms.

Chapter 9: References

[1] BCC Research, 2014, "The Market for Thermal Management Technologies" [Online]. Available: http://www.bccresearch.com/market-research/semiconductor-manufacturing/thermal-management-smc024j.html.

[2] Kandlikar, S. G., 2012, "History, advances, and challenges in liquid flow and flow boiling heat transfer in microchannels: A critical review," J. Heat Transf., **134**(3).

[3] Zhang, Y. P., Yu, X. L., Feng, Q. K., and Zhang, R. T., 2009, "Thermal performance study of integrated cold plate with power module," Appl. Therm. Eng., **29**(17–18), pp. 3568–3573.

[4] Chu, R. C., Simons, R. E., Ellsworth, M. J., Schmidt, R. R., and Cozzolino, V., 2004, "Review of cooling technologies for computer products," IEEE Trans. Device Mater. Reliab., **4**(4), pp. 568–585.

[5] D. BTuckerman, D. B., and Pease, R. F. W., "High-performance heat sinking for VLSI," Electron Device Lett IEEE, **2**(5), pp. 126–129.

[6] Colgan, E. G., Furman, B., Graham, W., LaBianca, N., Magerlein, J. H., Polastre, R. J., Rothwell, M. B., Bezama, R. J., Choudhary, R., Marston, K., Toy, H., Wakil, J., and Zitz, J., 2005, "A practical implementation of silicon microchannel coolers for high power chips," 2005 IEEE Twenty First Annual IEEE Semiconductor Thermal Measurement and Management Symposium, pp. 1–7.

[7] Tullius, J. F., Vajtai, R., and Bayazitoglu, Y., 2011, "A Review of Cooling in Microchannels," Heat Transf. Eng., **32**(7-8), pp. 527–541.

[8] Kalani, A., Kandlikar, S.G, 2013, "Enhanced Pool Boiling with Ethanol at Sub-Atmospheric Pressures for Electronics Cooling," ASME J. Heat Transf. Spec. Issue Electron. Cool. Accept. Publ. J. Heat Transf.

[9] Chan, M. A., Yap, C. R., and Ng, K. C., 2009, "Pool Boiling Heat Transfer of Water on Finned Surfaces at Near Vacuum Pressures," J. Heat Transf., **132**(3), pp. 031501–031501.

[10] Guglielmini, G., Misale, M., and Schenone, C., 2002, "Boiling of saturated FC-72 on square pin fin arrays," Int. J. Therm. Sci., **41**(7), pp. 599–608.

[11] Krishnamurthy, S., and Peles, Y., 2010, “Flow boiling heat transfer on micro pin fins entrenched in a microchannel,” J. Heat Transf., **132**(4), pp. 1–10.

[12] Launay, S., Fedorov, A. G., Joshi, Y., Cao, A., and Ajayan, P. M., 2006, “Hybrid micro-nano structured thermal interfaces for pool boiling heat transfer enhancement,” Microelectron. J., **37**(11), pp. 1158–1164.

[13] Sloan, A., Penley, S., and Wirtz, R. A., 2009, “Sub-atmospheric pressure pool boiling of water on a screen-laminate enhanced surface,” 25th Annual IEEE Semiconductor Thermal Measurement and Management Symposium, 2009. SEMI-THERM 2009, pp. 246–253.

[14] Jaikumar, A., and Kandlikar, S. G., 2015, “Enhanced pool boiling heat transfer mechanisms for selectively sintered open microchannels,” Int. J. Heat Mass Transf., **88**, pp. 652–661.

[15] Yao, Z., Lu, Y.-W., and Kandlikar, S. G., 2011, “Effects of nanowire height on pool boiling performance of water on silicon chips,” Int. J. Therm. Sci., **50**(11), pp. 2084–2090.

[16] Khanikar, V., Mudawar, I., and Fisher, T., 2009, “Effects of carbon nanotube coating on flow boiling in a micro-channel,” Int. J. Heat Mass Transf., **52**(15-16), pp. 3805–17.

[17] Betz, A. R., Xu, J., Qiu, H., and Attinger, D., 2010, “Do surfaces with mixed hydrophilic and hydrophobic areas enhance pool boiling?,” Appl. Phys. Lett., **97**(14), pp. 141909 –141909–3.

[18] Mudawar, I., 2013, “Recent Advances in High-Flux, Two-Phase Thermal Management,” J. Therm. Sci. Eng. Appl., **5**(2), pp. 021012–021012.

[19] Kandlikar, S. G., and Grande, W. J., 2003, “Evolution of Microchannel Flow Passages–Thermohydraulic Performance and Fabrication Technology,” Heat Transf. Eng., **24**(1), pp. 3–17.

[20] Frank P. Incropera, Theodore L. Bergman, Adrienne S. Lavine, and David P. DeWitt, Fundamentals of Heat and Mass Transfer, John Wiley & Sons, 2011.

[21] Nukiyama, S., 1934, “Maximum and minimum values of heat transmitted from metal to boiling water under atmospheric pressure,” Soc. Mech. Eng. Jpn. -- J., **37**(206), pp. 367–374.

[22] Kandlikar, S. G., Shoji, M., and Dhir, V. K., 1999, Handbook of Phase Change: Boiling and Condensation, Taylor & Francis.

[23] Carey, V. P., 1992, Liquid-Vapor Phase-Change Phenomena: An Introduction To The Thermophysics Of vaporization and condensation in heat transfer equipment: An Introduction to the Thermophysics of Vaporization & Condensation in Heat Transfer Equipment, Taylor & Francis.

[24] Harirchian, T., and Garimella, S. V., 2009, "Effects of channel dimension, heat flux, and mass flux on flow boiling regimes in microchannels," Int. J. Multiph. Flow, **35**(4), pp. 349–362.

[25] Taitel, Y., and Dukler, A. E., 1976, "A model for predicting flow regime transitions in horizontal and near horizontal gas-liquid flow," AIChE J., **22**(1), pp. 47–55.

[26] Peles, Y., Contemporary Perspectives on Flow Boiling Instabilities in Microchannels and Minichannels, Begell House.

[27] Kandlikar, S. G., 2006, "Nucleation characteristics and stability considerations during flow boiling in microchannels," Exp. Therm. Fluid Sci., **30**(5), pp. 441–447.

[28] Hsu, Y. Y., 1961, "On size range of active nucleation cavities on heating surface," ASME Meeting WA-177, Nov 26-Dec 1 1961, American Society of Mechanical Engineers (ASME), p. 7.

[29] Satish G, K., 2006, "Nucleation characteristics and stability considerations during flow boiling in microchannels," Exp. Therm. Fluid Sci., **30**(5), pp. 441–447.

[30] Hetsroni, G., Mosyak, A., Segal, Z., and Ziskind, G., 2002, "A uniform temperature heat sink for cooling of electronic devices," Int. J. Heat Mass Transf., **45**(16), pp. 3275–3286.

[31] Wang, G., Cheng, P., and Wu, H., 2007, "Unstable and stable flow boiling in parallel microchannels and in a single microchannel," Int. J. Heat Mass Transf., **50**(21–22), pp. 4297–4310.

[32] Wu, H. Y., and Cheng, P., 2004, "Boiling instability in parallel silicon microchannels at different heat flux," Int. J. Heat Mass Transf., **47**(17–18), pp. 3631–3641.

[33] Steinke, M. E., and Kandlikar, S. G., 2004, "An Experimental Investigation of Flow Boiling Characteristics of Water in Parallel Microchannels," J. Heat Transf., **126**(4), pp. 518–526.

[34] Bergles, A. E., and Kandlikar, S. G., 2005, "On the Nature of Critical Heat Flux in Microchannels," J. Heat Transf., **127**(1), pp. 101–107.

[35] Kandlikar, S. G., 2002, "Fundamental issues related to flow boiling in minichannels and microchannels," Exp. Therm. Fluid Sci., **26**(2–4), pp. 389–407.

[36] Mukherjee, A., and Kandlikar, S. G., 2009, "The effect of inlet constriction on bubble growth during flow boiling in microchannels," Int. J. Heat Mass Transf., **52**(21–22), pp. 5204–5212.

[37] Qu, W., and Mudawar, I., 2003, "Measurement and prediction of pressure drop in two-phase micro-channel heat sinks," Int. J. Heat Mass Transf., **46**(15), pp. 2737–2753.

[38] Liu, D., and Garimella, S. V., 2007, "Flow boiling heat transfer in microchannels," J. Heat Transf., **129**(10), pp. 1321–1332.

[39] Kandlikar, S. G., Kuan, W. K., Willistein, D. A., and Borrelli, J., 2006, "Stabilization of flow boiling in microchannels using pressure drop elements and fabricated nucleation sites," Trans. ASME J. Heat Transf., **128**(4), pp. 389–96.

[40] Wang, G., Cheng, P., and Bergles, A. E., 2008, "Effects of inlet/outlet configurations on flow boiling instability in parallel microchannels," Int. J. Heat Mass Transf., **51**(9–10), pp. 2267–2281.

[41] Kuo, C.-J., and Peles, Y., 2008, "Flow Boiling Instabilities in Microchannels and Means for Mitigation by Reentrant Cavities," J. Heat Transf., **130**(7), pp. 072402–072402.

[42] Koşar, A., Kuo, C.-J., and Peles, Y., 2005, "Boiling heat transfer in rectangular microchannels with reentrant cavities," Int. J. Heat Mass Transf., **48**(23–24), pp. 4867–4886.

[43] Zhang, T., Tong, T., Chang, J.-Y., Peles, Y., Prasher, R., Jensen, M. K., Wen, J. T., and Phelan, P., 2009, "Ledinegg instability in microchannels," Int. J. Heat Mass Transf., **52**(25–26), pp. 5661–5674.

[44] Qu, W., and Siu-Ho, A., 2009, “Experimental study of saturated flow boiling heat transfer in an array of staggered micro-pin-fins,” Int. J. Heat Mass Transf., **52**(7–8), pp. 1853–1863.

[45] Qu, W., and Siu-Ho, A., 2009, “Measurement and prediction of pressure drop in a two-phase micro-pin-fin heat sink,” Int. J. Heat Mass Transf., **52**(21–22), pp. 5173–5184.

[46] Koşar, A., Rafet Özdemir, M., and Keskinoz, M., 2010, “Pressure drop across micro-pin heat sinks under unstable boiling conditions,” Int. J. Therm. Sci., **49**(7), pp. 1253–1263.

[47] Law, M., Lee, P.-S., and Balasubramanian, K., 2014, “Experimental investigation of flow boiling heat transfer in novel oblique-finned microchannels,” Int. J. Heat Mass Transf., **76**, pp. 419–431.

[48] Liburdy, J. A., Pence, D. V., and Narayanan, V., 2008, “Flow Boiling Characteristics in a Fractal-Like Branching Microchannel Network,” pp. 97–106.

[49] Lu, C. T., and Pan, C., 2009, “A highly stable microchannel heat sink for convective boiling,” J. Micromechanics Microengineering, **19**(5), p. 055013.

[50] Alam, T., Poh Seng Lee, and Yap, C. R., 2013, “Effects of surface roughness on flow boiling in silicon microgap heat sinks,” Int. J. Heat Mass Transf., **64**, pp. 28–41.

[51] Alam, T., Lee, P. S., Yap, C. R., Jin, L., and Balasubramanian, K., 2012, “Experimental investigation and flow visualization to determine the optimum dimension range of microgap heat sinks,” Int. J. Heat Mass Transf., **55**(25–26), pp. 7623–7634.

[52] Megahed, A., 2011, “Experimental investigation of flow boiling characteristics in a cross-linked microchannel heat sink,” Int. J. Multiph. Flow, **37**(4), pp. 380–393.

[53] Cho, E. S., Koo, J.-M., Jiang, L., Prasher, R. S., Kim, M. S., Santiago, J. G., Kenny, T. W., and Goodson, K. E., 2003, “Experimental study on two-phase heat transfer in microchannel heat sinks with hotspots,” Ninteenth Annual IEEE Semiconductor Thermal Measurement and Management Symposium, 2003, pp. 242–246.

[54] Jiang, L., Koo, J.-M., Wang, E., Bari, A., Cho, E. S., Ong, W., Prasher, R. S., Maveety, J., Kim, M. S., Kenny, T. W., Santiago, J. G., and Goodson, K. E., 2002, "Cross-Linked Microchannels for VLSI Hotspot Cooling," pp. 13–17.

[55] Balasubramanian, K., Lee, P. S., Teo, C. J., and Chou, S. K., 2013, "Flow boiling heat transfer and pressure drop in stepped fin microchannels," Int. J. Heat Mass Transf., **67**, pp. 234–252.

[56] David, M. P., Miler, J., Steinbrenner, J. E., Yang, Y., Touzelbaev, M., and Goodson, K. E., 2011, "Hydraulic and thermal characteristics of a vapor venting two-phase microchannel heat exchanger," Int. J. Heat Mass Transf., **54**(25–26), pp. 5504–5516.

[57] Fazeli, A., Mortazavi, M., and Moghaddam, S., 2015, "Hierarchical biphilic micro/nanostructures for a new generation phase-change heat sink," Appl. Therm. Eng., **78**, pp. 380–386.

[58] Miner, M. J., Phelan, P. E., Odom, B. A., and Ortiz, C. A., 2013, "Experimental Measurements of Critical Heat Flux in Expanding Microchannel Arrays," J. Heat Transf., **135**(10), pp. 101501–101501.

[59] Miner, M. J., Phelan, P. E., Odom, B. A., and Ortiz, C. A., 2013, "An Experimental Investigation of Pressure Drop in Expanding Microchannel Arrays," J. Heat Transf., **136**(3), pp. 031502–031502.

[60] Miner, M. J., Phelan, P. E., Odom, B. A., Ortiz, C. A., Prasher, R. S., and Sherbeck, J. A., 2013, "Optimized Expanding Microchannel Geometry for Flow Boiling," J. Heat Transf., **135**(4), pp. 042901–042901.

[61] Cooke, D., and Kandlikar, S. G., 2011, "Pool boiling heat transfer and bubble dynamics over plain and enhanced microchannels," J. Heat Transf., **133**(Compendex).

[62] Steinke, M. E., and Kandlikar, S. G., 2004, "Control and effect of dissolved air in water during flow boiling in microchannels," Int. J. Heat Mass Transf., **47**(8–9), pp. 1925–1935.

[63] Cooke, D., and Kandlikar, S. G., 2012, "Effect of open microchannel geometry on pool boiling enhancement," Int. J. Heat Mass Transf., **55**(4), pp. 1004–1013.

[64] Hetsroni, G., Mosyak, A., and Segal, Z., 2001, "Nonuniform temperature distribution in electronic devices cooled by flow in parallel microchannels," IEEE Trans. Compon. Packag. Technol., **24**(1), pp. 16–23.

[65] Zhang, L., Wang, E. N., Goodson, K. E., and Kenny, T. W., 2005, "Phase change phenomena in silicon microchannels," Int. J. Heat Mass Transf., **48**(8), pp. 1572–1582.

[66] Chen, T., and Garimella, S. V., 2006, "Measurements and high-speed visualizations of flow boiling of a dielectric fluid in a silicon microchannel heat sink," Int. J. Multiph. Flow, **32**(8), pp. 957–971.

[67] Tamanna, A., and Lee, P. S., 2015, "Flow boiling heat transfer and pressure drop characteristics in expanding silicon microgap heat sink," Int. J. Heat Mass Transf., **82**, pp. 1–15.

[68] Tibiriçá, C. B., and Ribatski, G., 2013, "Flow boiling in micro-scale channels – Synthesized literature review," Int. J. Refrig., **36**(2), pp. 301–324.

[69] Mudawar, I., 2011, "Two-phase microchannel heat sinks: Theory, applications, and limitations," J. Electron. Packag. Trans. ASME, **133**(4).

[70] Balasubramanian, P., and Kandlikar, S. G., 2005, "Experimental Study of Flow Patterns, Pressure Drop, and Flow Instabilities in Parallel Rectangular Minichannels," Heat Transf. Eng., **26**(3), pp. 20–27.

[71] Collier, J. G. (John G., 1972, Convective boiling and condensation [by] John G. Collier, McGraw-Hill, London, New York.

[72] Field, B. S., and Hrnjak, P., 2007, "Adiabatic Two-Phase Pressure Drop of Refrigerants in Small Channels," Heat Transf. Eng., **28**(8-9), pp. 704–712.

[73] Ducoulombier, M., Colasson, S., Bonjour, J., and Haberschill, P., 2011, "Carbon dioxide flow boiling in a single microchannel – Part I: Pressure drops," Exp. Therm. Fluid Sci., **35**(4), pp. 581–596.

[74] Kawahara, A., Chung, P. M.-Y., and Kawaji, M., 2002, "Investigation of two-phase flow pattern, void fraction and pressure drop in a microchannel," Int. J. Multiph. Flow, **28**(9), pp. 1411–1435.

[75] Niu, H., Pan, L., Su, H., and Wang, S., 2009, “Flow Pattern, Pressure Drop, and Mass Transfer in a Gas−Liquid Concurrent Two-Phase Flow Microchannel Reactor,” Ind. Eng. Chem. Res., **48**(3), pp. 1621–1628.

[76] Bowers, M. B., and Mudawar, I., 1994, “High flux boiling in low flow rate, low pressure drop mini-channel and micro-channel heat sinks,” Int. J. Heat Mass Transf., **37**(2), pp. 321–332.

[77] Bowers, M. B., and Mudawar, I., 1994, “Two-Phase Electronic Cooling Using Mini-Channel and Micro-Channel Heat Sinks: Part 2—Flow Rate and Pressure Drop Constraints,” J. Electron. Packag., **116**(4), pp. 298–305.

[78] Saisorn, S., and Wongwises, S., 2008, “An inspection of viscosity model for homogeneous two-phase flow pressure drop prediction in a horizontal circular micro-channel,” Int. Commun. Heat Mass Transf., **35**(7), pp. 833–838.

[79] Lee, J., and Mudawar, I., 2005, “Two-phase flow in high-heat-flux micro-channel heat sink for refrigeration cooling applications: Part I—pressure drop characteristics,” Int. J. Heat Mass Transf., **48**(5), pp. 928–940.

[80] Choi, C., and Kim, M., 2011, “Flow pattern based correlations of two-phase pressure drop in rectangular microchannels,” Int. J. Heat Fluid Flow, **32**(6), pp. 1199–1207.

[81] Dalkilic, A. S., Kürekci, N. A., and Wongwises, S., 2011, “Effect of void fraction and friction factor models on the prediction of pressure drop of R134a during downward condensation in a vertical tube,” Heat Mass Transf., **48**(1), pp. 123–139.

[82] Shah, R. K., and London, A. L., 1978, Advances in Heat Transfer: Supplement, Academic Press.

[83] Satish G. Kandlikar, 2006, Heat Transfer and Fluid Flow in Minichannels and Microchannels, Elservier Science Ltd, Oxford.

[84] Kays, W. M., and London, A. L., 1984, Compact Heat Exchangers, McGraw-Hill.

[85] Owens, W. L., “Two-phase pressure gradient,” Int. Dev. in heat transfer, ASME.

[86] Cicchitti, A., Lombardi, C., Silvestri, M., Soldaini, G., and Zavattarelli, R., 1959, Two-Phase Cooling Experiments: Pressure Drop, Heat Transfer and Burnout Measurements, Centro Informazioni Studi Esperienze, Milan.

[87] McAdams, W. H., Woods, W. K., and Heroman, L. C., 1964, "Vaporization inside horizontal tubes, II. Benzene–oil mixture," Trans ASME, **64**, pp. 193–200.

[88] Akers, W. W., Deans, H. A., and Crosser, O. K., 1958, "Condensing Heat Transfer Within Horizontal Tubes," Chem Eng Progr, **Vol: 54, No. 10**.

[89] Beattie, D. R. H., and Whalley, P. B., 1982, "A simple two-phase frictional pressure drop calculation method," Int. J. Multiph. Flow, **8**(1), pp. 83–87.

[90] Dukler, A. E., Wicks, M., and Cleveland, R. G., 1964, "Frictional pressure drop in two-phase flow: A. A comparison of existing correlations for pressure loss and holdup," AIChE J., **10**(1), pp. 38–43.

[91] Kalani, A., and Kandlikar, S. G., 2014, "Evaluation of Pressure Drop Performance During Enhanced Flow Boiling in Open Microchannels With Tapered Manifolds," J. Heat Transf., **136**(5), pp. 051502–051502.

[92] Kalani, A., and Kandlikar, S. G., 2015, "Effect of taper on pressure recovery during flow boiling in open microchannels with manifold using homogeneous flow model," Int. J. Heat Mass Transf., **83**, pp. 109–117.

[93] Çıkım, T., Armağan, E., Ince, G. O., and Koşar, A., 2014, "Flow boiling enhancement in microtubes with crosslinked pHEMA coatings and the effect of coating thickness," J. Heat Transf., **136**(8), p. 081504.

[94] Balasubramanian, K., Jagirdar, M., Lee, P. S., Teo, C. J., and Chou, S. K., 2013, "Experimental investigation of flow boiling heat transfer and instabilities in straight microchannels," Int. J. Heat Mass Transf., **66**, pp. 655–671.

[95] Zhu, Y., Antao, D., Chu, K.-H., Hendricks, T. J., and Wang, E. N., 2014, "Enhanced Flow Boiling Heat Transfer in Microchannels with Structured Surfaces."

[96] Kandlikar, S. G., and Balasubramanian, P., 2004, "An Extension of the Flow Boiling Correlation to Transition, Laminar, and Deep Laminar Flows in Minichannels and Microchannels," Heat Transf. Eng., **25**(3), pp. 86–93.

[97] Kandlikar, S. G., 1983, "An Improved Correlation for Predicting Two-Phase Flow Boiling Heat Transfer Coefficient in Horizontal and Vertical Tubes," HTD Publ Am Soc Mech Eng U. S., HTD-VOL-27.

[98] Kandlikar, S. G., 1990, “A General Correlation for Saturated Two-Phase Flow Boiling Heat Transfer Inside Horizontal and Vertical Tubes,” J. Heat Transf., **112**(1), pp. 219–228.

[99] Phillips, R. J., “Forced-convection, liquid-cooled, microchannel heat sinks,” Massachusetts Institute of Technology.

[100] Buchling Rego, Philipp K., "Flow Boiling in Open Microchannels with Tapered Manifolds using Ethanol in a Gravity-Driven Flow" (2015). Thesis. Rochester Institute of Technology. Accessed from http://scholarworks.rit.edu/theses/8721

Chapter 10: Appendix

Thermocouple Calibration

The thermocouples were calibrated using the OMEGA Hot Point® Dry Block Probe Calibrator for all k-type thermocouples used in the system. The calibration temperature range was set from 50°C – 230°C (increment of 30°C), all the thermocouples used operated in the set range. The below figure shows the calibration curve for a thermocouple T1 which is located in the heater block. Similar calibration curves were obtained for all thermocouples used. A linear curve fit was applied to the collected points to determine the equation for the thermocouple. The calibration equation is displayed with the R^2 value. This calibration equation values were inputted in the LabVIEW block diagram for temperature measurement.

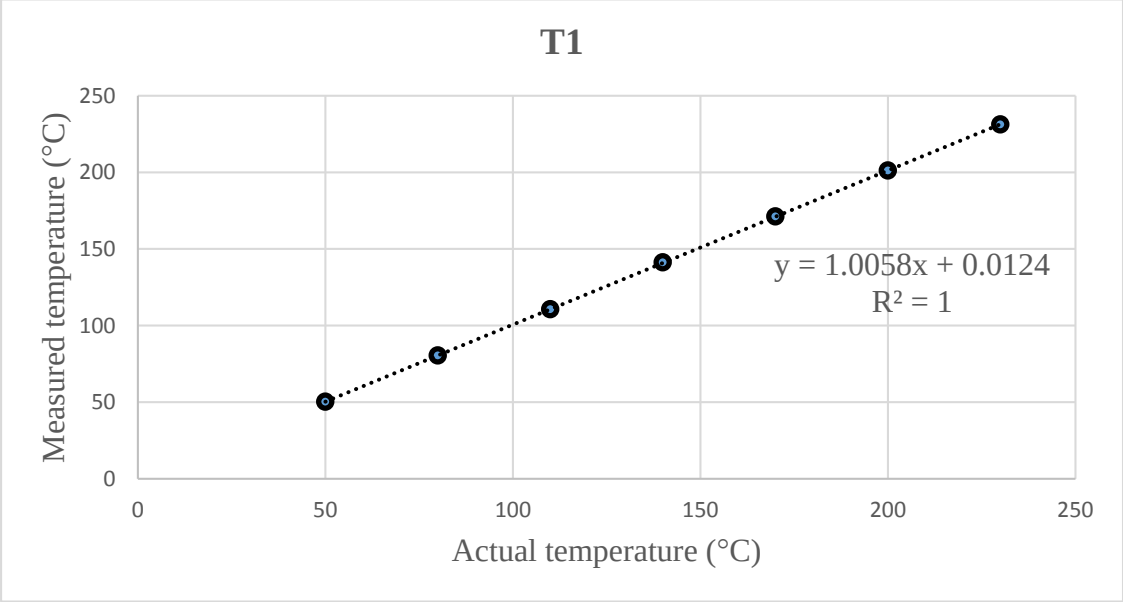

Similar procedure was followed for all thermocouples used. Standard deviation for each thermocouple was also calculated and used in the uncertainty analysis.

Error Propagation – Derivation of Uncertainties

The derivation of the uncertainty equations [100] shown in Section 6, of all key calculated parameters is shown below.

Heat Flux Uncertainty Derivation

The relation for heat flux, measured from the three heater block thermocouples, is computed from Eqns. (1) and (2) in Section 4, and shown below in Eqn. (34)

$$\boldsymbol{q'' = -k_{Cu}\left(\frac{3T_1 - 4T_2 + T_3}{2\Delta d}\right)} \quad (1)$$

The variables in Eqn. (34) are substituted into the error propagation equation (Eqn. 6), as shown in Eqn. (35) and Eqn. (36) below.

$$\frac{\boldsymbol{U_{q''}}}{\boldsymbol{q''}} = \sqrt{\sum_{i=1}^{n}\left(\frac{\partial \boldsymbol{q''}}{\partial \boldsymbol{\sigma_i}}\boldsymbol{U_{\sigma_i}}\right)^2} \quad (2)$$

$$\therefore \frac{\boldsymbol{U_{q''}}}{\boldsymbol{q''}} = \sqrt{\frac{\left(\frac{\partial \boldsymbol{q''}}{\partial \boldsymbol{k_{Cu}}}\boldsymbol{U_{k_{Cu}}}\right)^2 + \left(\frac{\partial \boldsymbol{q''}}{\partial \boldsymbol{\Delta d}}\boldsymbol{U_{\Delta d}}\right)^2 + \left(\frac{\partial \boldsymbol{q''}}{\partial \boldsymbol{T_1}}\boldsymbol{U_{T_1}}\right)^2 + \left(\frac{\partial \boldsymbol{q''}}{\partial \boldsymbol{T_2}}\boldsymbol{U_{T_2}}\right)^2 + \left(\frac{\partial \boldsymbol{q''}}{\partial \boldsymbol{T_3}}\boldsymbol{U_T}\right.}{\boldsymbol{q''^2}}} \quad (3)$$

It will be useful for the derivation to define a variable α defined as shown in Eqn. (37).

$$\alpha = 3T_1 - 4T_2 + T_3 \quad (4)$$

This will simplify the derivations that follow. The sensitivity coefficients for each variable, which are expressed as partial derivatives of the equation (function *p* in Eqn. 6) with respect to the individual variables of interest (variables σ_i in Eqn. 6), are evaluated individually. The expressions are then rewritten in terms of the function of interest, *q''*, as shown in Eqns. (38-42).

$$\frac{\partial q"}{\partial k_{Cu}} = -\frac{\alpha}{2\Delta d} = \frac{q"}{k_{Cu}} \quad (5)$$

$$\frac{\partial q"}{\partial \Delta x} = -k_{Cu}\frac{\alpha}{-2\Delta d^2} = -\frac{q"}{\Delta d} \quad (6)$$

$$\frac{\partial q"}{\partial T_1} = -k_{Cu}\frac{3}{2\Delta d} = \frac{3q"}{\alpha} \quad (7)$$

$$\frac{\partial q"}{\partial T_2} = -k_{Cu}\frac{-4}{2\Delta d} = -\frac{4q"}{\alpha} \quad (8)$$

$$\frac{\partial q"}{\partial T_3} = \frac{-k_{Cu}}{2\Delta d} = \frac{q"}{\alpha} \quad (9)$$

The terms in Eqns. (38-42) are substituted back into Eqn. (36) to obtain the following.

$$\frac{\boldsymbol{U_{q"}}}{\boldsymbol{q"}} = \sqrt{\frac{\left(\frac{\boldsymbol{q"}}{\boldsymbol{k_{Cu}}}\boldsymbol{U_{k_{Cu}}}\right)^2 + \left(-\frac{\boldsymbol{q"}}{\boldsymbol{\Delta d}}\boldsymbol{U_{\Delta d}}\right)^2 + \left(\frac{\boldsymbol{3q"}}{\boldsymbol{\alpha}}\boldsymbol{U_{T_1}}\right)^2 + \left(-\frac{\boldsymbol{4q"}}{\boldsymbol{\alpha}}\boldsymbol{U_{T_2}}\right)^2 + \left(\frac{\boldsymbol{q"}}{\boldsymbol{\alpha}}\boldsymbol{U_{T_3}}\right)^2}{\boldsymbol{q"^2}}} \quad (10)$$

The squared terms in each of the parentheses in the numerator of Eqn. (43) are expanded in Eqn. (44).

$$\frac{\boldsymbol{U_{q"}}}{\boldsymbol{q"}} = \sqrt{\frac{\frac{\boldsymbol{q"^2}}{\boldsymbol{k_{Cu}^2}}\boldsymbol{U_{k_{Cu}}^2} + \frac{\boldsymbol{q"^2}}{\boldsymbol{\Delta x^2}}\boldsymbol{U_{\Delta x}^2} + \frac{\boldsymbol{9q"^2}}{\boldsymbol{\alpha^2}}\boldsymbol{U_{T_1}^2} + \frac{\boldsymbol{16q"^2}}{\boldsymbol{\alpha^2}}\boldsymbol{U_{T_2}^2} + \frac{\boldsymbol{q"^2}}{\boldsymbol{\alpha^2}}\boldsymbol{U_{T_3}^2}}{\boldsymbol{q"^2}}} \quad (11)$$

This allows all $q"^2$ terms in the numerator to cancel with the denominator, thus yielding the final expression in Eqn. (7), which is reproduced below in Eqn. (45).

$$\frac{\boldsymbol{U_{q"}}}{\boldsymbol{q"}} = \sqrt{\frac{\boldsymbol{U_{k_{Cu}}}^2}{\boldsymbol{k_{Cu}^2}} + \frac{\boldsymbol{U_d}^2}{\boldsymbol{\Delta d^2}} + \frac{\boldsymbol{9U_{T_1}}^2}{\boldsymbol{\alpha^2}} + \frac{\boldsymbol{16U_{T_2}}^2}{\boldsymbol{\alpha^2}} + \frac{\boldsymbol{U_{T_3}}^2}{\boldsymbol{\alpha^2}}} \quad (12)$$

Chip Surface Temperature Uncertainty Derivation

The relation for surface temperature is calculated from the heat flux over the projected area, taking into account the thermal resistance of copper, and the distance between the top thermocouple and the surface, as is shown in Eqn. (3) in Section 4. While the uncertainty in surface temperature is expected to be quite low, mathematical rigor dictates it is required in order to compute the uncertainty in heat transfer coefficient.

The variables in Eqn. (3) are substituted into the error propagation equation (Eqn. 6), as shown in Eqn. (46) and Eqn. (47) below.

$$\frac{\boldsymbol{U_{T_s}}}{\boldsymbol{T_s}} = \sqrt{\sum_{\boldsymbol{i=1}}^{\boldsymbol{n}} \left(\frac{\boldsymbol{\partial T_s}}{\boldsymbol{\partial \sigma_i}} \boldsymbol{U_{\sigma_i}}\right)^{\boldsymbol{2}}} \tag{13}$$

$$\therefore \frac{\boldsymbol{U_{T_s}}}{\boldsymbol{T_s}} = \sqrt{\frac{\left(\frac{\boldsymbol{\partial T_s}}{\boldsymbol{\partial T_1}} \boldsymbol{U_{T_1}}\right)^{\boldsymbol{2}} + \left(\frac{\boldsymbol{\partial T_s}}{\boldsymbol{\partial q''}} \boldsymbol{U_{q''}}\right)^{\boldsymbol{2}} + \left(\frac{\boldsymbol{\partial T_s}}{\boldsymbol{\partial d_1}} \boldsymbol{U_{d_1}}\right)^{\boldsymbol{2}} + \left(\frac{\boldsymbol{\partial T_s}}{\boldsymbol{\partial k_{Cu}}} \boldsymbol{U_{k_{Cu}}}\right)^{\boldsymbol{2}}}{\boldsymbol{T_s^2}}} \tag{14}$$

The sensitivity coefficients for each variable are evaluated individually below. The expressions are then rewritten in terms of the function of interest, T_s, as shown in Eqns. (48-51).

$$\frac{\partial T_s}{\partial T_1} = 1 - 0 = 1 = \frac{T_s}{T_s} \tag{15}$$

$$\frac{\partial T_s}{\partial q''} = 0 - 1\left(\frac{d_1}{k_{Cu}}\right) = -\left(\frac{d_1}{k_{Cu}}\right)\left(\frac{T_s}{T_s}\right) \tag{16}$$

$$\frac{\partial T_s}{\partial d_1} = -\frac{q''}{k_{Cu}} = -\frac{q''}{k_{Cu}}\left(\frac{T_s}{T_s}\right) \tag{17}$$

$$\frac{\partial T_s}{\partial k_{Cu}} = -q''d_1 = -q''d_1\left(\frac{T_s}{T_s}\right) \tag{18}$$

The terms in Eqns. (48-51) are substituted back into Eqn. (47) to obtain the following expression.

$$\frac{U_{T_s}}{T_s} = \sqrt{\frac{\left(\frac{T_s}{T_s}U_{T_1}\right)^2 + \left(-\left(\frac{d_1}{k_{Cu}}\right)\left(\frac{T_s}{T_s}\right)U_{q"}\right)^2 + \left(-\frac{q"}{k_{Cu}}\left(\frac{T_s}{T_s}\right)U_{d_1}\right)^2 + \left(-q"d_1\left(\frac{T_s}{T_s}\right)U_{k_{Cu}}\right)}{T_s^2}} \quad (19)$$

The squared terms in each of the parentheses in the numerator of Eqn. (52) are expanded in Eqn. (53).

$$\frac{\boldsymbol{U_{T_s}}}{\boldsymbol{T_s}} = \sqrt{\frac{\boldsymbol{\frac{T_s^2}{T_s^2}U_{T_1}^2 + \frac{d_1^2}{k_{Cu}^2}\frac{T_s^2}{T_s^2}U_{q"}^2 + \frac{q"^2}{k_{Cu}^2}\frac{T_s^2}{T_s^2}U_{d_1}^2 + q"^2d_1^2\frac{T_s^2}{T_s^2}U_{k_{Cu}}^2}}{\boldsymbol{T_s^2}}} \quad (20)$$

This allows all $q"^2$ terms in the numerator to cancel with the denominator, thus yielding the final expression shown in Eqn. (54).

$$\frac{\boldsymbol{U_{T_s}}}{\boldsymbol{T_s}} = \sqrt{\boldsymbol{\frac{U_{T_1}^2}{T_s^2} + \frac{U_{q"}^2d_1^2}{k_{Cu}^2T_s^2} + \frac{U_{d_1}^2q"^2}{k_{Cu}^2T_s^2} + \frac{U_{k_{Cu}}^2q"^2d_1^2}{T_s^2}}} \quad (21)$$

7.3.4 **Heat Transfer Coefficient Uncertainty Derivation**

The relation for heat transfer coefficient is shown in Eqn. (4) in Section 4. The variables in Eqn. (4) are substituted into the error propagation equation (Eqn. (6) in Section 4), as shown in Eqn. (55) and (56) below.

$$\frac{\boldsymbol{U_h}}{\boldsymbol{h}} = \sqrt{\boldsymbol{\sum_{i=1}^{n}\left(\frac{\partial h}{\partial \sigma_i}U_{\sigma_i}\right)^2}} \quad (22)$$

$$\frac{\boldsymbol{U_h}}{\boldsymbol{h}} = \sqrt{\frac{\left(\frac{\boldsymbol{\partial h}}{\boldsymbol{\partial q''}}\boldsymbol{U_{q''}}\right)^{\boldsymbol{2}} + \left(\frac{\boldsymbol{\partial h}}{\boldsymbol{\partial T_s}}\boldsymbol{U_{T_s}}\right)^{\boldsymbol{2}} + \left(\frac{\boldsymbol{\partial h}}{\boldsymbol{\partial T_{sat}}}\boldsymbol{U_{T_{sat}}}\right)^{\boldsymbol{2}}}{\boldsymbol{h^2}}} \qquad (23)$$

The sensitivity coefficients for each variable are evaluated individually. The expressions are then rewritten in terms of the function of interest, *h*, as shown in Eqns. (57-59).

$$\frac{\partial h}{\partial q''} = \frac{1}{T_s - T_{sat}} = \frac{h}{q''} \qquad (24)$$

$$\frac{\partial h}{\partial T_s} = -\frac{q}{(T_s - T_{sat})^2} = -\frac{h}{(T_s - T_{sat})} \qquad (25)$$

$$\frac{\partial h}{\partial T_{sat}} = \frac{q}{(T_s - T_{sat})^2} = \frac{h}{(T_s - T_{sat})} \qquad (26)$$

The terms in Eqns. (57-59) are substituted back into Eqn. (56) to obtain the following.

$$\frac{\boldsymbol{U_h}}{\boldsymbol{h}} = \sqrt{\frac{\left(\frac{\boldsymbol{h}}{\boldsymbol{q''}}\boldsymbol{U_{q''}}\right)^{\boldsymbol{2}} + \left(-\frac{\boldsymbol{h}}{\boldsymbol{(T_s - T_{sat})}}\boldsymbol{U_{T_s}}\right)^{\boldsymbol{2}} + \left(\frac{\boldsymbol{h}}{\boldsymbol{(T_s - T_{sat})}}\boldsymbol{U_{T_{sat}}}\right)^{\boldsymbol{2}}}{\boldsymbol{h^2}}} \qquad (27)$$

The squared terms in each of the parentheses in the numerator of Eqn. (60) are expanded in Eqn. (61).

$$\frac{\boldsymbol{U_h}}{\boldsymbol{h}} = \sqrt{\frac{\frac{\boldsymbol{h^2 U_{q''}^2}}{\boldsymbol{q''^2}} + \frac{\boldsymbol{h^2 U_{T_s}^2}}{\boldsymbol{(T_s - T_{sat})^2}} + \frac{\boldsymbol{h^2 U_{T_{sat}}^2}}{\boldsymbol{(T_s - T_{sat})^2}}}{\boldsymbol{h^2}}} \qquad (28)$$

This allows all h^2 terms in the numerator to cancel with the denominator, thus yielding the final expression in Eqn. (9), which is reproduced below in Eqn. (62).

$$\frac{U_h}{h} = \sqrt{\frac{U_{q"}^2}{q"^2} + \frac{U_{T_s}^2}{\Delta T_{sat}^2} + \frac{U_{T_{sat}}^2}{\Delta T_{sat}^2}} \quad (29)$$

Heat Loss Study

A heat loss study was conducted via numerical simulation in ANSYS® Fluent® to establish the amount of heat lost at the edges of the chip surface [100]. This was done by developing a 2-D model of the heater block geometry in ANSYS® GAMBIT, and importing the model into Fluent®. The heater block is modelled with its true dimensions, including the ceramic insulation located on its sides and the silicone gasket on the top surface, as shown in Fig. 24(a). The central portion of the surface, which would normally be cooled by the fluid of choice in the flow boiling system, is perfectly insulated. The input heat from the bottom surface can therefore only flow to the sides of the chip. In this manner, any input heat flux will represent the heat loss for a given surface temperature T_s. There is a contact resistance associated with the ceramic insulation that is not accounted for. This thermal contact resistance arises as a result of the ceramic insulation blocks not being affixed to the surfaces of the copper block, and would result in lower heat losses than the portrayed scenario. Thus, the model as stated represents a worst-case scenario of heat loss at the sides of the chip.

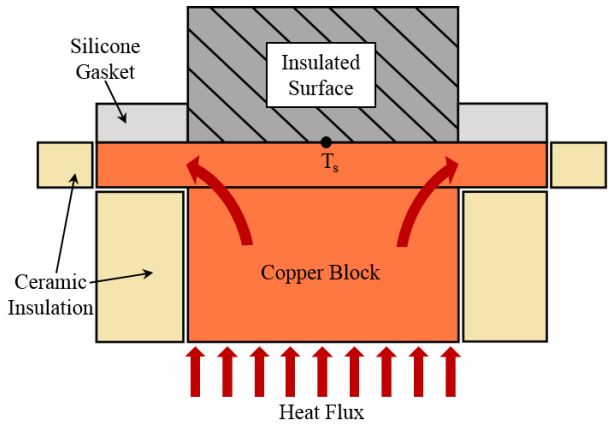

(a)

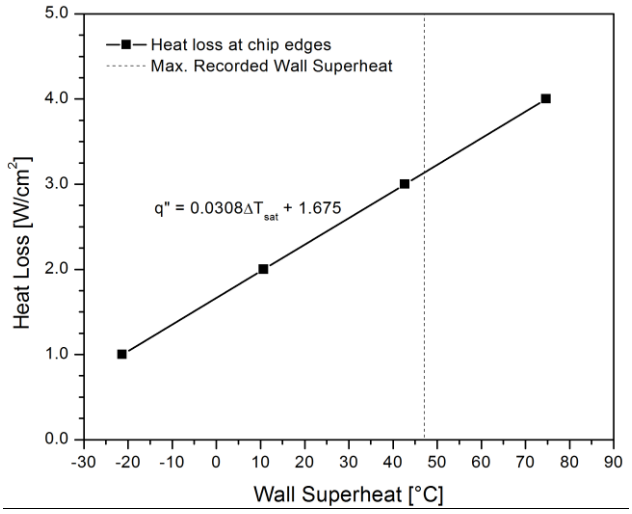

(b)

Figure 78: (a) Heat loss simulation model, (b) Plot of heat loss as a function of wall superheat

Several heat fluxes are simulated in order to cover the entire operating range for the chip surface temperature across the nucleate boiling range, up to CHF. The heat loss and surface temperature are correlated via a linear trendline equation to establish an estimate of heat loss at every heat flux. A plot of the simulation results is shown in Fig. 78(b) along with the corresponding trendline.

The final heat flux values calculated from the results are thus adjusted taking into account the predicted heat loss for the corresponding wall superheat, as shown in equation below

$$q''_{adjusted} = q''_{measured} - q''_{loss}$$

$$= q''_{measured} - (0.0308\Delta T_{sat} + 1.675)$$

For the purpose of this analysis it was chosen to neglect the contact resistance between the ceramic blocks and the heater side faces. In reality, this contact resistance will not be negligible due to the lack of adhesion or thermal interface material between the ceramic blocks and the heater side faces. As a result, it is expected that small air pockets will form between the ceramic blocks and the heater side faces, effectively worsening the thermal conductivity in those areas. This estimate of heat loss at the chip edges therefore represents a worst-case study of heat loss.

Effect of inertia force

To better understand the effect of inertia force, a non-dimensional parameter K_1 is used. K_1 represents the ratio of the evaporation momentum force to the liquid inertia force at the liquid-vapor interface[2] and is given by:

$$K_1 = \left(\frac{q^{"}}{G h_{LV}}\right)^2 \frac{\rho_L}{\rho_v}$$

Where q" is heat flux, G is mass flux, h_{LV} is the latent heat of vaporization, ρ_L is the liquid density and ρ_V is the vapor density. For q", CHF values are taken and K_1 is plotted against the Re. The below plot (Fig. S1) shows that as the Re increases to Re = 800, a drastic reduction in K_1 from 0.12 to 0.04 is observed. This represents the dominant effect of inertia forces, however further increase in Re does not show the same sharp reduction. The ratio K_1 flattens out, indicating that the CHF does not increase with further increase in flow. Further increase in Re beyond Re>1100 show a small decrease from 0.04 to 0.02 in K_1 value. This represents a modest increase in the CHF, but as noted earlier, comes with a significant pressure drop penalty.

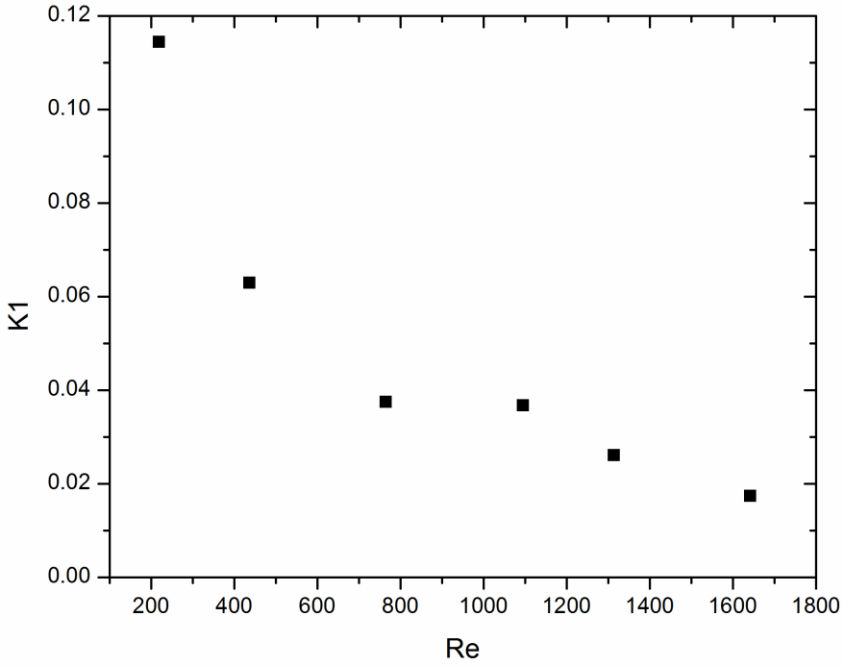

Fig. S1 Variation of K_1 with Re for flow boiling CHF data of tapered manifold

Comparison to pool boiling

Pool boiling heat transfer mechanism is at the core of any flow boiling system. The main advantages of pool boiling for high heat flux removal are a uniform surface temperature and an efficient heat removal system. Recent advances have made this boiling process quite efficient with nanowires, open microchannels, and combinations of different hierarchical surface structures consisting of a combination of nanoscale and microscale features. Figure 1 shows a comparison of some of the recent high performing pool boiling structures reported in the literature.

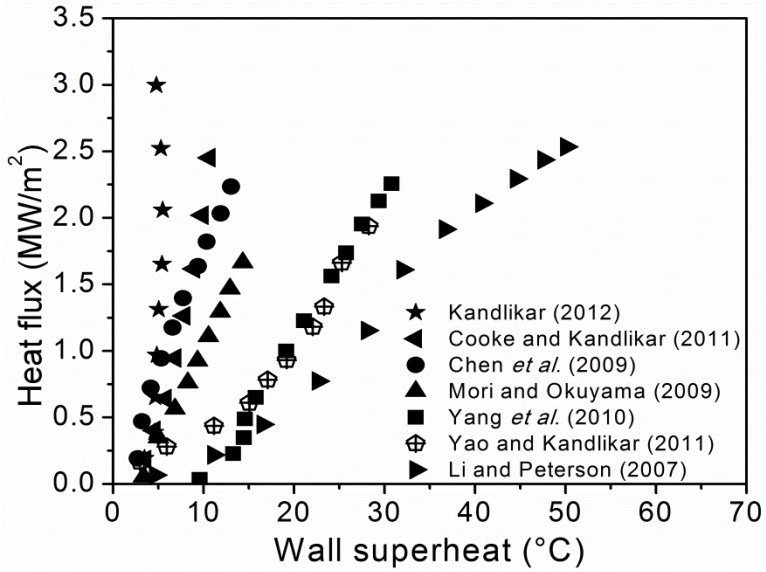

Figure 1: Enhanced pool boiling performance reported in literature.

Mori and Okuyama [23] used a porous plate while Chen et al. [24] and Yao et al. [25, 26] used copper nanowires. Yang et al. [27] employed an open foam cover and Li and Peterson [28] employed a sintered wire mesh. Cooke and Kandlikar [29, 30] used open microchannels that resulted in a heat flux of 244 W/cm^2 with a heat transfer coefficient of

269,000 W/m$^{2\circ}$C. A microstructure design based on utilizing the evaporation momentum force proposed by Kandlikar [31] was able to dissipate a heat flux of over 300 W/cm^2 with a record heat transfer coefficient of 629,000 W/m$^{2\circ}$C. In comparison, the microchannel flow boiling systems have a significantly lower performance as seen from the literature review. In order to justify the additional complexities over pool boiling, it is essential for a flow boiling system to provide (i) a stable operation, and (ii) superior heat transfer coefficient and CHF values.

The best pool boiling performance currently exceeds the OMM configurations investigated in this paper. Cooke and Kandlikar [29, 30] achieved a heat flux of 250 W/cm^2 at ΔT_{sat} = 10 °C using the best performing microchannel chip tested in pool boiling, while in the initial tests reported here, a maximum heat flux of 506 W/cm^2 was obtained with ΔT_{sat} = 26.2 °C. It may be noted that CHF was not reached during any of the tests due to the temperature limitations of the heater, and only one microchannel configuration was tested to validate the concept. CHF was thus significantly enhanced in the OMM design.

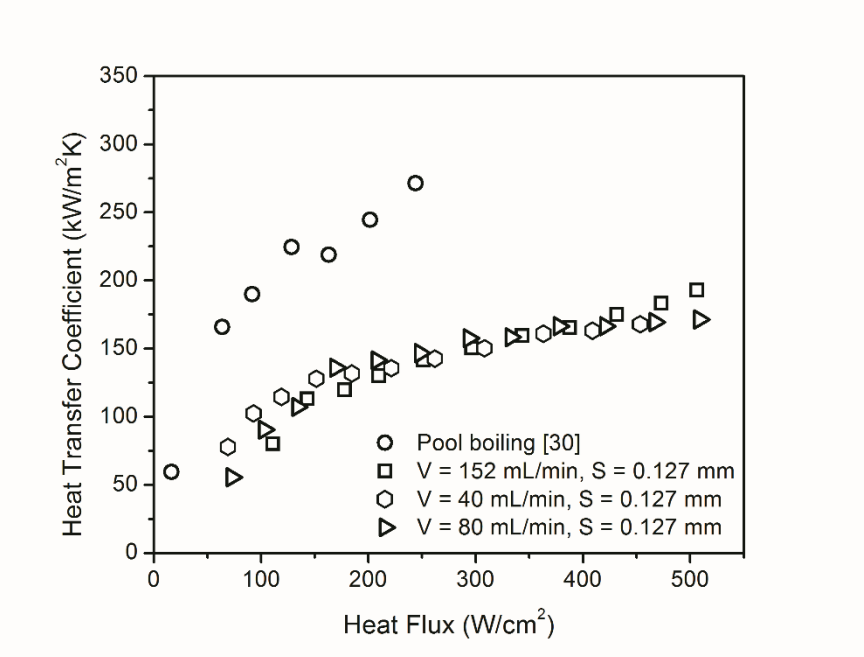

Figure 17: Heat transfer coefficient vs. heat flux comparison between pool boiling and flow boiling with uniform manifold block, microchannel chip and V = 152 mL/min and S = 0.127 mm

Figure 17 shows a comparison between the heat transfer coefficients for pool boiling and flow boiling. The three tests which reached the maximum heat flux of around 500 W/cm^2 have been included in this plot. It is seen that the three cases yield a very similar heat transfer coefficients which improve with heat flux. The pool boiling setup with open microchannels yielded a maximum heat transfer coefficient of 270 kW/m^2·°C at a heat flux of 250 W/cm^2 [30], while the current OMM flow boiling setup attained a maximum heat transfer coefficient of 193 kW/m^2·°C at a heat flux of 506 W/cm^2. Pool boiling outperformed flow boiling in terms of heat transfer coefficient at all heat fluxes. These results indicate that flow boiling in OMM does not improve heat transfer efficiency in nucleate boiling mode, and that its utility lies primarily in enhancing the CHF through vapor removal and liquid supply to the nucleation sites.

It is seen that the OMM design exceeds the pool boiling performance of the advanced open microchannel design in terms of CHF. Further improvements are expected as the manifold gap, taper and microchannel geometry undergo refinements.

5.1 Effect of Tapered Manifold

The effect of manifold taper on flow stability was evaluated by comparing inlet pressure fluctuations at steady state conditions for both uniform and tapered manifold blocks with a plain chip with an entry spacing S = 1.524 mm as shown in Fig. 5. For each heat flux, the pressure drop readings taken over a 5 minute period at 5 Hz frequency are shown.

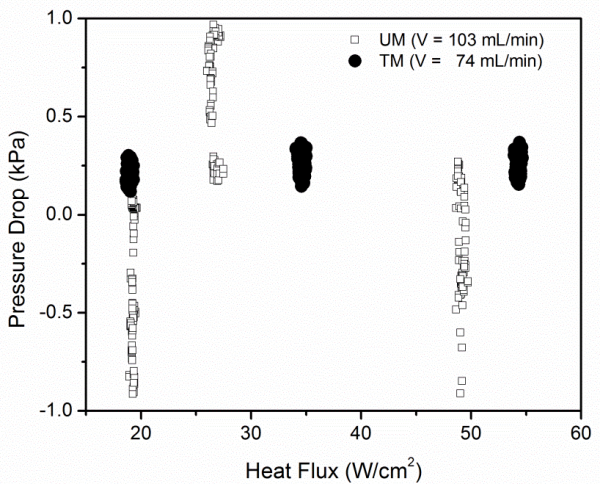

Figure 5

The uniform manifold tests were run with a flow rate of V = 103 mL/min and the tapered manifold tests were run with a slightly lower flow rate of V = 74 mL/min. For all heat fluxes tested, the uniform manifold displayed inlet pressure fluctuations between positive and negative values, whereas the pressure drop was almost constant for the tapered manifold over the time interval. For all heat flux values, the tapered block produced

positive and steady inlet pressure readings over a 5-minute time interval, indicating that the tapered manifold mitigates flow boiling instability experienced with uniform manifold.

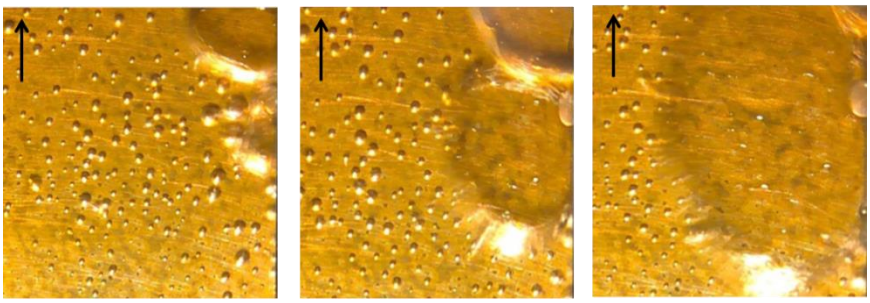

Figure 6: Unstable flow boiling with plain surface with a uniform manifold, successive images taken at 8 ms time intervals with V = 103 mL/min and spacing S = 1.524 mm.

The improvement in stability is also demonstrated in video footage of bubble formation for each test. Figure 6 shows a sequence of three high speed images 8 ms apart with a uniform manifold block and a plain test chip at V = 103 mL/min and S = 1.524 mm. A nucleating bubble forms on the right edge of the frame and then expands both upstream and downstream, thereby inducing back flow in the test section that is responsible for the pressure fluctuations shown in Fig. 5.

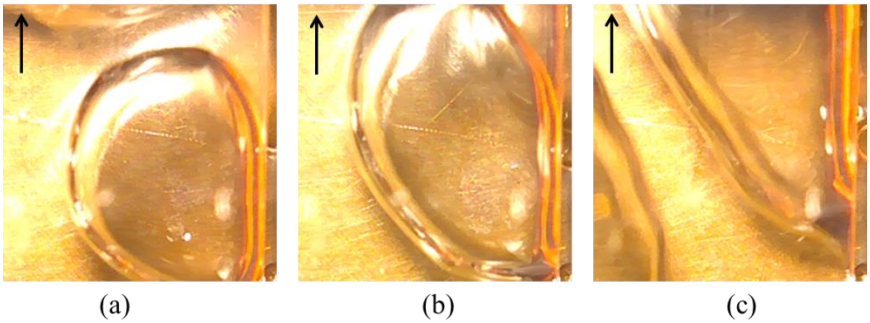

Figure 7: Stable flow boiling on a plain surface with a tapered manifold, successive images taken at 3 ms time interval with a flow rate of 74 mL/min and an inlet spacing S = 1.524 mm.

The image sequence in Fig. 7 corresponds to a tapered manifold block with a plain test chip at V = 74 mL/min and S = 1.524 mm. In this case the nucleating bubble forms and detaches from the chip surface without expanding against the flow direction. This results in a reduction in pressure fluctuations and improved flow boiling stability.

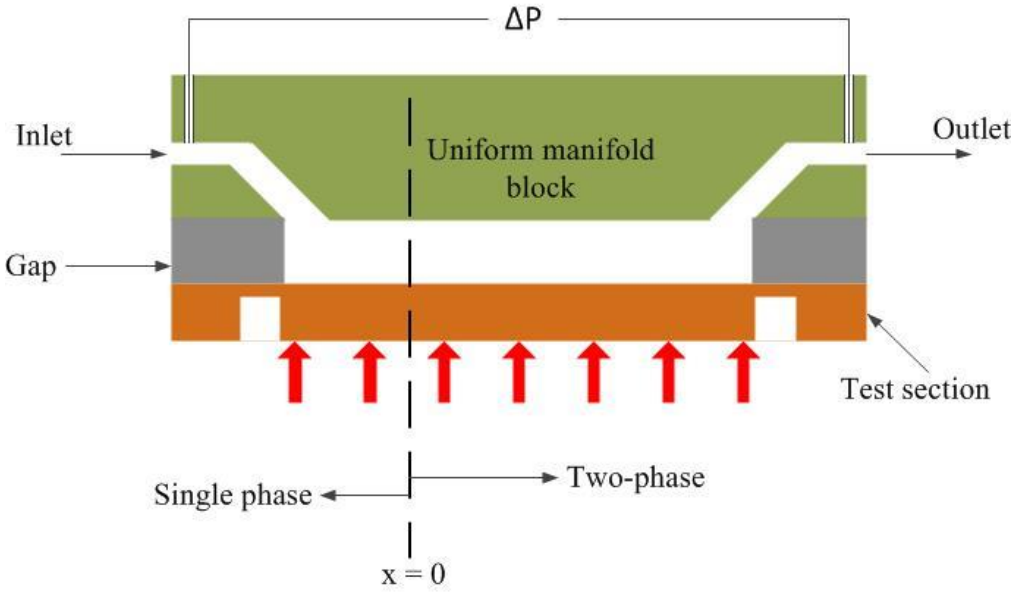

Oscillatory Flow Pattern

Stable flow boiling was obtained over a plain surface with the help of a tapered manifold. No flow reversal was observed over the entire ranges of parameters tested. However, an oscillatory motion was seen at the heat fluxes above 100 W/cm^2. Figures 9(a) and (b) show the liquid region (L) with a vapor bubble (V). A liquid film is present underneath the vapor bubble and multiple dry spots are visible. In the next two images (c and d), the vapor stream was seen shifting towards the right hand side, and dry spots appeared near the liquid-vapor interface on both sides along the edges. In Figs. 9(e) and (f), the bubble nucleation was observed in the liquid region near the center area. The liquid-vapor interface is clearly seen in Figs. 9(f) and the vapor stream is seen to go from left to right and then back from right to left in Figs. 9(f)-(h). The above sequence of images show an oscillatory motion of flow, however no back flow was observed during this motion. The dryout regions in the liquid film underneath the bubble were rewetted during the back and forth motion of the vapor stream. Similar oscillatory motion was also observed with uniform manifold configuration.

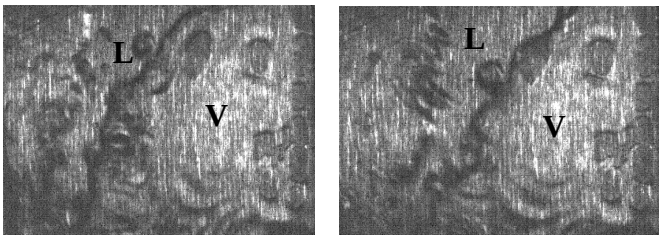

(a) (b)

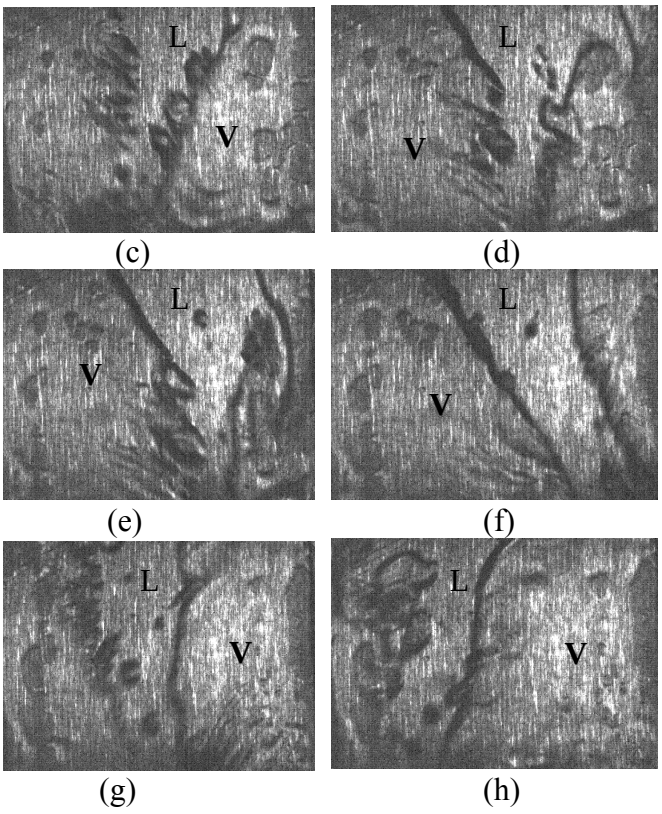

Figure 9 (a-h). Sequence of images showing oscillatory motion in the geometry at higher heat fluxes.

Heat transfer Modeling

To take in account the effect of flow rate in Kandlikar and Balasubramanian [97] correlation, h_{LO} is calculated using the Dittus-Boelter correlation. The correlation is given by the formula below:

$$h_{LO} = 0.023\, Re_L^{0.8} Pr_L^{0.4} \frac{k_L}{D_h}$$

Where Re_L is liquid Reynolds number, Pr_L is liquid Prandtl number and k_L is liquid thermal conductivity.

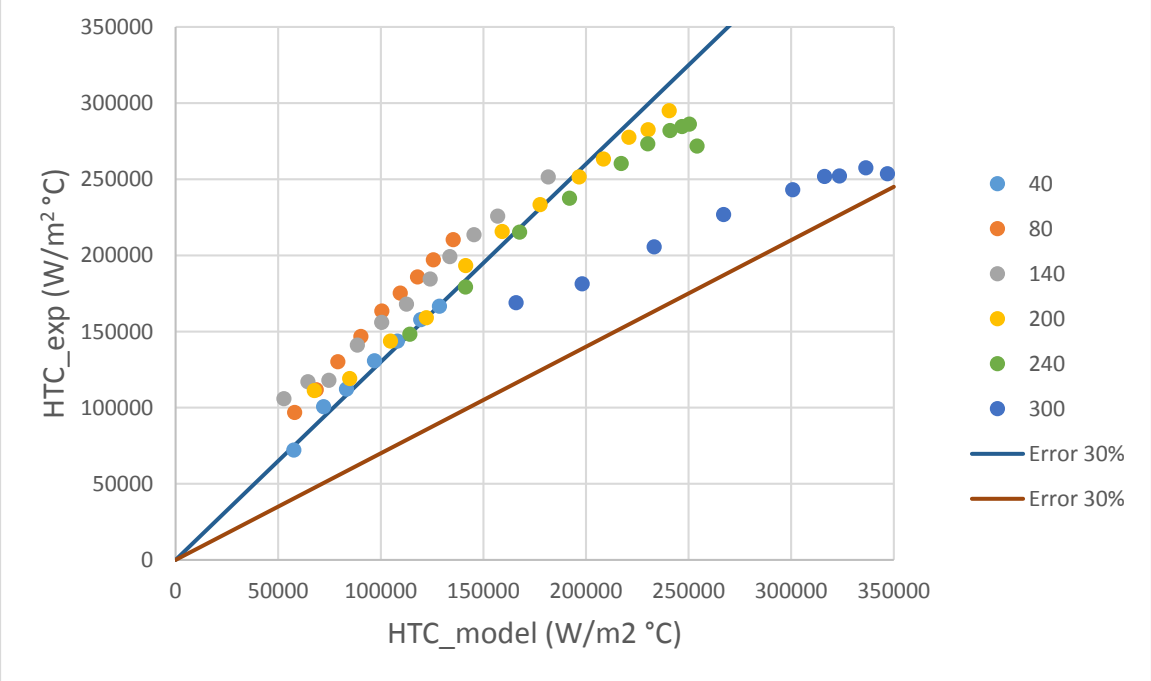

Figure 79: Comparison of heat transfer coefficient experimental data with Kandlikar and Balasubramanian [97] correlation using Dittus-Boelter for all flow rates

Publication List

Journal Paper

[1] Kalani, A., and Kandlikar, S. G., 2015, “Combining Liquid Inertia With Pressure Recovery From Bubble Expansion for Enhanced Flow Boiling,” Appl. Phys. Lett, 107, 181601 doi: 10.1063/1.4935211

[2] Kalani, A., and Kandlikar, S. G., 2015, “Flow patterns and heat transfer mechanisms during flow boiling over open microchannels in tapered manifold (OMM),” Int. J. Heat Mass Transf., 89, pp. 494–504.

[3] Kalani, A., and Kandlikar, S. G., 2015, “Effect of taper on pressure recovery during flow boiling in open microchannels with manifold using homogeneous flow model,” Int. J. Heat Mass Transf., 83, pp. 109–117.

[4] Kalani, A., and Kandlikar, S. G., 2014, “Evaluation of Pressure Drop Performance During Enhanced Flow Boiling in Open Microchannels With Tapered Manifolds,” J. Heat Transf., 136(5), pp. 051502–051502.

[5] Kandlikar, S. G., Widger T., Kalani A., and Mejia V.,2013, “Enhanced Flow Boiling Over Open Microchannels With Uniform and Tapered Gap Manifolds,” J. Heat Transf., 135(6), p. 061401.

Conference Paper

[1] Kalani, A., and Kandlikar, 2016, "Heat Dissipation Beyond 1 kW/cm2 with Low Pressure Drop and High Heat Transfer Coefficient for Flow Boiling using Open Microchannels with Tapered Manifold," ASME 2015 14th International Conference on Nanochannels, Microchannels, and Minichannels, Washington, DC, USA, July 10–14, 2016

[2] Kalani, A., and Kandlikar, 2015, "A Photographic Study of Flow Boiling Stability on a Plain Surface With Tapered Manifold," ASME 2015 13th International Conference on Nanochannels, Microchannels, and Minichannels, San Francisco, California, USA, July 6–9, 2015

[3] Kalani, A., and Kandlikar, 2014, "Pressure Drop Analysis Using the Homogeneous Model for Open Microchannel with Manifold (OMM)," ASME 2014 International Conference on Nanochannels, Microchannels, and Minichannels, Chicago, Illinois, USA.

[4] Kalani, A., and Kandlikar, 2013, "Preliminary Results of Pressure Drop Modeling During Flow Boiling in Open Microchannels With Uniform and Tapered Manifolds (OMM)," ASME 2013 International Mechanical Engineering Congress and Exposition, San Diego, California, USA.

[5] Kalani, A., and Kandlikar, 2013, "Experimental Investigation of Flow Boiling Performance of Open Microchannels With Uniform and Tapered Manifolds (OMM)," ASME 2013 Heat Transfer Summer Conference, Minneapolis, Minnesota, USA.